INFORMATION TO USERS

This manuscript has been reproduced from the microfilm master. UMI films the text directly from the original or copy submitted. Thus, some thesis and dissertation copies are in typewriter face, while others may be from any type of computer printer.

The quality of this reproduction is dependent upon the quality of the copy submitted. Broken or indistinct print, colored or poor quality illustrations and photographs, print bleedthrough, substandard margins, and improper alignment can adversely affect reproduction.

In the unlikely event that the author did not send UMI a complete manuscript and there are missing pages, these will be noted. Also, if unauthorized copyright material had to be removed, a note will indicate the deletion.

Oversize materials (e.g., maps, drawings, charts) are reproduced by sectioning the original, beginning at the upper left-hand corner and continuing from left to right in equal sections with small overlaps. Each original is also photographed in one exposure and is included in reduced form at the back of the book.

Photographs included in the original manuscript have been reproduced xerographically in this copy. Higher quality 6" x 9" black and white photographic prints are available for any photographs or illustrations appearing in this copy for an additional charge. Contact UMI directly to order.

UMI

A Bell & Howell Information Company
300 North Zeeb Road, Ann Arbor MI 48106-1346 USA
313/761-4700 800/521-0600

Imaging mid-mantle discontinuities : Implications for mantle chemistry, dynamics, rheology, and deep earthquakes

by

John C. Castle

A dissertation submitted in partial fulfillment

of the requirements for the degree of

Doctor of Philosophy

University of Washington

1998

Approved by Kenneth C. Creager

(Chairperson of Supervisory Committee)

Program Authorized

to Offer Degree

Date

Doctoral Dissertation

In presenting this dissertation in partial fulfillment of the requirements for the Doctoral degree at the University of Washington, I agree that the Library shall make its copies freely available for inspection. I further agree that extensive copying of this dissertation is allowable only for scholarly purposes, consistent with "fair use" as prescribed in the U.S. Copyright Law. Requests for copying or reproduction of this dissertation may be referred to University Microfilms, 1490 Eisenhower Place, P.O. Box 975, Ann Arbor, MI, 48106, to whom the author has granted "the right to reproduce and sell (a) copies of the manuscript in microform and/or (b) printed copies of the manuscript made from microform."

Signature John C. Castle

Date March 2, 1998

University of Washington

Abstract

Imaging mid-mantle discontinuities : Implications for mantle chemistry, dynamics, rheology, and deep earthquakes

by John C. Castle

Chairperson of Supervisory Committee

Professor Kenneth C. Creager

Geophysics Program

Using teleseismic network data and new signal processing techniques, I investigated mantle structure in the vicinity of subduction zones. The 660-km seismic discontinuity in the Izu-Bonin region is depressed by up to 80 km, indicative of material 1000°K colder than ambient mantle. A broad depression of the discontinuity near 33°N suggests that the subducting slab extends to the west upon the discontinuity from 139°E to at least 135°E. Farther to the south near 26°N, a narrow and confined discontinuity depression suggests local penetration. Along the entire Mariana-Bonin-Izu-Japan-Kuril Trench, the dip of the slab changes to vertical at the deepest earthquake, regardless of the depth of the earthquakes. This observation implies that the slab loses strength at the seismicity cutoff. A grain size reduction due to the olivine to spinel phase change would create a weak zone within the slab, eliminate the slab membrane strength, and thus provide a mechanism allowing the slab to fall vertically downward. The 660-km discontinuity is less than 3 km thick and the shear wave jump across the discontinuity is .40 km/sec ± .05 km/sec. This jump agrees with the velocity jump predicted of a pyrolite mantle containing 4% cation aluminum at

the bottom of the transition zone. I observed the 410-km discontinuity infrequently, suggesting this discontinuity broadens in the subduction zone, possibly due to high water content. There exists no consistent sharp ($<$ 10 km) discontinuity between 660 km and 410 km depth and between 410 km and the crust. Beneath the 660-km discontinuity in Izu-Bonin, there does not exist another horizontal discontinuity to at least 1300 km. If a chemical change is associated with the 660-km discontinuity, it produces a very small change in shear velocity ($\delta Vs < 1\%$). The absence of a discontinuity in the 660 km - 1300 km depth range shows that a hypothesized global discontinuity does not exist at these depths. Applying new migration and stacking techniques to global waveform data, I used S-to-P scattered arrivals to image a deep dipping structure beneath Izu-Bonin, which I interpret as an ancient slab. Reinterpretations of S wave tomography, P wave tomography, and plate reconstructions all confirm this result.

TABLE OF CONTENTS

LIST OF FIGURES

LIST OF TABLES

ACKNOWLEDGMENTS

I am grateful to many people:

- My parents and sister (and the cats)
- Seattle - Ken Creager and John Winchester
- Göttingen - Chuck Wicks and Michael Weber
- Canberra - Brian Kennett, Phil Cummins, and Malcolm Sambridge
- Christine Schmitt

Chapter 1

INTRODUCTION

The goals of my doctoral research were twofold. On the engineering side, I wanted to apply modern signal processing tools to newly available large datasets of teleseismic waveforms. On the scientific side, I was interested in finding out as much as possible about the seismic structure of the mid-mantle and then interpreting the results in terms of a dynamical and chemical earth.

This dissertations consists of six interrelated chapters, all of which use vertical component teleseismic network data recorded by and archived at data centers in the Western United States, Germany, Australia, England, and India. Each chapter is written in the style of a complete paper. Chapter 2 has been accepted to *Journal of Geophysical Research* as *Castle and Creager* [1998]. Chapter 5 was published in *Geophysical Research Letters* as *Castle and Creager* [1997]. Chapter 3 will be submitted to a special edition of the new journal *Earth, Planets and Space.* Chapters 4 and 6 have been prepared as short papers while chapter 7 contains additional information findings.

My advisor, Professor Kenneth C. Creager, helped prepare the manuscripts for *Castle and Creager* [1997] and *Castle and Creager* [1998].

Chapter 2 - topography of the 660-km discontinuity

Near a depth of 660-km, γ-spinel (Ringwoodite) transforms to perovskite and magnesiowüstite ($Mg_2SiO_4 \rightarrow MgSiO_3 + MgO$) [*Liu*, 1979], creating a sharp discontinuity

in seismic wave-speeds which can be imaged using seismic network data. The phase change is endothermic [*Ito and Takahashi*, 1989] such that cold material depresses the depth of the phase change. Assuming that cold material is subducted slab, precisely mapping the topography of the 660-km discontinuity reveals where the slab exists at depth.

Using teleseismic S-to-P converted phases generated at the 660-km discontinuity below earthquakes ($S_{660}P$), data migration techniques, and stacking algorithms, we imaged the discontinuity structure in the Izu-Bonin subduction zone south of Japan. We found that the slab depresses the discontinuity up to 85 km, suggesting a thermal anomaly of -1000°K. Inferring slab location from the shape of the discontinuity, we confirmed earlier tectonic reconstructions and suggested that there exists a tear in the slab near 29.5°N. Finally, the location of the deepest earthquakes (near 450 km) and the location of the slab at the 660-km discontinuity imply that the slab descends vertically downward from the earthquakes to the discontinuity, regardless of the dip of the slab above the earthquakes. From the change in dip of the slab, we infer that there exists a weak zone in the slab at the deepest earthquakes.

Chapter 3 - a connection between slab rheology and deep earthquakes

In the previous chapter, we showed that in the Izu-Bonin subduction zone, the slab dip steepens sharply at the seismicity cutoff. In this chapter, we incorporated additional observations of the subducting slab in the northwest Pacific, including observations from hypocenter locations, residual sphere analyses, and regional tomographic studies. Along the entire Mariana-Bonin-Izu-Japan-Kuril-Kamchatka arc, the slab dip increases dramatically at the location of the seismicity cutoff.

Synthesizing mineral physics modeling results, deep earthquakes are likely the result of buoyancy stresses in the transition zone combined with the meta-stable olivine to spinel phase change. When the phase change occurs in cold slabs, there is a grain size reduction of up to four orders of magnitude.

Inferring a connection between the change in dip and the deep earthquakes, we hypothesize that the earthquakes, marking the olivine to spinel phase change, create a zone of weakness that eliminates the membrane strength of the slab which allows the slab to sink downward.

Chapter 4 - the size of the 660-discontinuity and mantle chemistry

In this chapter we looked at the amplitude of the $S_{660}P$ phase. The amplitude is directly related to the size of the shear wave velocity jump across the discontinuity and insensitive to either the density jump or compressional velocity jump. We found the size of the shear wave jump was slightly larger than the amount in the *iasp91* velocity model [*Kennett and Engdahl*, 1991].

For several years, the velocity jump at the 410-km discontinuity was believed to be incompatible with the velocities predicted by the mantle chemistry model pyrolite (e.g. *Bass and Anderson* [1984]) . Comparisons to mineral physics data suggest that our observed value of the shear wave velocity jump at the 660-km discontinuity is consistent with a pyrolitic mantle. Using recent extrapolations from mineral physics data [*Weidner and Wang*, 1998], we found our value was most consistent with a pyrolitic mantle containing 4% cation aluminum (Al^+).

Chapter 5 - a discontinuity below 660-km?

We next turned our attention to the area beneath the 660-km discontinuity. If the depth of a hypothetical chemical discontinuity globally coincides with the depth of the γ-spinel to magnesiowüstite and perovskite phase change, they should locally separate in the presence of a downgoing slab. *Kawakatsu and Niu* [1994] also found evidence for a discontinuity near 920-km depth in other subduction zones and suggested that there exists a global 920-km discontinuity.

We found no evidence for a subhorizontal discontinuity beneath Izu-Bonin, implying that a chemical does not coincide with the spinel to magnesiowüstite and

perovskite phase change and that the 920-km discontinuity is not a global feature.

Chapter 6 - a deep dipping structure beneath Izu-Bonin

While we did not observe evidence for a discontinuity below the 660-km discontinuity in Izu-Bonin, we did observe isolated arrivals in the stacked seismic data. These phases arrived at seemingly random times and slownesses and, when interpreted as horizontal surfaces, suggested over five different, sharp discontinuities between 660 km and 1100 km.

Searching for an alternate explanation for these arrivals, we created a new data processing and migration technique which enabling us to search for scatterers throughout the mantle. Applying the new procedure to short-period data recorded in the western United States, we imaged a dipping structure near 1000 km depth beneath and parallel to the Izu-Bonin trench.

Both tomographic shear and compressional wave models show a previously unnoticed feature in the same location. Plate reconstructions suggest that subduction has taken place in this region during the past 30 My. We interpret the structure imaged in the short-period seismic data as an ancient, chemically distinct subducted Moho and the structure in the tomographic models as the broader thermal anomaly of a subducted slab.

Chapter 7 - between the crust and the 660-km discontinuity

Finally, we collected seismic data to investigate the upper mantle and developed a new method to present and analyze stacked data.

We confirmed previous results that the 660-km discontinuity is extremely sharp. We find no evidence for any sharp discontinuity in the 660 km - 410 km and 410 km - surface depth range. As we use data filtered between 2 and 5 sec, our observations limit the minimum thickness of any possible discontinuity, such as the 520-km discontinuity, to 7 km.

Interestingly, we did not consistently observe the 410-km discontinuity. Both our data and other groups findings are creating a consensus that the 410-km discontinuity is somehow disrupted near subduction zones. Two interesting propositions are that the discontinuity is locally broadened due either to thermal effects or to increased amounts of water.

Finally, surface reflected pP waves generated at oceanic crust intriguingly appeared different than those generated at continental crust. The *pPoceanic* contained precursor energy that are likely due to reflections off of the bottom of the oceanic crust.

Chapter 2

TOPOGRAPHY OF THE 660-KM SEISMIC DISCONTINUITY BENEATH IZU-BONIN: IMPLICATIONS FOR TECTONIC HISTORY AND SLAB DEFORMATION

2.1 Abstract

We analyze the P-wave codas of 65 paths from deep northwestern Pacific earthquakes recorded by arrays of stations in Germany, the Western United States, India, and Turkmenistan. We identify a phase resulting from a near-source S-to-P conversion at a nearly horizontal discontinuity ranging in depth from 650 to 730 km, which we interpret as a thermally depressed spinel to perovskite and magnesiowüstite phase transition. We migrate these data along with 39 more from *Wicks and Richards* [1993], accounting for three-dimensional ray bending by the sloping discontinuity, to produce a high-resolution topography map of the 660-km discontinuity in the Izu-Bonin region. Assuming an equilibrium phase transition, we interpret the discontinuity depth in terms of local temperatures. The slab, if defined by a thermal anomaly greater than -400°K, is only about 100 km thick near 28°N suggesting the slab is penetrating into the lower mantle with little or no advective thickening. Farther to the north, however, cold material appears spread out over a wide region, consistent with the slab having been laid down flat on the 660-km discontinuity as the trench retreated 2000 km eastward. Both the narrow slab to the south and the flat-lying slab to the north are consistent with recent high-resolution tomographic images. The depression

to 745 km along the arc is consistent with a maximum thermal anomaly of about 1100°K. Along the entire arc, the depression occurs directly beneath the deepest earthquakes, even where seismicity is dipping at 45° and stops at 450 km depth, suggesting that the slab steepens to a vertical dip at the deepest seismicity. This change to a vertical orientation suggests that the slab loses strength temporarily through a physical process which causes the seismicity to increase dramatically and then abruptly cease.

2.2 Introduction

Images of subducting slabs interacting with mantle structures reveal crucial information to unlock our knowledge of mantle conditions. Their interactions depend critically on several conditions, including the viscosity of the various layers, the Clapeyron slope of mineral phase changes, and the regional subduction history. There exists a seismic discontinuity near 660 km depth (the 660-km discontinuity) that is most likely caused by the γ-spinel to perovskite and magnesiowüstite phase change (e.g., *Ringwood*, 1991). This phase change is endothermic with a Clapeyron slope of -2 to -2.8 MPa/°K [*Ito and Takahashi*, 1989; *Bina and Helffrich*, 1994] , such that cold material will displace the discontinuity to greater pressures and depths. Therefore by measuring the depth of the discontinuity, we have a direct measure of mantle temperature and, assuming cold material is subducted material, evidence revealing the slab location at depth. An increase in viscosity across the discontinuity will cause impinging slabs to buckle and thicken, hence the slab width at the discontinuity is strongly influenced by the viscosity contrast across the layers [*Gurnis and Hager*, 1988]. Finally, the location of cold slab material at depth depends on the historical motion of the trench. For example, theoretical calculations and physical models show that under a wide range of conditions, plates subducting at a stationary trench create a vertical column of slab material that penetrates through the 660-km discontinuity

into the lower mantle. On the other hand, a rapidly retreating trench typically lays slab material out upon the discontinuity [*Griffiths et al.*, 1995; *Guillou-Frottier et al.*, 1995; *Christensen*, 1996; *Zhong and Gurnis*, 1997] .

Most tectonic reconstructions argue that the northern Izu trench retreated seaward almost 1000 km to the northeast from 30 Ma to 17 Ma. At more recent times, the picture is less clear, but the trench location probably remained stationary from 17 Ma to 5 Ma, at which time it is hypothesized that it began advancing to the west/southwest at a rate of 3 mm/yr at 32°N and 27mm/yr at 27°N [*Seno and Maruyama*, 1984; *Carlson and Mortera-Gutierrez*, 1990; *Otsuki*, 1990; *van der Hilst and Seno*, 1993] . Images of the slab in this region based on seismicity, such as *Katsumata and Sykes* [1969], extend only to the depth of the deepest earthquakes, which are near 550 km depth at the southern end of the Bonin trench (near 25°N) but extend only to 430 km in the Izu trench (near 33°N).

In this study, we employ a method using near source S-to-P converted phases to image the slab at the 660-km discontinuity. These data support the above scenario of trench migration and are evidence that the slab bends to a vertical dip at the seismicity cutoff, suggesting a connection between the deepest earthquakes and slab rheology.

2.3 Data and Method

We analyze the $S_{660}P$ phase for 65 earthquake/network pairs to estimate the depth of the 660-km discontinuity. This phase leaves the earthquake traveling downward as an S wave, converts to a P wave at the discontinuity near 660 km depth beneath the source, and continues on to the seismometers as a P wave, following a path similar to the direct P wave (Figure 2.1).

Our data consist of teleseismic vertical-component P wave codas from 43 deep western Pacific earthquakes recorded by the Southern California Seismic Network

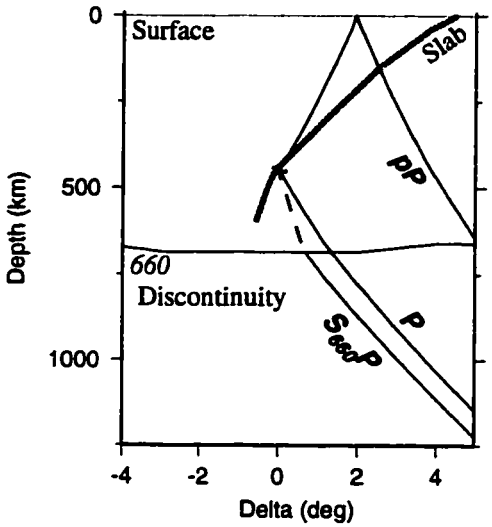

Figure 2.1: Ray paths of the P , $S_{660}P$, and pP phases in the vicinity of the slab. The difference in time between $S_{660}P$ and P determines the depth to the discontinuity.

(SCSN), Northern California Seismic Network (NCSN), and Pacific Northwest Seismic Network (PNSN) in the Western United States, the Grafenburg Regional Array (GRFN), the German Regional Seismic Network (GRSN), the Gauribidanur Array (GBA) in India, and the Geyookcha Array in Turkmenistan (Tables 2.1 & 2.2, Figure 2.2).

We process the data to identify the small amplitude $S_{660}P$ phase. Because the $S_{660}P$ phase travels from the earthquake to the 660-km discontinuity as a slower S wave, it arrives at the seismometers later than the direct P wave. By observing the delay time of the $S_{660}P$ wave relative to the P wave, employing a velocity model (we use *iasp91* [*Kennett and Engdahl*, 1991]), and using relocated hypocenters (we use *Engdahl et al.* [1997]), we determine the distance the $S_{660}P$ wave traveled as an S wave and thus the depth of the discontinuity.

For a flat lying discontinuity (Figure 2.1), the $S_{660}P$ ray, like the direct P ray, travels along the great circle path but travels slightly deeper into the mantle and arrives at the seismic network at a steeper angle than the F wave. The angle at which a ray arrives is measured in slowness, with steeper angles having smaller slownesses. (Slowness is the reciprocal of the horizontal wavefront speed across the network.) We

Table 2.1: Non Izu-Bonin earthquakes

Eq No	Date	Lat °N	Lon °E	Dep km	Mb	Net[a]	# Sta	Del (°)	$S_{660}P$ Lat	$S_{660}P$ Lon	$S_{660}P$ Dep	$S_{660}P$ PQ[b]
					Sea of Japan							
a	80- 1-18	37.83	133.52	430	6.0	bbGER	12	79.2	38.5	132.9	706	2
b	80- 3-31	35.49	135.59	363	6.1	bbGER	9	82.0	36.1	135.1	651	1
c	82- 2- 3	36.90	135.73	341	5.6	bbGER	12	81.0	37.6	135.1	671	3
d	88-11- 5	37.15	135.96	334	5.9	bbGER	12	80.9	37.9	135.3	671	3
e	90- 4-11	35.51	135.62	369	5.6	bbGER	13	82.1	36.2	135.1	665	1
f	90- 5-17	37.09	137.06	263	5.9	bbGER	12	81.4	37.9	136.4	...	...
g	92- 8- 7	35.78	135.31	359	6.3	spPNSN	102	73.0	36.4	136.1	666	1
h	93- 1-19	38.67	133.46	459	6.0	spSCSN	41	81.5	39.0	134.0	662	3
i	93- 1-19	38.67	133.46	459	6.0	spPNSN	110	71.8	39.1	134.0	658	3
j	95- 3-31	38.17	135.06	364	6.0	bbUS	17	78.4	38.7	135.9	667	3
					Ryukyu Trench							
k	81- 1- 2	29.27	128.20	232	6.1	bbGER	8	83.5	30.1	127.5	666	2
l	86-12-21	25.52	122.47	271	6.1	bbGER	13	83.5	26.3	121.8	641	2
m	87- 5- 3	28.42	127.73	206	5.8	spPNSN	90	82.7	29.3	128.6	658	2
n	87- 6-12	25.47	122.19	267	5.8	bbGER	11	83.4	26.3	121.4	700	2
o	94- 6-14	25.94	124.11	213	6.0	bbGER	7	84.5	26.8	123.4	650	3
					Marianas Trench							
p	87-10- 6	18.76	145.03	510	6.7	spIN	18	64.9	18.8	144.3	670	1

[a] bb = vertical broadband, sp = vertical short-period, GER = GRFN/GRSN, US = (PNSN, NCSN, and SCSN), IN = India, and GY = Geyookcha

[b] Pick Quality = 1 (best), 2, or 3

measure slownesses to distinguish phases; i.e., the $S_{660}P$ wave has a slightly smaller slowness value than the P wave (Figure 2.3).

For each earthquake and network pair we remove noisy traces, demean the seismograms, apply a 2-5 s bandpass filter, normalize amplitudes to the P wave, align on the P arrival, and slant-stack using a non-linear N^{th} root algorithm [*Muirhead and Datt*, 1976] with N=3. We empirically choose N=3 and the 2-5 s bandpass filter as both give optimal noise reduction and signal clarity. However, for several events, mainly those with either small magnitudes or few receivers (events # 27, 38, 39, 42, 45, and 49), we use a bandpass filter of either 1-4 s or 1-3 s due to increased noise near 5 s period. The N^{th} root stacking algorithm robustly and dramatically reduces the amplitude of incoherent signals across the network, such as signals generated in varying near re-

Table 2.2a: Izu-Bonin earthquakes

#	Date	Lat °N	Lon °E	Dep km	Mb	Net[a]	# Sta	Del (°)	Theo. amp.[b]	Filter Sec	Pick Qual.[c]
1	80- 4-22	32.16	137.74	402	6.1	bbGER	13	85.8	7%	2-5	1
2	82- 7- 4	27.91	137.04	547	6.3	bbGER	12	89.1	6%	2-5	2
3	82- 7- 4	27.91	137.04	547	6.3	spNCSN	121	82.0	6%	2-5	2
4	84- 1- 1	33.69	136.82	386	6.5	bbGER	13	84.1	104%	2-5	...
5	84- 3- 6	29.40	138.94	456	6.2	bbGER	13	88.7	17%	2-5	2
6	84- 3- 6	29.40	138.94	456	6.2	spNCSN	91	79.6	12%	2-5	2
7	84- 4-24	30.94	138.49	400	6.1	bbGER	13	87.2	6%	2-5	1
8	84- 4-24	30.94	138.49	400	6.1	spSCSN	99	83.2	24%	2-5	3
9	84- 4-24	30.94	138.49	400	6.1	spPNSN	77	74.4	23%	2-5	3
10	85- 4- 3	28.27	139.65	472	5.9	bbGER	13	90.0	0%	2-5	...
11	85- 4- 3	28.27	139.65	472	5.9	spNCSN	173	79.8	23%	2-5	1
12	85- 4- 3	28.30	139.60	472	5.9	spPNSN	76	75.6	22%	2-5	1
13	85- 4-10	29.98	139.01	409	5.8	bbGER	12	88.3	1%	2-5	1
14	85- 4-10	29.98	139.01	409	5.8	spSCSN	82	83.5	26%	2-5	...
15	85- 9-10	27.23	139.97	517	5.8	bbGER	13	91.0	3%	2-5	3
16	85- 9-10	27.23	139.97	517	5.8	spSCSN	103	84.4	23%	2-5	1
17	85-10- 4	27.63	140.01	491	5.9	bbGER	13	90.7	6%	2-5	2
18	85-12- 3	26.97	140.55	439	5.9	bbGER	13	91.5	2%	2-5	1
19	86- 2- 3	27.92	139.52	529	5.8	bbGER	13	90.2	15%	2-5	2
20	86- 2- 3	27.92	139.52	529	5.8	spSCSN	74	84.5	12%	2-5	2
21	86- 2- 3	27.92	139.52	529	5.8	spIN	19	59.3	12%	2-5	2
22	86- 3-17	27.43	140.07	478	5.8	bbGER	12	90.9	11%	2-5	3
23	87- 5-19	29.96	139.20	411	6.1	bbGER	12	88.4	9%	2-5	...
24	87-10- 2	27.35	140.08	463	5.8	bbGER	12	91.0	5%	2-5	...
25	88- 9- 7	30.38	137.56	504	6.1	bbGER	9	87.1	10%	2-5	...
26	88- 9- 7	30.38	137.56	504	6.1	spSCSN	60	84.1	11%	2-5	...
27	88- 9-13	30.03	138.68	456	5.8	bbGER	13	88.1	-1%	1-3	2
28	89- 6-16	31.85	138.19	369	5.9	bbGER	13	86.3	12%	2-5	1
29	90- 4-14	27.28	140.16	466	5.6	bbGER	13	91.1	-43%	2-5	...
30	90- 8- 5	29.59	137.75	523	6.0	bbGER	6	88.1	9%	2-5	2
31	90- 8- 5	29.59	137.75	523	6.0	spSCSN	40	83.5	7%	2-5	...
32	91- 5- 3	28.11	139.74	475	6.0	bbGER	13	90.2	2%	2-5	...
33	91- 5- 3	28.11	139.74	475	6.0	spNCSN	103	79.3	21%	2-5	1
34	92- 1-20	27.95	139.53	521	5.8	bbGER	7	90.1	37%	2-5	1
35	92- 1-20	27.95	139.53	521	5.8	spNCSN	131	79.6	18%	2-5	2
36	92- 1-20	27.95	139.53	521	5.8	spPNSN	97	76.0	17%	2-5	2
37	92- 5-30	30.77	141.91	12	5.9	spPNSN	104	72.5	-35%	2-5	1
38	92- 7-18	30.79	137.52	493	5.8	bbNCSN	8	81.3	57%	1-3	1
39	92- 7-18	30.79	137.52	493	5.8	spPNSN	69	75.3	-121%	1-4	1

continued on next page

[a] bb = vertical broadband, sp = vertical short-period, GER = GRFN/GRSN, US = (PNSN, NCSN, and SCSN), IN = India, and GY = Geyookcha

[b] Theoretical $S_{660}P$ / P amplitude

[c] Pick quality = 1 (best), 2, or 3

Table 2.2b: (continued)

#	Date	Lat °N	Lon °E	Dep km	Mb	Net[a]	# Sta	Del (°)	Theo. amp.[b]	Filter Sec	Pick Qual.[c]
continued from previous page											
40	92- 8-29	33.29	138.23	306	6.0	spNCSN	151	77.6	16%	2-5	1
41	92- 8-29	33.29	138.23	306	6.0	spPNSN	111	73.0	16%	2-5	2
42	92-10-30	30.00	139.15	413	6.0	bbNCSN	9	79.6	33%	1-4	1
43	92-10-30	30.00	139.15	413	6.0	bbGER	9	87.9	-7%	2-5	3
44	92-10-30	30.00	139.15	413	6.0	spNCSN	116	79.1	33%	2-5	1
45	93- 7- 5	30.25	138.92	406	5.5	spPNSN	91	74.8	12%	1-4	1
46	93- 7-20	27.36	140.01	461	6.1	spPNSN	76	76.1	-26%	2-5	1
47	93-10-11	32.04	137.89	357	6.4	bbGER	10	85.7	15%	2-5	2
48	93-10-11	32.04	137.89	357	6.4	spGY	36	63.7	15%	2-5	1
49	93-10-11	32.04	137.89	357	6.4	spPNSN	97	74.1	13%	1-4	1

[a] bb = vertical broadband, sp = vertical short-period, GER = GRFN/GRSN, US = (PNSN, NCSN, and SCSN), IN = India, and GY = Geyookcha

[b]Theoretical $S_{660}P$ /P amplitude

[c]Pick quality = 1 (best), 2, or 3

ceiver crustal structure relative to small, but coherent signals expected for structures near the source. By time shifting seismograms based on the distance between earthquakes and seismometers, the slant-stack algorithm allows us to use seismic networks as antennas to determine the direction of incoming energy [*Vidale and Benz*, 1992]. The large aperture of the networks, typically of order 1000 km, allows fine resolution of the slowness, as good as $\pm$ .05 s/°.

Additionally, we weight each seismogram based on the proximity of nearby stations. Studies in Washington State show that crustal reverberations are not correlated on spatial scales of several tens of kilometers [*Dewberry*, 1996], but are correlated on 10-km scales [*Pullen et al.*, 1995] . We use a weighting scheme based on that of *Goff and Jordan* [1988]; dense clusters of stations, such as those surrounding the volcano Mt. St. Helens, are down-weighted. We weight each individual seismogram by the equation:

$$Weight = \frac{1}{1 + \Sigma(1 + d_i/D)^{-2}} \tag{2.1}$$

where d_i are the distances (in km) from the seismometer to each of the other seis-

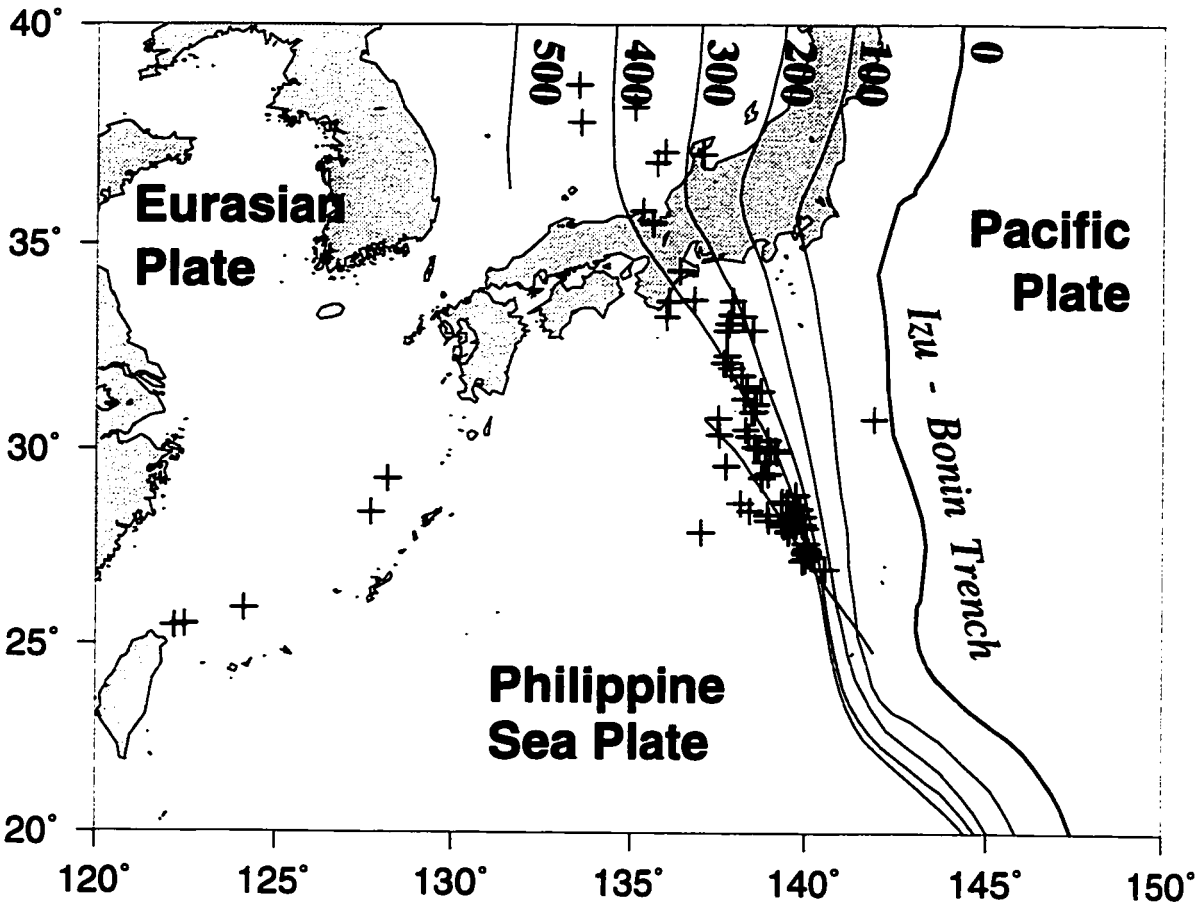

Figure 2.2: Tectonic setting of Izu-Bonin, the 43 earthquakes examined in this study (crosses), and Pacific Plate slab contours based on seismicity.

mometers and $D = 20$ km (i.e., weights are near unity when the nearest station is much over 20 km). This process further reduces signals generated in near receiver structures.

Figure 2.3a shows the 3^{rd} root slant-stacked data of event 11 after the envelope function has been applied (a vespegram). The theoretical arrival time and slowness of the $S_{660}P$ phase relative to the P phase is marked with an X. The trace below the vespegram is stacked along slowness values corresponding to theoretical values of S -to-P conversions at increasing discontinuity depths. The P , $S_{660}P$, and pP phases clearly stand out above the background noise. The next largest arrival, at 65 s, would

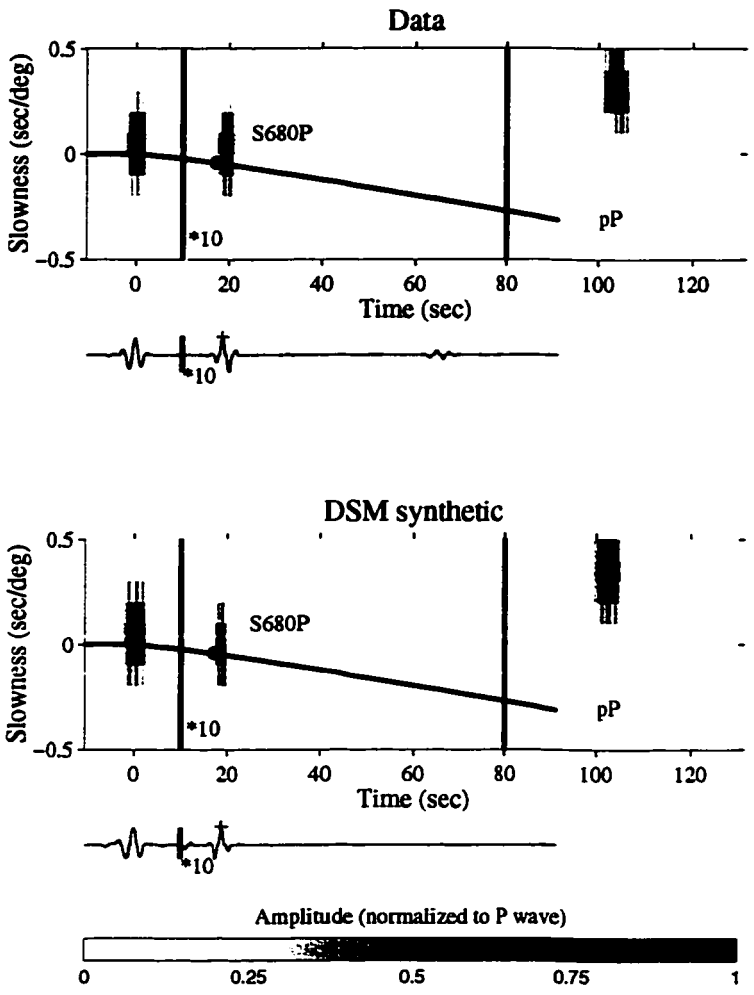

Figure 2.3: Vespegrams for the stacked data (top) and stacked DSM synthetics (bottom) with noise for event 11. Slowness is relative to the P slowness. The envelope function has been applied to traces after slant stacking using the 3^{rd} root algorithm. Amplitudes are normalized to the P wave and have been increased tenfold between dark lines. The color scale is linear. The trace below each vespegram is a 3^{rd} root stack along the slowness/time line plotted in the vespegram. Points on this line represent the theoretical time and slowness for S-to-P conversions off horizontal discontinuities at varying depths below the source.

be consistent with a horizontal discontinuity near 1200 km. However, the slowness is greater than expected for an S-to-P conversion at this depths, and the energy from this and other events can be better explained as coming from a steeply dipping sub-vertical structure deep beneath the Izu-Bonin trench [*Castle and Creager*, 1996b]. Returning to the $S_{660}P$ phases, the arrival time (1.6 s late compared to *iasp91*) and

slowness of the energy are consistent with a discontinuity depth of 679 km. The accuracies of these timings is approximately ± .2 sec which maps to a depth range of ± 2 km.

The small background noise in this vespegram implies a mantle clean of random scatterers along the great-circle path between the earthquake and California. The infinite frequency ray-tube from this event to the network has roughly a 25 km diameter at 1000 km depth and the detection level is approximately 1% for sharp S wave velocity changes [*Castle and Creager*, 1997]. This event exhibits evidence for only one such feature, which is at 60 s. Other events with over 100 stations and high signal-to-noise ratios also show evidence for a small number of distinct scatterers. While it is difficult to directly compare results, this observation appears to place upper limits on the observations of *Hedlin et al.* [1997] , who find evidence for small P -wave scatterers (1%) at 8 km length scales distributed evenly throughout the mantle.

We calculate complete synthetics for this event at periods of 2 s and longer using the Direct Solution Method *DSM* [*Cummins et al.*, 1994], the *iasp91* model and *PREM* densities [*Dziewonski and Anderson*, 1981], modified such that the 660-km discontinuity lies at 680 km depth. Synthetics are calculated using the *USGS* moment tensors [*Sipkin*, 1986] and the source location from *Engdahl et al.* [1997]. To add a source time function to the synthetics, we (1) linearly stack a six second window centered on the aligned P wave for both the data and synthetics, (2) deconvolve the resulting synthetic "source-time function" from the data "source-time function", and (3) convolve the resulting time series into each individual synthetic seismogram. This method removes any synthetic "source-time function" from the synthetics and adds the source time function from the data to the synthetics. We also add random noise to each synthetic. We determine amplitude of the noise added to each synthetic by fitting a first order polynomial to the envelope function of the observed seismogram in a time window 10 s after P to 10 s before pP , creating synthetics seismograms very similar in appearance to the data. Finally, we slant stack the synthetic seismograms

Table 2.3a: $S_{660}P$ locations and depths

Event	Original			Migrated		
No	Lat	Lon	Depth	Lat	Lon	Depth
1	32.9	137.2	731.5	32.8	137.1	730.2
2	28.3	136.8	706.2	28.0	136.9	699.4
3	28.1	137.3	681.0	27.9	137.4	675.8
4	34.3	136.4	...	...	...	...
5	29.9	138.6	681.3	29.9	138.6	680.3
6	29.8	139.5	671.0	29.9	139.8	666.4
7	31.5	138.1	668.0	31.5	138.3	665.1
8	31.4	139.2	676.1	31.5	139.2	674.8
9	31.5	139.1	675.0	31.6	139.2	674.0
10	28.8	139.3	...	...	...	...
11	28.6	140.2	679.0	28.8	140.2	676.4
12	28.8	140.1	677.0	29.1	140.2	671.0
13	30.7	138.5	726.0	30.5	138.5	723.4
14	30.5	139.8	...	...	...	...
15	27.6	139.7	670.0	27.4	139.6	665.5
16	27.5	140.4	680.0	27.4	140.7	674.4
17	28.1	139.7	723.0	27.9	139.2	711.9
18	27.6	140.1	721.0	27.5	139.8	716.1
19	28.4	139.2	751.0	28.2	139.0	744.9
20	28.2	140.0	675.0	28.4	140.0	670.5
21	27.9	138.7	708.1	27.9	138.4	703.4
22	27.9	139.7	738.7	27.9	139.4	735.7
23	30.5	138.8	...	...	...	...
24	27.9	139.7	...	...	...	...
25	31.0	137.1	...	...	...	...
26	30.7	138.0	...	...	...	...
27	30.5	138.3	706.0	30.4	138.6	700.7
28	32.5	137.7	687.2	32.6	138.2	679.2
29	27.7	139.9	...	...	...	...
30	30.0	137.5	705.0	29.9	137.7	700.3
31	29.8	138.1	...	...	...	...
32	28.7	139.3	...	...	...	...
33	28.5	140.3	690.0	28.8	140.4	685.9
34	28.3	139.3	685.5	28.6	139.6	676.0
35	28.2	139.9	675.0	28.4	140.0	671.2
36	28.3	139.9	673.0	28.4	140.0	669.9
37	32.0	143.4	650.0	31.9	143.4	649.6
38	31.1	138.0	678.1	31.2	138.2	674.8
39	31.3	138.1	670.0	31.3	138.2	665.2
40	33.9	139.2	664.1	33.9	139.4	661.7

continued on next page

Table 2.3b: (continued)

Event	Original			Migrated		
No	Lat	Lon	Depth	Lat	Lon	Depth
continued from previous page						
41	34.0	139.1	663.0	34.1	139.4	660.3
42	30.4	139.8	659.9	30.6	140.1	655.5
43	30.6	138.8	709.8	30.4	138.5	706.0
44	30.4	139.8	659.0	30.6	140.1	655.1
45	30.8	139.6	660.9	30.9	139.9	655.4
46	27.8	140.5	686.7	27.8	140.8	684.4
47	32.8	137.3	707.0	32.8	138.0	696.7
48	32.6	136.6	702.0	32.5	137.2	694.7
49	32.7	138.6	664.7	32.8	139.1	660.3

identically as the observed seismograms; Figure 2.3b shows the vespegram for the synthetics. The noise levels appear similar except for isolated arrivals in the data, suggesting isolated scatterers in the mantle as mentioned above. Comparing the synthetic stacks to the data stacks, we find that both the timings and amplitudes of the $S_{660}P$ waves agree well, justifying our interpretation that this is the $S_{660}P$ phase.

2.4 *Travel Time Determinations*

The $S_{660}P$ phase stands out above the extremely low background noise level for 54 of the 65 paths examined, revealing discontinuity depths between 650 km and 750 km (Tables 2.1 & 2.3; Figure 2.4). To determine discontinuity depths based on time delays of the $S_{660}P$ arrival, we create WKBJ synthetics [*Chapman et al.*, 1988] with two phases, the P and $S_{660}P$ waves. The WKBJ synthetics are generated as described above for the complete DSM synthetics, using *iasp91* velocities, *PREM* densities, *USGS* moment tensors, source time functions, but without additive noise.

We cross-correlate the synthetic $S_{660}P$ signal with the data $S_{660}P$ waveform and adjust the discontinuity depth to maximize this correlation. Additionally, we verify the slowness of the data $S_{660}P$ signal using vespegrams. While we have attempted

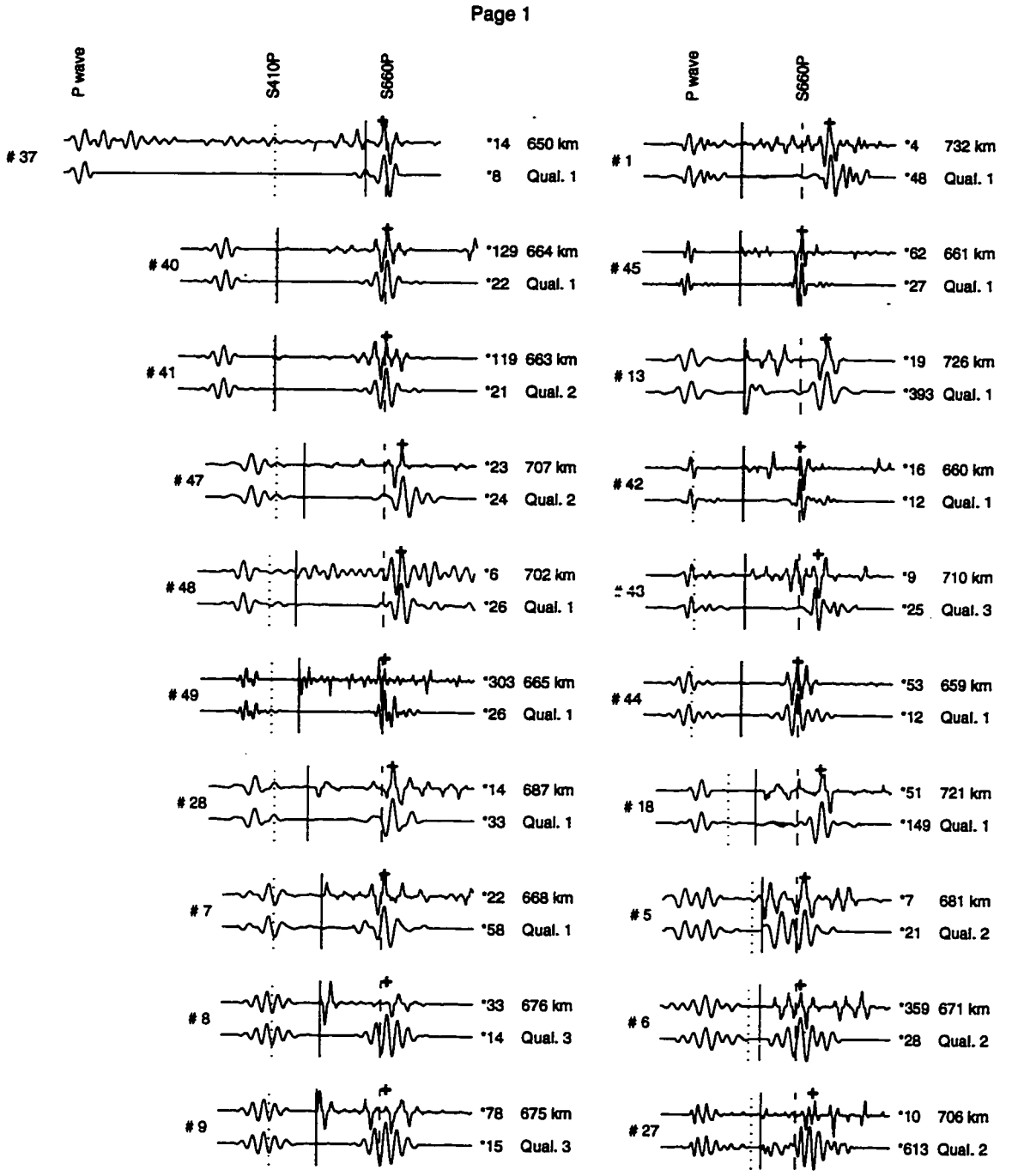

Figure 2.4a: Stacked data (top) and stacked WKBJ synthetics (bottom) for each event. Stacking algorithm is same as described for traces in Figure 3. P -wave stack is at far left. After the vertical bars, amplitudes are magnified by factor given to the right. The '+' indicates our time pick, the dashed line is the theoretical $S_{660}P$ arrival time, and the dotted line(s) mark the theoretical arrival time for the phase $S_{410}P$ for events above 410 km depth and the arrival times of $s_{410}P$ and $p_{410}P$ (which arrive at other slownesses) for events below 410 km. Event number, estimated discontinuity depth and quality are also shown. Time scale is at bottom of second page.

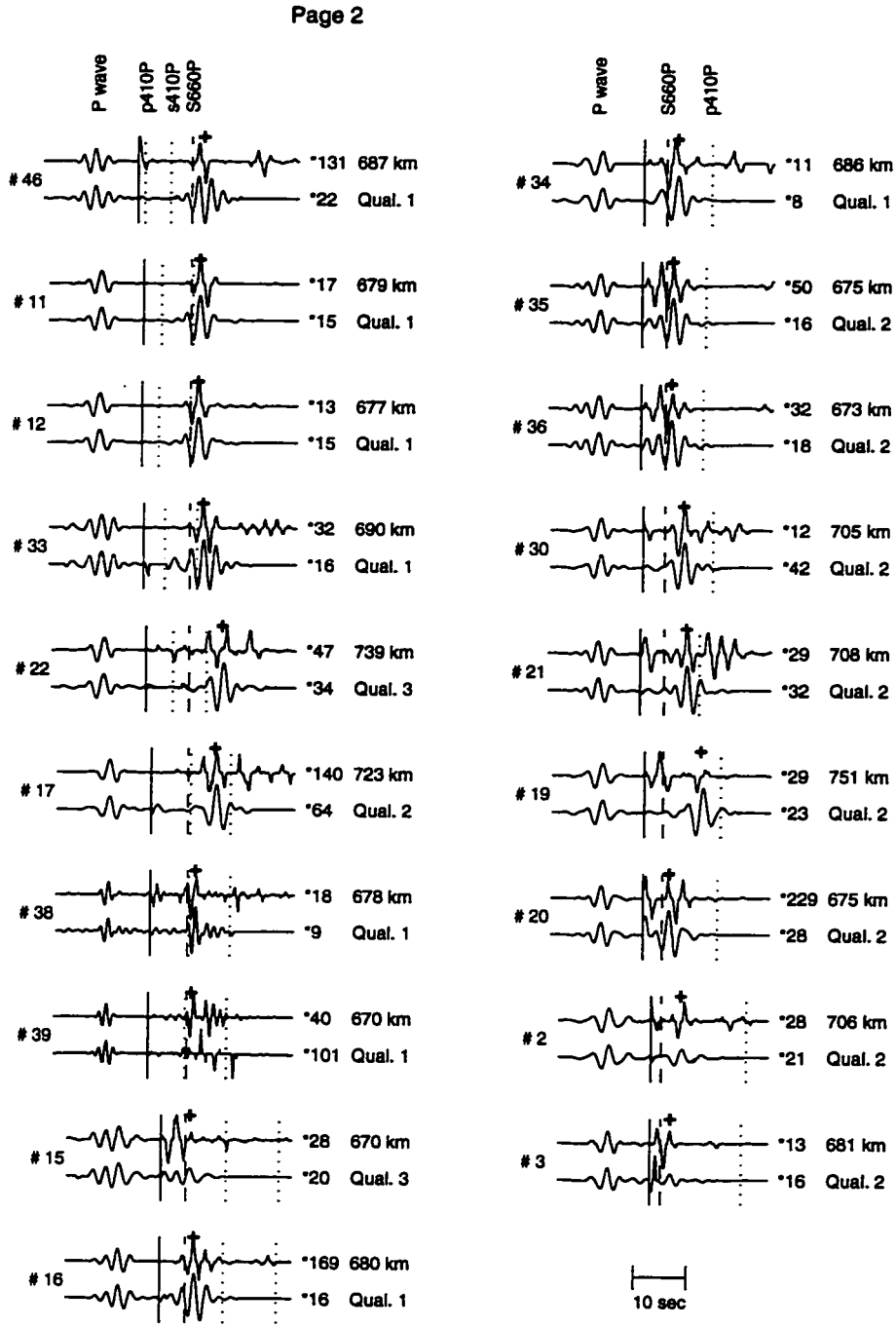

Figure 2.4b: (continued)

to minimize errors due to cycle skips, which could introduce a ± 20 km error in any single determination, we present the data so that the reader can make his or her own determinations. There is little ambiguity for most of the quality 1 picks, where picking uncertainties are typically a few tenths of a second leading to discontinuity depth uncertainties of a few km.

We observe no consistent discontinuity except for the 660-km discontinuity. Unlike longer period studies in the region [*Zhang and Lay*, 1993], the 210-km discontinuity is not observed in our data, which has a dominant period near 2 s, suggesting that the *PREM* model [*Dziewonski and Anderson*, 1981] exaggerates the sharpness of any change in shear-wave velocity near 210 km depth. While signals from the 410-km discontinuity have been used to map its topography [*Collier and Helffrich*, 1997], we rarely observe $S_{410}P$, $s_{410}P$, or $p_{410}P$ (dotted lines in Figure 2.4). The latter two phases leave an earthquake traveling upwards and reflect off of the 410-km discontinuity. Note that the stacks in Figure 2.4 are tuned to look for discontinuities below each earthquake and not for up-going phases which arrive at other slownesses. However, the stacked data rarely show arrivals from the 410-km discontinuity even when tuned to observe them. The absence of a consistent 410-km discontinuity near the slab can be explained by either significant topography on the discontinuity or by broadening of discontinuity to over 40 km width [*Helffrich and Wood*, 1996], either of which could reduce the amplitude of 10 km wavelength S waves. The lack of consistent later arrivals after $S_{660}P$ suggests that below the 660-km discontinuity, there exists no other sharp horizontal discontinuity to at least 1000 km [*Castle and Creager*, 1997]. Other distinct arrivals, observed inconsistently and at seemingly random times and slownesses after the $S_{660}P$ phase, can be explained by local 3-D non-horizontal structures [*Castle and Creager*, 1996; *Wicks and Weber*, 1996; *Kaneshima and Helffrich*, 1998]. These topics will be examined in detail in future work.

Returning to the $S_{660}P$ phase, it is observed in all but ten of our 65 stacked seismograms. The absence of the phase in eight of these ten events is explained

below. For events 14 and 29 the earthquake magnitudes are both less than 5.9 m_b (Table 2.2). Event 4 has an exceedingly long source time function and we therefore feel uncomfortable making a pick. The noisy stack of event 25 was recorded by only nine stations. For events 10, 24, 31, and 32, the expected ratios of S energy compared to P energy leaving the source toward the receivers, at the $S_{660}P$ and P wave take-off angles, respectively, are among the smallest of the events examined. Table 2.2 also lists the theoretical amplitude of the $S_{660}P$ phase relative to P , including the effects of the moment tensor and the S -to-P conversion coefficient at the discontinuity. For reference, if both the P -wave and S -wave were at their peak on the radiation pattern, then for an earthquake at 400 km depth traveling to a receiver at 80°, the theoretical amplitude would be 12%. Negative percentages indicate that the P wave and $S_{660}P$ wave have opposite predicted first motions, very small values (e.g., event 10) indicate that the S wave is nodal while exceedingly high values (e.g., event 39) indicate that the P wave is nodal. Finally, we rank each pick visually (1 (best), 2, or 3) based on the robustness of each time pick.

In addition to our data, we include 39 depths estimates from *Wicks and Richards* [1993] (Table 2.4) determined using the hypocenters from *Engdahl et al.* [1997]. *Wicks and Richards* used data from the small, yet extremely quiet, Warramonga Array in the Northern Territory, Australia. Where these additional points overlay our observations, the agreement is generally good, such that we feel confident combining these data sets. Our data for events 11 and 33 overlap the two $S_{660}P$ data points calculated in the Izu-Bonin region by *Vidale and Benz* [1992] with linear stacking. Our estimates of 679 km and 690 km are very close to their results of 677 km and 686 km. We have improved on other work [*Vidale and Benz*, 1992; *Wicks and Richards*, 1993; *Kawakatsu and Niu*, 1994; *Collier and Helffrich*, 1994] by our combined use of additional large-aperture network data, which is now readily available at the *IRIS* data center, and the N^{th} root slant-stacking algorithm, allowing us increased slowness and time resolution and greater noise reduction.

Table 2.4: *Wicks & Richards* (1993) earthquakes and $S_{660}P$ points

Event	Lat	Lon	Depth	Original			Migrated (this study)		
No	°N	°E	km	Lat	Lon	Depth	Lat	Lon	Depth
50	28.02	139.98	458	27.0	139.8	688.5	26.9	140.2	684.4
51	27.50	140.02	474	26.5	139.9	694.2	26.5	140.0	692.6
52	29.71	138.88	448	28.6	138.8	713.1	29.2	139.0	701.1
53	29.30	138.77	485	28.4	138.7	690.2	28.2	138.3	682.8
54	28.36	139.66	442	27.2	139.5	704.2	26.9	139.6	700.7
55	28.36	138.93	540	27.7	138.8	695.5	27.4	138.6	690.2
56	28.87	139.73	425	27.7	139.6	705.1	27.7	139.8	703.0
57	28.46	138.44	535	27.8	138.4	676.2	27.8	138.1	671.0
58	28.11	139.92	449	27.1	139.8	690.4	26.9	140.2	684.6
59	28.51	139.81	403	27.2	139.6	703.0	27.1	140.0	699.1
60	30.34	138.40	458	29.4	138.3	685.0	29.1	138.4	680.9
61	27.91	137.03	548	27.4	137.0	665.4	27.3	137.0	663.9
62	28.66	138.16	519	28.0	138.1	671.7	27.9	138.0	669.5
63	30.50	138.31	443	29.4	138.2	694.2	29.4	138.2	693.6
64	28.67	139.48	452	27.7	139.3	689.1	27.4	139.1	684.5
65	28.70	139.34	474	27.8	139.2	693.0	27.5	139.0	688.3
66	29.96	138.99	438	28.9	138.9	686.4	29.2	139.2	679.6
67	28.08	139.41	524	27.4	139.3	685.3	27.3	139.2	682.5
68	28.32	139.93	464	27.3	139.8	691.9	27.2	140.2	686.0
69	28.14	139.35	531	27.4	139.3	697.7	27.2	139.1	694.8
70	27.18	139.91	511	26.4	139.8	683.2	26.4	139.8	682.3
71	27.41	139.97	485	26.5	139.8	693.9	26.3	140.0	690.8
72	28.22	138.95	534	27.6	138.9	684.6	27.4	138.6	680.1
73	33.33	137.89	343	31.9	137.8	713.5	32.0	137.4	710.4
74	31.14	138.59	399	30.0	138.5	683.6	29.9	138.5	682.6
75	30.96	138.55	391	29.6	138.4	722.5	31.0	138.5	676.7
76	32.16	137.69	402	30.8	137.6	729.6	30.6	137.2	725.4
77	32.95	138.51	304	31.6	138.4	659.7	31.6	138.5	658.5
78	31.57	138.34	380	30.3	138.2	699.4	30.9	138.4	688.9
79	31.46	138.73	343	30.2	138.6	664.2	30.0	138.6	661.8
80	32.94	137.77	349	31.5	137.7	714.0	32.0	137.4	707.0
81	33.28	136.03	432	32.1	136.0	717.1	32.0	136.2	715.0
82	33.65	136.11	410	32.3	136.1	731.7	32.1	136.2	729.7
83	32.33	137.76	382	31.1	137.7	678.5	31.3	138.2	671.3
84	33.12	137.81	348	31.7	137.7	700.8	31.8	138.3	693.1
85	33.67	137.92	316	32.1	137.8	712.7	32.0	137.4	710.3
86	31.28	138.28	406	30.1	138.2	683.2	30.0	138.4	680.2
87	30.08	138.57	448	29.1	138.5	681.7	29.1	138.5	681.1
88	34.38	136.42	364	32.9	136.3	724.6	32.7	136.8	719.5

We have determined our $S_{660}P$ conversion locations by interpreting arrivals times using a radial Earth model. There are three possible biases: 1) earthquake mislocation, 2) aspherical slab structure, and 3) a dipping 660-km discontinuity. To minimize mislocation errors, we use relocated hypocenters [*Engdahl et al.*, 1997], determined by employing an iterative procedure that reassociates arrival times in the ISC catalog with the appropriate phase among *P, pP, pwP,* and *sP*. This procedure dramatically reduces the errors in hypocentral depth estimates. *Engdahl et al.* estimate their errors globally at ± 15 km globally. In the Izu-Bonin region, however, the error for deep earthquakes is significantly smaller and is likely less than 2 km [*Wicks and Richards*, 1993a, *Engdahl et al.*, 1997].

We also calculate the effect of a 4% velocity anomaly, such as in a cold, fast slab or in a slow piece of meta-stable, untransformed olivine [*Green et al.*, 1990; *Kirby et al.*, 1991]. For an earthquake at 400 km, should the *S* and *P* waves travel through 250 km of material with a 4% velocity anomaly, the result would bias the discontinuity depth by only 10 km. This bias becomes even smaller with increasing hypocenter depth, which are the events where we generally see the most depression. Additionally, along ray paths traveling through fast material, such as the slab, the relative $S_{660}P$ -*P* travel time will decrease and move the apparent discontinuity to shallower depths. However, along ray paths to Germany which travel closer to the slab than rays to North America, we observe no systematic shallowing of the discontinuity.

2.5 *Data migration to account for 660-km discontinuity topography*

For each event, we use the $S_{660}P$ - *P* delay times and source-receiver geometry to estimate the depth, latitude, and longitude of the ray intersection point with an assumed horizontal discontinuity (Tables 2.3 & 2.4). However, the systematic variations in estimated depth as a function of latitude and longitude suggest that this discontinuity exhibits substantial topography.

The topography of the discontinuity will bend rays out of the paths predicted by ra-

dially symmetrical models. To better image the surface, we take 3-D ray bending into account by employing a migration algorithm. The timing of an $S_{660}P$ arrival determines an isochronal surface, similar in appearance to that of an "egg shell" surrounding the earthquake (Figure 2.5). Converted S -to-P waves generated at any point on this surface will satisfy our time observation. Importantly, the tangent plane to each point on the isochronal "egg shell" is the unique surface which satisfies Snell's Law for the incoming and outgoing rays [*Salas et al.*, 1986]. By precisely measuring the slowness and azimuth along which the $S_{660}P$ wave arrives, we could trace the ray back from the stations towards the source to determine the location on the surface where the conversion takes place. While this procedure is effective at imaging lower-mantle structures where the "egg-shell" is far from the source [*Castle and Creager*, 1996b], it is not effective for this problem because the uncertainty in ray angles at the receiver arrays ($\pm$ 1°) maps to uncertainties of order 100 km on the "egg shell". These 100-km uncertainties map into larger uncertainties in ray take-off angles at the source when the scatterer is closer to the source.

To use our migration scheme, we start by determining a preliminary 660-km discontinuity surface from the points calculated assuming a locally horizontal discontinuity. To avoid spatial aliasing, we weight each estimated depth by the inverse of its quality (we assign *Wicks and Richards* points a quality of 2) and average the depths on a 0.5° evenly spaced grid. A smooth surface, $z(x, y)$, is created from the gridded data by solving:

$$(1 - T) * L(L(z)) + T * L(z) = 0 \tag{2.2}$$

where L is the surface Laplacian operator and T is a tension factor between 0 ("minimum curvature") and 1 ("harmonic surface"); we empirically use T = .40 [*Wessel and Smith*, 1995]. We next calculate the isochronal "egg shell" for each source/receiver pair using the observed delay time. We then iteratively migrate our conversion points. This is done for each observation separately by varying the latitude

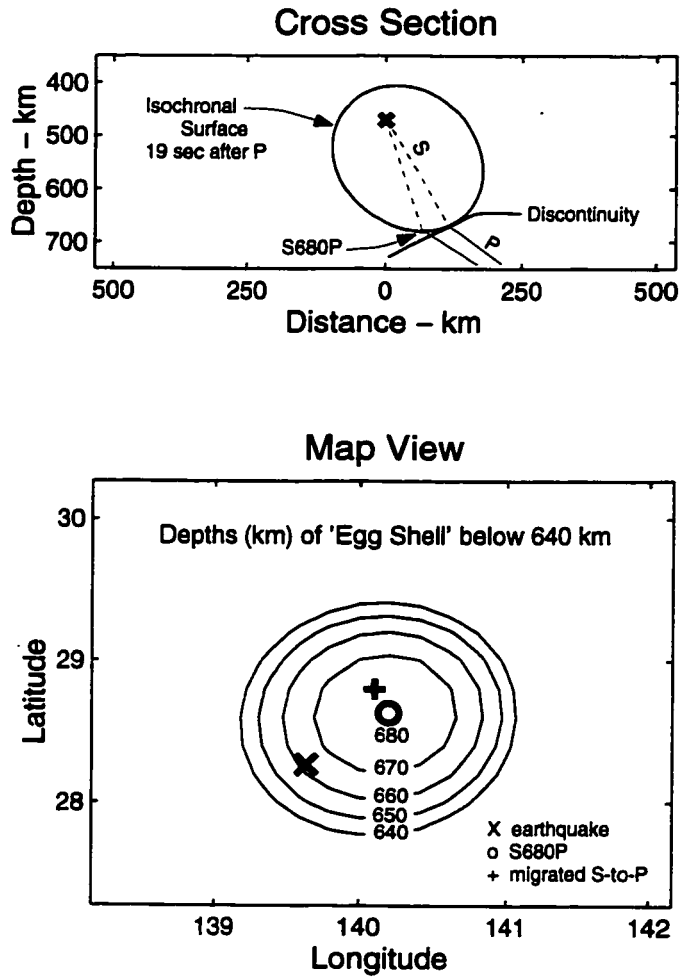

Figure 2.5: (a) Cross section of the 19 second S -to-P isochronal 'egg shell' surface around event 15 and a hypothetical discontinuity; and (b) a map view of the isochronal surface, showing the earthquake location ('x'), the conversion point at 680 km depth for a horizontal discontinuity ('o'), and the 3-D migrated location ('+').

and longitude of conversion points to minimize

$$(S - E)^2 + \gamma^2 |\nabla S - \nabla E|^2 \tag{2.3}$$

where S (km) is the discontinuity surface determined in the previous iteration and E (km) is the surface of the "egg shell", the gradients are unit-less, and we empirically use $\gamma = 70$ km/rad $= 1.2$ km/°. This migration matches the depth of the points "egg shell" to the discontinuity surface (the terms on the left hand side) and the gradient

of each "egg shell" to the gradient of the discontinuity surface (Figure 2.5).

This migration procedure is applied to the Izu-Bonin arc region, where the sampling is dense. After the migration calculation, we have 78 migrated conversion points in the Izu-Bonin region (Tables 2.3 and 2.4). The standard deviation of the misfit in discontinuities depths $(S - E)$ falls from 8.6 km for the unmigrated points to 5.2 km for the migrated points, while the standard deviation of misfit in discontinuity slopes $|\nabla S - \nabla E| * 180/\pi$ decreases from 4.8°to 3.7°. The migration algorithm changes the depth of the points an average of -5 km (note that every point is moved to a shallower depth), while the mean change in horizontal locations are less than 1 km. The root-mean-square changes in latitude and longitude are 18 and 26 km respectively.

From these 78 migrated data points, we create a topography map of the 660-km discontinuity surface (Figure 2.6). Comparing this map to the map of the 660-km discontinuity surface generated using unmigrated points (not shown), the final interpretation using either map would be identical. The migration technique does create a smoother map. Finally, this method attempts to migrate each $S_{660}P$ arrival to only one location on the discontinuity, ignoring the possibility of arrivals being generated at multiple locations on the discontinuity. For the best data (such as event #12), the $S_{660}P$ and P waveforms match, suggesting that either no multi-pathing exists or that the multiples arrive within $^1/_4$ period (0.5 s) of each other. Future work could model the entire waveform using 3-D discontinuity models.

2.6 Discussion

2.6.1 Discontinuity depth under Ryukyu, Japan and Marianas

In addition to the dense set of observations under Izu-Bonin, we have estimated depths to the 660-km discontinuity in 16 other locations (Table 2.1). We make one observation near the Marianas Trench, six to the southeast near Taiwan and the Ryukyu Trench, and nine under the Sea of Japan. For each group, we compare the points to the expected slab location at 660 km, extrapolated from shallower seismicity.

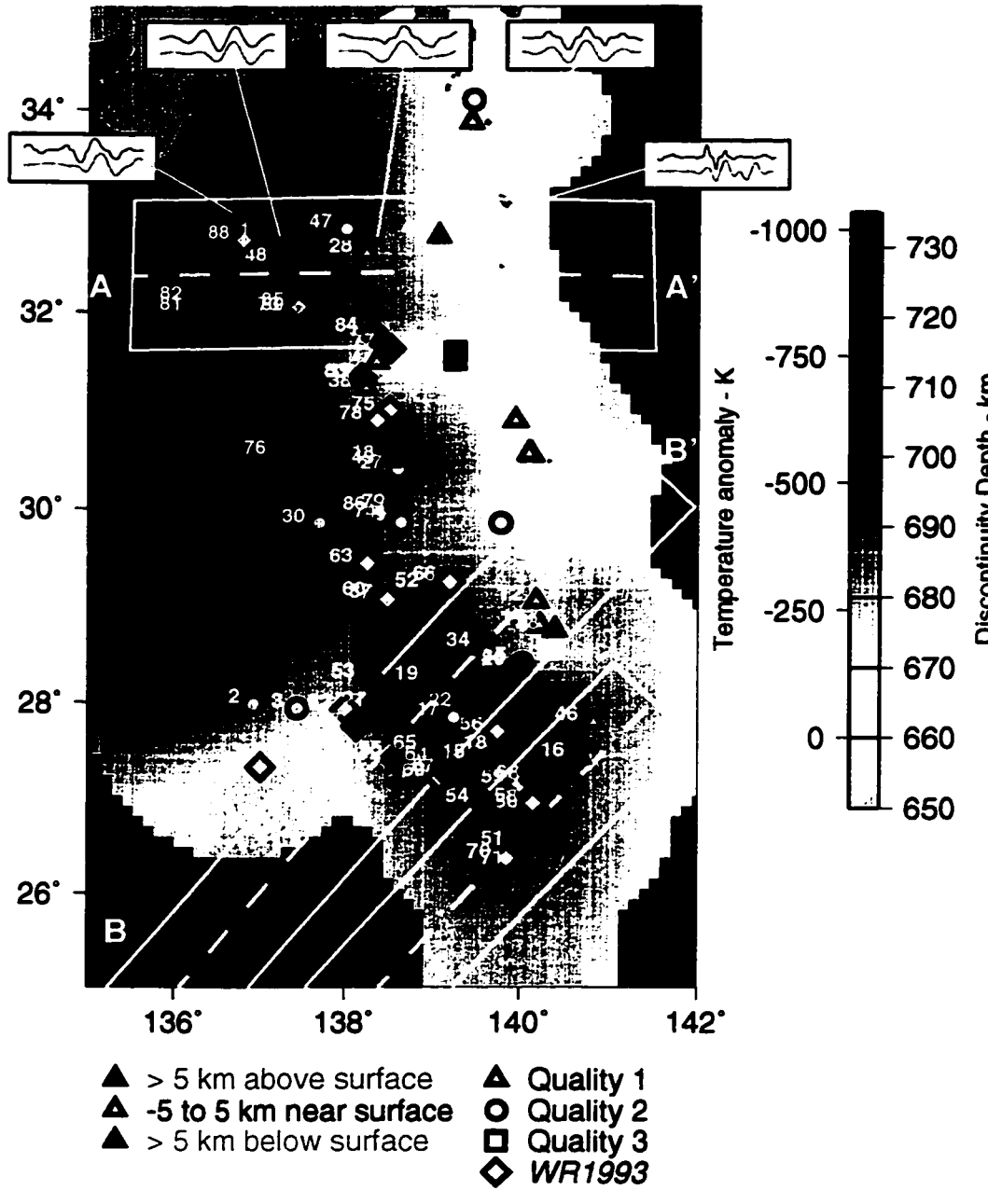

Figure 2.6: The 78 migrated data points, the surface they define, and the location of three cross sections. '△' are quality 1 picks, 'o' are quality 2, '□' are quality 3, and '◇' are *Wicks and Richards* picks, all of which have been migrated to these locations. Red symbols are those more than 5 km above the surface, blue are more than 5 km below the surface, and yellow symbols are within 5 km of the surface. Ten second windows of stacked seismograms (top) and stacked synthetics (bottom) are shown for events #1, 28, 40, 48, and 49. The 660-km discontinuity depth is converted to a temperature scale using a Clapeyron slope of -2.8 MPa/°K.

The point near the Marianas Trench images the discontinuity over 100 km westward of the almost vertical slab and is at a depth of 670 km. Along the Ryukyu Trench, the points image the discontinuity far to the east of the slab and have an average depth of 654 km, not including one point farther to the east and closer to the slab at a depth of 700 km. Farther to the north and over 600 km to the east of the slab - 660-km intersection, the average depth under the Sea of Japan is 664 km, while one point within 300 km of the slab has a depth of 706 km. Taken together, these data image a discontinuity that is at an average depth of 661 km away from subducting slabs.

2.6.2 Discontinuity depth under Izu-Bonin

Figure 2.6 shows a map of our migrated 660-km discontinuity surface. The depths of the surface range from 650 km to 745 km, similar to work done in the Tonga subduction zone [*Niu and Kawakatsu*, 1995], and imply, using a Clayperon slope of -2.8 MPa/K, temperature variations relative to ambient mantle of 150° to -1100°K.

We compare our results to the recent tomographic compressional-wave velocity model *Widiyantoro* [1997] constructed using millions of P and pP travel times and block sizes of 1°; Figure 2.7. Figure 2.8 shows three cross-sections. The solid line shows the depth of the 660-km discontinuity, along with the data points, and the color shows the P wave velocities anomalies from the tomographic model. The symbol size is roughly equal to the maximum expected error of ±15 km. For the quality 1 data, the time-pick uncertainties are only 0.2 s, or 2 km. The primary source of error is from inexact knowledge of upper-mantle seismic wave speeds which cause errors in earthquake depth estimates, as well as in converting $S_{660}P$ -P delay times to source-to-discontinuity depth differences. Whereas we estimate that the absolute uncertainties in discontinuity depths are as large as ±15 km, the rms variability between all our estimates and the resulting topography model is only 5 km, suggesting that the relative errors may be as small as ±5 km.

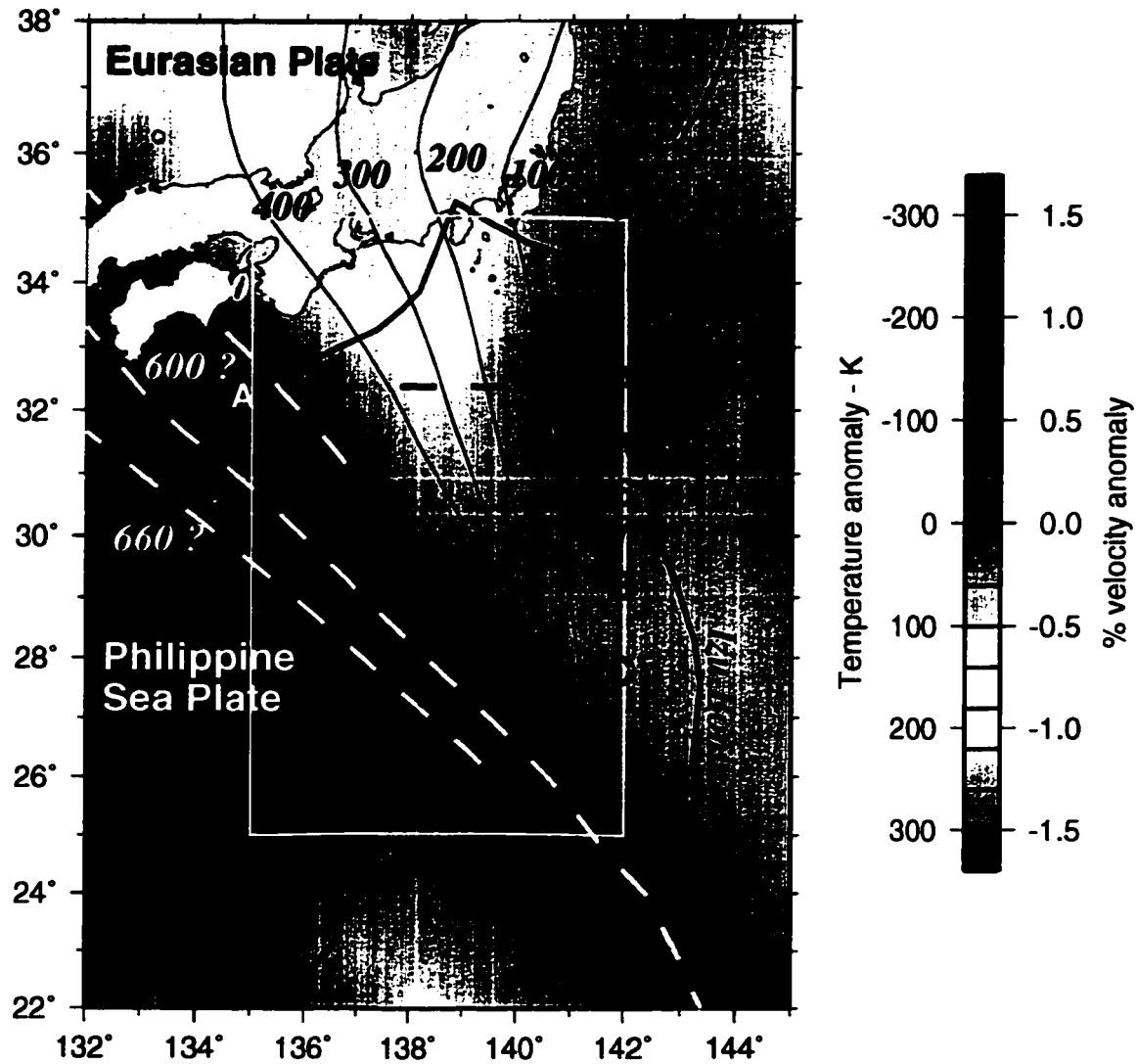

Figure 2.7: The tomographic image of P wave velocities at 700 km [*Widiyantoro*, 1997], seismicity contours (dashed lines indicate extrapolations), the relative Pacific/Philippine Sea Plate motion [*Seno et al.*, 1993] (blue), the "no-net rotation frame" absolute motion of the Pacific Plate [*Gordon*, 1995] (red), and our study region (white rectangle). The velocity anomaly scale is converted to a temperature scale using a thermal coefficient of velocity of -0.0005 km/s/°K, consistent with residual-sphere modeling and mineral physics data [*Creager and Jordan*, 1986].

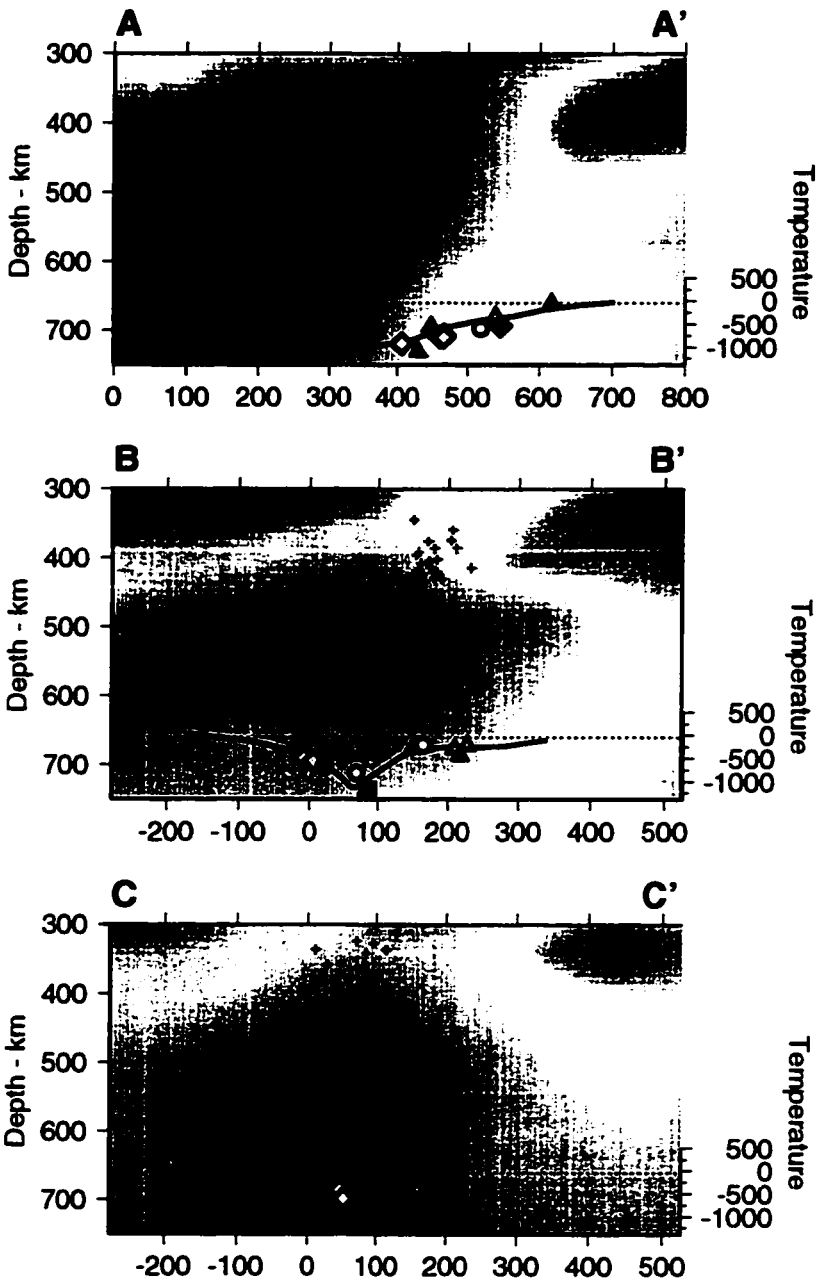

Figure 2.8: Three cross sections and adjacent migrated data points. The symbol size represents the vertical error bars and the symbols are as in Figure 2.6. The background color is the tomographic model of [*Widiyantoro*, 1997] and the color scale is as in Figure 2.7. Also shown are earthquake locations and the average discontinuity depth.

The discontinuity topography and the tomography results, determined from independent data sets, agree well. To the north, near cross section AA', a broad depression of the discontinuity to the west in the topography (cold temperatures) corresponds to a broad region of fast (cold) material in the tomographic model. At BB', the depression of the discontinuity is concentrated in a narrow band. In the tomography model (with 1°block sizes), BB' marks the transition from a broad horizontal fast zone to the zone near CC', where the fast velocities in the tomographic model are correspondingly concentrated in a narrow band (see also Figure 2.7).

2.6.3 Amplitude of depression

Along cross section AA' and BB' the maximum depression of the discontinuity is 745 km, representing a 85 km downward deflection of the discontinuity from the average depth of roughly 660 km found in long-period studies [*Revenaugh and Jordan*, 1991; *Flanagan and Shearer*, 1997] and corresponds to a thermal anomaly of -1100° K. Models of subduction of old, cold lithosphere for this part of the world predict thermal anomalies of about -900°K at 660 km depth [*Creager and Jordan*, 1986; *Helffrich et al.*, 1989] if shear-strain heating is not important and the slab subducts with only minor deformation. This deflection is consistent with previous estimates in Izu-Bonin and Tonga [*Vidale and Benz*, 1992; *Wicks and Richards*, 1993; *Niu and Kawakatsu*, 1995].

2.6.4 Slab thickening and penetration into the lower mantle

Thermal models of steady-state flow characterized by little internal slab deformation predict (1) a maximum temperature anomaly of -900°K at 660 km depth [*Creager and Jordan*, 1986], and (2) a slab width of 120 km at 660 km depth as measured by the distance between the -400°K thermal anomaly isotherms [*Creager and Jordan*, 1986; *Helffrich et al.*, 1989]. Resolution of most tomographic models and effects of ray bending by three-dimensional variation in velocity structure (e.g., *Fischer et al.* [1988] and *VanDecar* [1991]) make slab width a very difficult parameter to estimate

using seismic travel times alone. Along cross section BB' the observed slab width of about 100 km is in good agreement with slab width estimated from the thermal calculations. The lack of depression of the discontinuity to the west implies that no cold slab material is there and thus the slab appears to penetrate vertically beneath the deepest seismicity into the lower mantle at 27°N, 140°E with little or no advective thickening. This is also consistent with the tomographic images in *van der Hilst et al.* [1991] and *Widiyantoro* [1997] (Figures 2.7 and 2.8) which show narrow, near vertical downwelling deep into the lower mantle beneath the Marianas and southern Izu-Bonin island arcs.

In contrast, at 32°N, along section AA' the discontinuity gradually deepens from 650 km at 139°E to 730 at 136°E. The seismograms shown in Figure 2.6 resolve this consistent trend especially well. The same waveform shape of the observed $S_{660}P$ phase (solid) and the theoretical $S_{660}P$ phase (grey line) make the picks here unambiguous. Recall that the theoretical $S_{660}P$ gets its shape from the P wave. There is no cycle skipping ambiguity, and the relative timing can be picked to within a tenth of a second which translates to depth uncertainties of one km. The width of the depression along AA' is at least 200 km, but unfortunately the data do not extend far enough west to determine where the discontinuity returns to normal depths. As noted above, the mean depth beneath the Ryukyu Islands is 654 km (Table 2.1). The closest sampling point to Izu Bonin is only 600 km west of the sampling points in AA' (Figure 2.2). Thus, the depressed region is at least 200 km wide, but not more than 800 km.

This is also consistent with tomographic imaging [*Okino et al.*, 1989; *van der Hilst et al.*, 1991; *Widiyantoro*, 1997] and waveform modeling results [*Tajima*, 1997; *Brudzinski et al.*, 1997] which are interpreted in terms of the Izu-Bonin slab laying flat near the base of the upper mantle, and not penetrating simply into the lower mantle. *Van der Hilst and Seno* [1993] suggest that the very rapid retreat of the Izu-Bonin trench to the east by 2000 km has laid the slab down flat on the 660-km discontinuity.

Our topography estimates are consistent with this inference. Furthermore, numerical modeling of slab dynamics [*Christensen*, 1996] shows that slabs are expected to lay out flat on an endothermic phase change at 660 km if the trench retreats rapidly, as is the case for northern Izu-Bonin.

If the slab penetrates into the lower mantle at the southern end of the arc while laying out flat farther to the north, the slab must be torn. From the topography map (Figure 2.6), it appears as if this tear may exist near 29.5°N, 138.5°E. This is the same tear hypothesized in a cartoon based on earlier tomography studies in this region [*van der Hilst and Seno*, 1993].

2.6.5 Depression directly beneath deepest seismicity

Among the most intriguing results of this study is the 660-km discontinuity depression located directly below the deepest seismicity. This is displaced 150 km (at BB') to 500 km (at AA') to the east of where we would have expected it to be based on extrapolations of seismicity (Figure 2.8). We draw seismicity contours based on the *Engdahl et al.* [1997] catalog of relocated hypocenters and do a three-dimensional extrapolation to depths below the seismicity cutoff (Figures 2.2 and 2.8). Note that the deepest seismicity at BB' is 550 km, and the seismicity cutoff progressively shallows to the north reaching only 450 km at AA'. Thus, the 600 and 660 km contours are extrapolated everywhere, and the 500 km contour is an extrapolation north of 31°N. Rather than continue on the trajectory of the shallower seismicity, which is dipping about 45°along AA', the slab appears to bend sharply at the depth of the seismicity cutoff and fall straight down to cause the observed depression of the 660-km discontinuity.

In order to understand the significance of this observation we review other aspects of the Izu-Bonin Wadati-Benioff zone seismicity. First, based on the old age of subducting lithosphere and the rapid rate of convergence, *Kirby et al.* [1996] argue that this slab should be colder to greater depths than any other slab except the

Tonga slab. It is therefore highly anomalous that the seismicity cuts off at depths well above 650 km. Second, the largest earthquakes, as well as the largest concentration of earthquakes, occur near the base of the seismogenic zone along the strike of Izu-Bonin[*Kirby et al.*, 1996]. Additionally, the depth of the seismicity cutoff varies from nearly 600 km at 24° N to less than 400 km at 36°N. Third, subduction along the trench is oblique which is most pronounced at the southern edge, south of 23°N (Figure 2.7). Fourth, while focal mechanisms of deep earthquakes in Izu-Bonin are more varied than for many other subduction zones [*Lundgren and Giardini*, 1992], they do show predominantly down-dip compression. However, the deepest events show consistent along-strike tension [*Green and Houston*, 1995], while events more than 100 km shallower than the seismicity cutoff show along-arc null. A set of deep events show internal shear of the slab such that the deeper part of the slab moves south relative to the shallower part [*Lundgren and Giardini*, 1992]. Finally, this region has seen rapid trench migration to the east from 48 Ma to 17 Ma followed by slow westward migration [*van der Hilst and Seno*, 1993].

The internal shear can be explained by the oblique subduction (Figure 2.7). The observation that the shear is concentrated at great depth can be explained by either increasing mantle viscosity with depth, or by decreasing slab strength. In either case, the observation that it is concentrated deep in the slab suggests that the slab above the seismicity cutoff has significant membrane strength.

The overall shape of the Japan-Izu-Bonin-Mariana slab is such that in a steady state flow, the strain required to get from the spherical shell of the oceanic lithosphere into the observed geometry requires large along-strike extensional strains somewhere between the Izu and Marianas trenches [*Yamaoka and Fukao*, 1986; *Burbach and Frohlich*, 1986]. In fact, the inferred membrane strain for this region is among the largest for all subduction zones. This geometric problem is apparently manifested in the slab tear postulated above at 29.5°N and in the along-strike tension axes of the deepest focal mechanisms. As argued by *Creager and Boyd* [1991] for the Aleutian

Arc, which also exhibits along arc extension, the ideal slab geometry has a shallower dip. While gravity pulls the slab down, it is primarily the membrane strength of the slab that keeps it from bending to a near vertical dip everywhere.

We postulate that all these observations are closely related to the mechanism that causes deep earthquakes. One possibility for the deep earthquakes is that the slab is unstable, perhaps due to oblique subduction, membrane stretching, or the complex history of trench migration. Some combination of factors forces higher strain rates in the slab, causing more heating and bringing the temperature of the slab to the point where the over-driven olivine to spinel phase transition goes to completion at shallower than normal depths. This scenario would produce extra seismicity just prior to the seismicity cutoff [*Green and Houston*, 1995; *Kirby et al.*, 1996] , and may temporarily weaken the slab, producing the bend to a steeper dip at the seismicity cutoff. One mechanism for weakening the slab is transformational faulting which is postulated to produce very small olivine grains facilitating deformation until they grow to larger sizes, especially in cold slabs [*Riedel and Karato*, 1997]. Most dynamic 2-D calculations give the slab minimal bending strength such that slabs should tend to bend and subduct vertically. We suggest that it is the membrane strength that holds slabs from going vertical. Once this membrane strength is lost, even temporarily, the slab turns to a vertical dip and heads straight down. Note also that both residual-sphere [*Creager and Jordan*, 1986] and high-resolution tomographic imaging [*van der Hilst et al.*, 1991; *Widiyantoro*, 1997] show the Kuril and Japan slabs also bend to significantly steeper dips at the depths of their seismicity cutoffs.

2.7 Conclusions

We apply stacking and migration algorithms to over 5,000 waveforms, to produce a fine scale image of the topography of the 660-km discontinuity in the Izu-Bonin region. The topography map, where a depressed discontinuity indicates cold material, is consistent with tomographic images, with fast wave speeds in regions of cold tem-

peratures. The 660-km discontinuity is locally depressed up to a maximum of 85 km, which is consistent with a cold thermal anomaly of order 1100°K. The width of the depression is only about 100 km at 28°N, consistent with slab penetration into the lower mantle with no advective thickening. On the other hand, width of depression at 32°N is over 200 km, consistent with the slab having been laid down flat on the 660-km discontinuity as the trench retreated 2000 km eastward [*van der Hilst and Seno*, 1993]. All along the arc, the depression occurs directly beneath the deepest earthquakes. Apparently, the slab fails and bends to a vertical dip at the deepest seismicity. This failure involves a physical process which causes the seismicity to increase dramatically and then abruptly cease. The slab failure may be due to either a loss of membrane strength resulting from small grain sizes or buoyancy effects due to a density increase from the olivine-spinel transformation.

2.8 Acknowledgments

We thank C. Wicks, J. Vidale, R. Engdahl for data, S. Widiyantoro and R. van der Hilst for access to their unpublished tomography model, M. Flanagan, J Vidale, and J. Revenaugh for constructive reviews, the staff at the data centers in Seattle (IRIS and PNSN), in California (NCSN and SCSN), in Erlangen, Germany (GRSN), and in the United Kingdom (Blackness), and the producers of *GMT* [*Wessel and Smith*, 1995]. Funding was provided by the National Science Foundation and by a Fulbright Scholarship to ANU, Australia (JCC).

Chapter 3

NW PACIFIC SLABS STEEPEN AT SEISMICITY CUTOFF

3.1 Abstract - change in slab rheology due to deep earthquakes

One of the most interesting findings of *Castle and Creager* [1998] (chapter 2) was that the subducting plate bends to a vertical dip at the deepest earthquakes. This change in dip occurs along the entire Izu-Bonin trench, regardless of the depth of the seismicity cutoff or the dip of the slab above the cutoff.

In this chapter I expand and further investigate (1) deep earthquakes in the Mariana-Bonin-Izu-Japan-Kuril subduction system, (2) the subducting slab dip along the arc, and (3) possible connections between the two.

The largest deep earthquakes (depth greater than 300 km) invariably occur near the depth of the seismicity cutoff, regardless of whether the cutoff occurs at 400, 500, 600, or 650 km depth. Data from $S_{660}P$ arrivals, residual sphere analyses, and tomographic studies show that the slab consistently changes to a vertical dip at the seismicity cutoff. We hypothesize that the earthquakes are connected to the olivine to spinel phase change and that the slab dip steepens as a result of a weakening caused by at least one of the following: [1] a loss of membrane strength due to large earthquakes, [2] a density increase due to the phase change, or [3] a grain size reduction and subsequent loss of strength due to the phase change.

3.2 Deep earthquakes

The old age of the subducting Pacific Plate and the rapid rate of subduction create an extremely cold slab [*Kirby et al.*, 1996]. Ensuing, earthquakes should occur to the

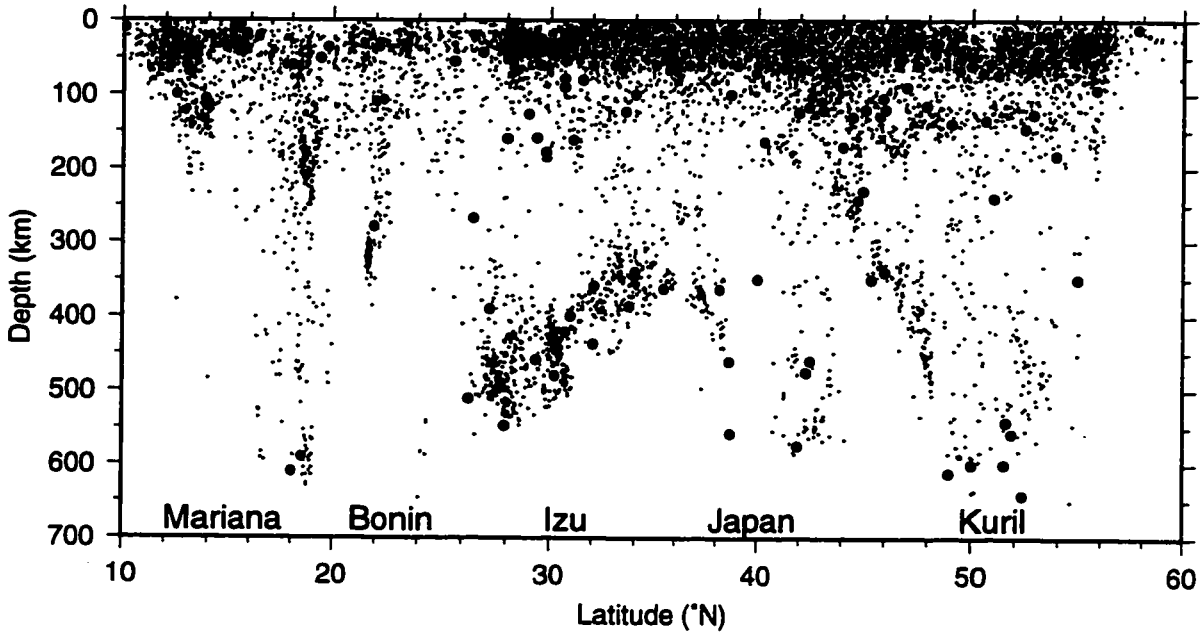

Figure 3.1: Western Pacific earthquakes. A • marks large earthquakes with moments greater than 5.9 Mb. The figure is modeled after *Kirby et al.* [1996]

bottom of the transition zone along the entire arc. Interestingly, the depth of the deepest earthquakes varies considerably along the arc, ranging from about 350 km between the Japan and Kuril trenches to 650 km in the Mariana and Kuril trenches (Figure 3.1). Also interesting is that, outside of the shallow seismicity between 0 km and 200 km, the deepest earthquakes are the largest at each point in the arc.

Not only are they larger, the deepest earthquakes have different stress orientations. Figure 3.2 shows the stress orientations of the earthquakes in the Izu-Bonin region [*Dziewonski et al.*, 1981, *Green and Houston*, 1995]. The pressure (P) and extensional (T) axes are plotted along and perpendicular to the slab. Below 100 km, the orientation of the maximum compressive stress rotates to down-dip compression (Figure 3.2, upper left plot). Two related explanations of the down-dip compression include: [1] resistance to penetration into the lower mantle [*Lundgren and Giardini*, 1992] and [2] compressive stresses from buoyancy effects due to thermal perturbations

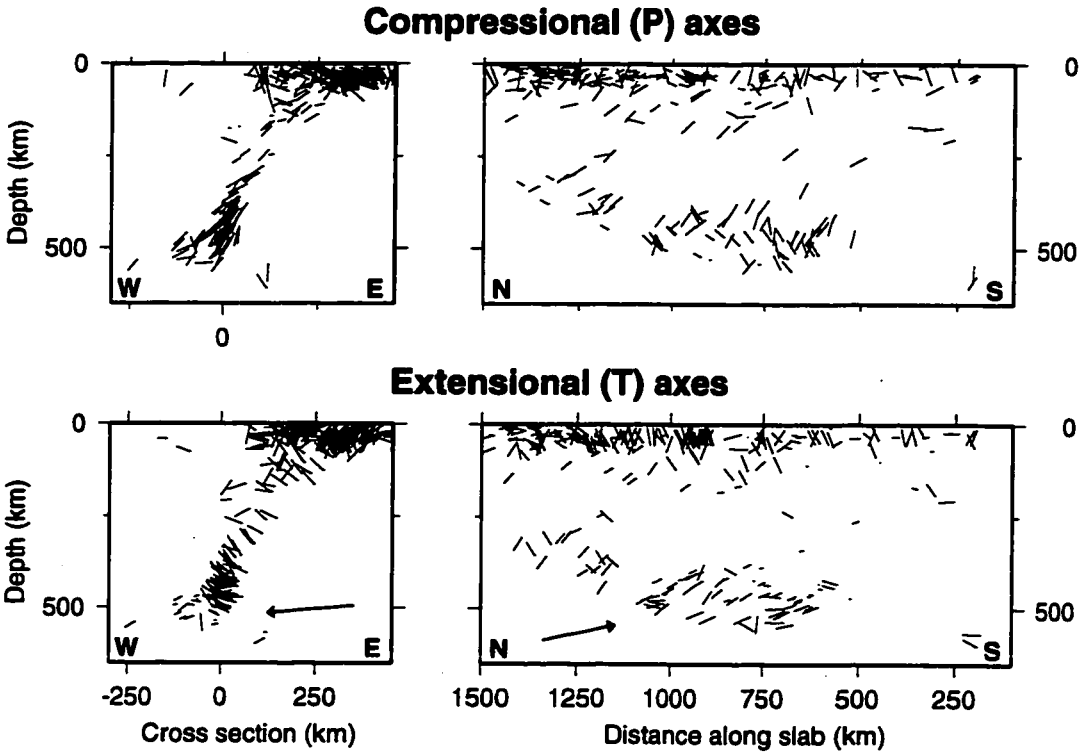

Figure 3.2: Izu-Bonin earthquake stress orientations from the Harvard CMT catalog [*Dziewonski et al.*, 1981]. P is maximum compression axis and T is the maximum extension axes. The length of the symbol is proportional to the length of the vector in the given plane. The distances along the ordinate are measured from 22°N, 142°E parallel and perpendicular to 340°, roughly the strike of the trench. The figure is modeled after *Green and Houston* [1995] .

of the 410-km discontinuity (upwards) and 660-km discontinuity (downwards) resulting from the cold subducting slab [*Bina*, 1997]. The T-axes of these same earthquakes (Figure 3.2, lower left plot) show extension predominately perpendicular to the plane of the slab, as would be expected from simple 2D flow models (e.g. *Kincaid and Olson* [1987]).

However, the earthquakes below 500 km are unlike the shallower seismicity. The strike of the Izu-Bonin trench, at roughly -20°W of N, and the convergence between the Pacific and Philippine Plate, which is -66°W of N [*Seno et al.*, 1993] (Figure 2.7), create a region of oblique subduction, which causes along-arc shear deformation at depth [*Lundgren and Giardini*, 1992]. The T-axes of the deepest earthquakes (Fig-

ure 3.2, lower plots, arrows) change considerably from the seismicity directly shallower. There is almost no shear perpendicular to the slab (Figure 3.2, lower left) and much more shear along the strike of the slab (Figure 3.2, lower right). Therefore, the seismicity is either indicative or causal of a weakening in the slab, allowing it to respond to stresses originating from the oblique subduction.

The slab weakening could be either a weakening relative to the ambient mantle or a weakening within the slab. The viscosity of the mantle appears to increase with depth [*Hager and Richards*, 1989], providing one explanation for the down-dip compression generally observed for deep earthquakes. However, while upper mantle viscosity structure is still poorly constrained, the radial variations in the upper mantle viscosity are likely minor compared to the jump predicted at the 660-km discontinuity [*Thoraval and Richards*, 1997]. If true, that these earthquakes are at least 100 km above the lower mantle suggests that the change in extensional axes is not due to external viscosity changes but rather associated with an internal change in slab rheology.

3.3 Slab geometry

Along the entire Mariana-Bonin-Izu-Japan-Kuril arc, the slab bends to vertical or nearly-vertical at the depth of the deepest seismicity. The evidence for this observation comes from the seismicity itself, $S_{660}P$ arrival times analysis, residual sphere analysis, and regional tomographic studies.

Mariana trench

The dots (•) in cross section DD', Figure 3.3, [*Creager and Jordan*, 1986], show the seismicity beneath the Mariana trench (note that the depth labels are 0, 600, and 1200 km). The seismicity defines a vertical slab stretching from just below the surface to the seismicity termination near 660 km depth.

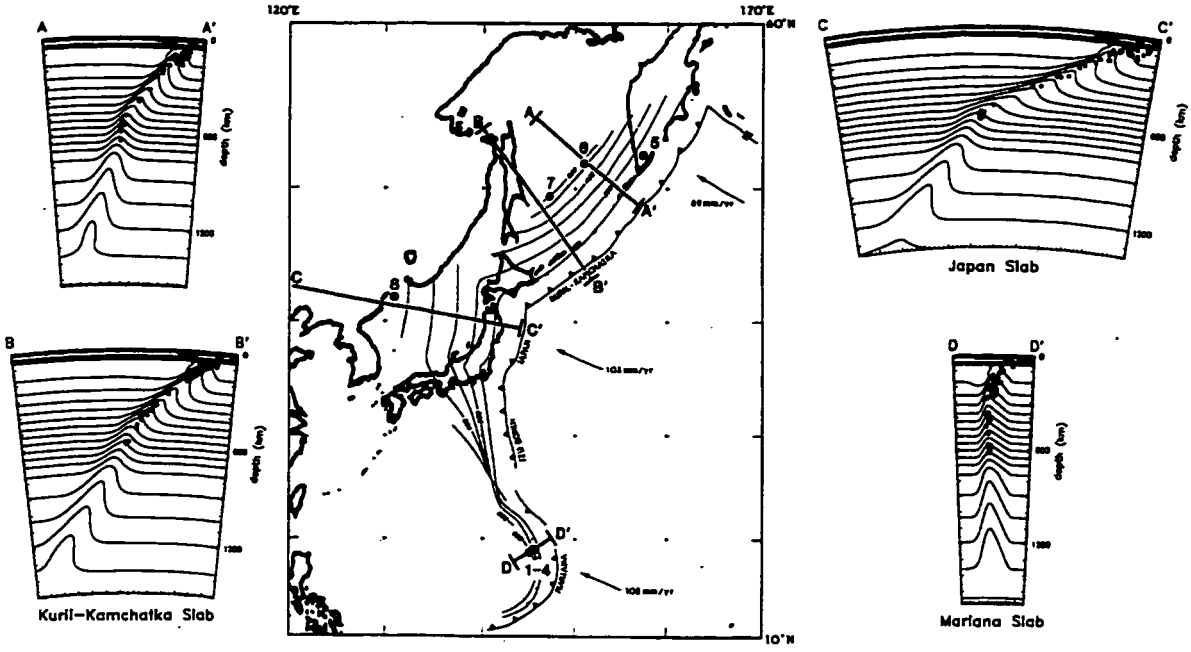

Figure 3.3: Residual sphere analysis [*Creager and Jordan*, 1986]

Izu-Bonin trench

This region is the most complicated trench in the system. At the southern end, near 23°N, tomographic studies [*Widiyantoro*, 1997] image a steeply dipping slab, while to the north, near 32°N, they image a broad, shallowly dipping slab. Residual sphere analysis in the region have been inconclusive [*Creager*, 1984]. Additionally, the membrane strain (the distortion required to fit the Pacific Plate to the seismicly defined subducting slab shape) is extremely high in this region [*Yamaoka and Fukao*, 1986, *Burbach and Frohlich*, 1986, *Creager and Ciao*, 1998].

However, high resolution maps of the 660-km discontinuity demonstrate that the slab bends to a vertical dip at the deepest seismicity [*Castle and Creager*, 1998] (Figure 3.4, chapter 2). Assuming the 660-km discontinuity is the endothermic Ringwoodite (γ-spinel) to perovskite and magnesiowüstite phase change, depression of the discontinuity is due to cold material, such as subducted slab. Thus, mapping the discontinuity topography maps the slab location at depth.

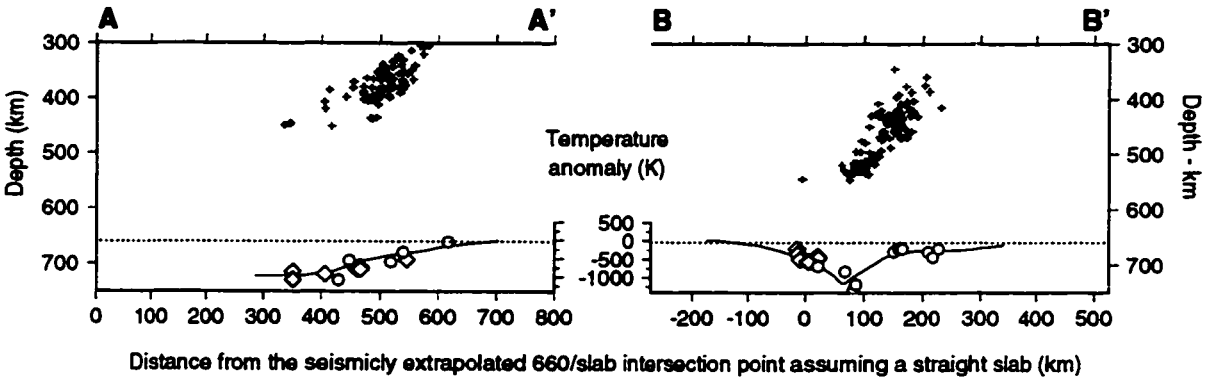

Figure 3.4: Izu-Bonin 660-km discontinuity topography [*Castle and Creager*, 1998]

At 26°N, near the southern end of the trench, the slab descends steeply to the seismicity cutoff. There, it steepens and descends vertically into the lower mantle. Farther to the north at 32°N, historical tectonics complicate the picture. Nevertheless, we see in Figure 2.8 that the slab dips at roughly 45° from the surface to the deepest seismicity, descends vertically from the seismicity cutoff to the 660-km discontinuity, and then extends horizontally to the west upon the discontinuity.

Japan trench

Beneath the Japan trench, two pieces of evidence suggest that the slab dip steepens at the seismicity.

Figure 3.3 shows the results of *Creager and Jordan* [1986] . Using a method called residual sphere analysis, *Creager and Jordan* employed variations (residuals) in the travel times of down-going teleseismic P waves from shallow and deep earthquakes to map out the location and extent of fast material below the earthquakes. The fast velocity anomalies are converted to temperature anomalies and plotted in terms of isotherms (Figure 3.3). Implicit in the interpretation is that fast material represents the thermal signature of a cold subducted slab.

Cross section CC' shows the results of the residual sphere analysis beneath the Japan trench. The slab descends at a shallow angle to the deepest earthquakes where

the dip clearly steepens to over 60°.

Figure 3.5 shows the results of *van der Hilst et al.* [1998] for the region beneath the Japan trench. This tomographic image of the P wave-speeds was created as part of a global inversion using relocated earthquakes [*Engdahl et al.*, 1997] and the arrival times of millions of P, pP, sP, and PKP phases. Red and blue areas show slow and fast velocity anomalies, respectively. We assume that fast areas mark subducted slabs.

Very similar to the residual sphere analysis for this region, Figure 3.5 shows a slab subducting at a shallow angle until it reaches the seismicity cutoff, where the slab subducts at a much steeper angle.

Kuril trench

This region appears similar to the Japan trench. The slab subducts beneath the surface at roughly 45°and again, at the deepest seismicity, the slab steepens dramatically. Both the cross sections AA' and BB' of the residual sphere analysis (Figure 3.3) and the tomographic results of *van der Hilst et al.* [1991] (Figure 3.6) illustrate this steepening well. Also, along AA' (Figure 3.3) the steepening can be seen in the deepest seismicity.

While the high velocities in the transition zone west of the deepest earthquakes in areas such as Izu-Bonin have led to different interpretations (e.g., *Inoue et al,* [1990]), the agreement between the tomography (see also *Kamiya et al.* [1988]), the residual sphere analysis, and discontinuity topography all suggest that the slab indeed goes vertical at the seismicity cutoff.

3.4 Slab membrane strength

Gravity pulls the cold, dense slab downward. It is the membrane strength of the subducting Pacific Plate which prevents it from bending to a vertical dip [*Creager and Boyd*, 1991]. If the membrane strength is removed, the slab falls vertically.

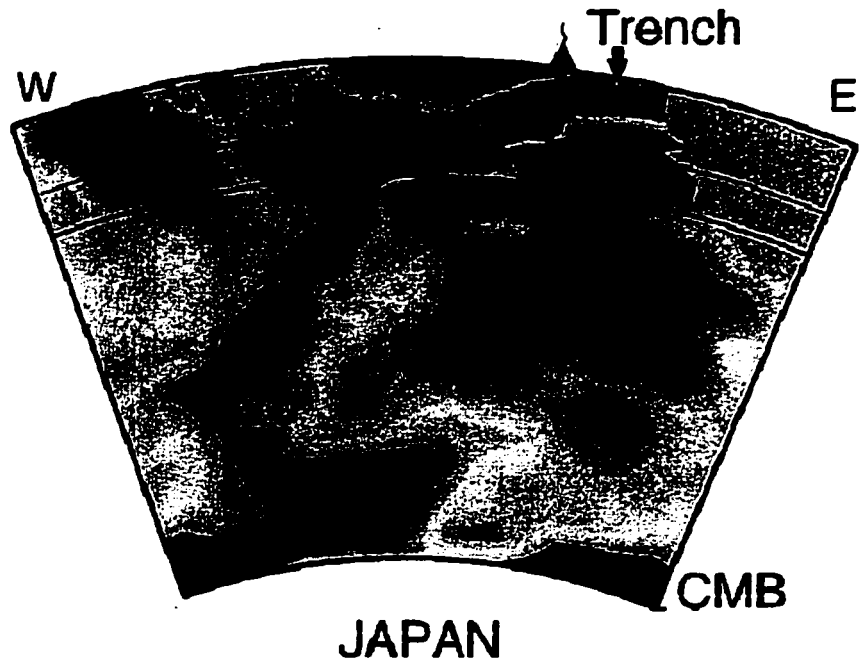

Figure 3.5: Tomography below Japan [*van der Hilst et al.*, 1998]

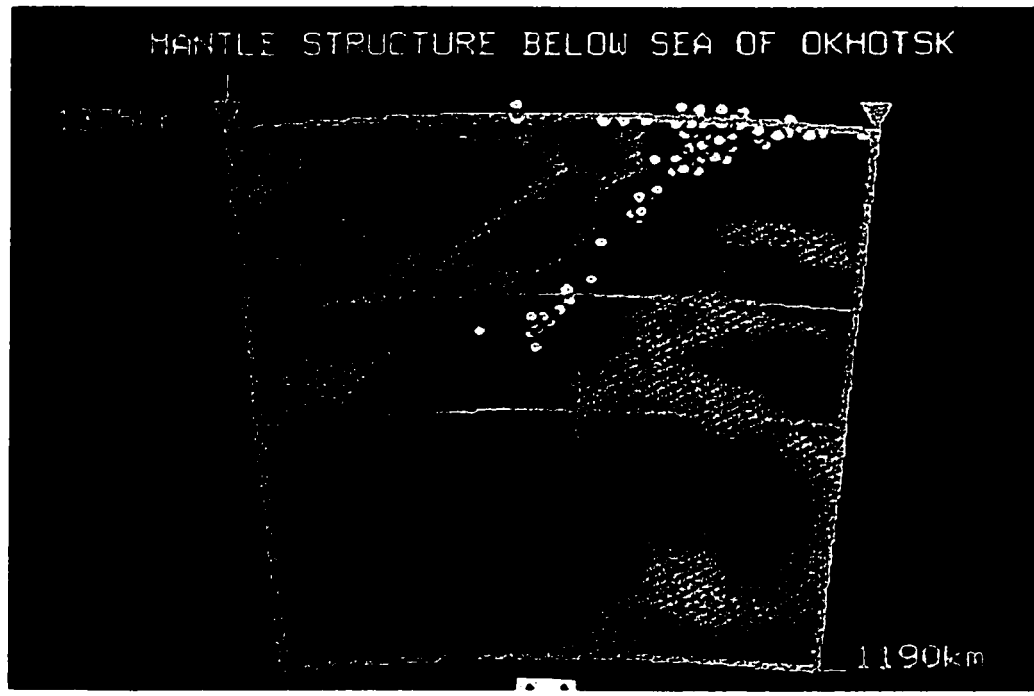

Figure 3.6: Tomography below the Sea of Okhotsk [*van der Hilst et al.*, 1991]

In most 2-D numerical experiments and physical experiments when the trench location is fixed, dense slabs tend to bend near the surface and subduct nearly vertically into the mantle (e.g. *Christensen* [1996] and *Zhong and Gurnis* [1997]). Several attempts have been made to explain why most slabs do not descend vertically into the mantle. Whereas slabs, like a sheet of paper, have little bending strength, the combination of their aspect ratio and high viscosity relative to warm surrounding mantle gives them considerable membrane strength. It appears that the membrane strength of slabs plays a critical role in determining slab geometry (dip) [*Creager and Boyd*, 1991, *Creager et al.*, 1995].

If the slab strength is reduced along a horizontal line, the membrane strength can no longer maintain a shallow dip and the slab will descend more steeply. If the slab strength is reduced along vertical planes, the ability of membrane strength to control dip is determined largely by the ratio of along-arc length of the segment to down dip length. For example, the proposed tear north of the Mariana trench produces a short segment (the Mariana slab) that subducts vertically and a long segment (Izu-Bonin to Kurils) whose geometry may be largely controlled by membrane strength.

Deep earthquakes could remove this membrane strength in either a macro- or microscopic fashion. First, the largest earthquakes may tear the slab [*Silver and Jordan*, 1983]. Second, on a microscopic level, earthquakes may dramatically reduce the constituent grain size, drastically reducing slab strength until the grains have time to grow. In regions of large earthquakes, either one of these, or a combination of the two, could create the zone of weakness necessary to temporarily eliminate the membrane strength.

3.5 The olivine to spinel phase change

We hypothesize that the olivine to spinel phase change is responsible for both observations, the unusual deep earthquakes and the simultaneous change in slab rheology.

In ambient mantle, the olivine to spinel phase occurs near a depth of 410 km and is

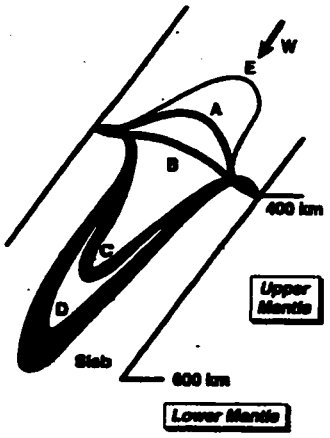

Figure 3.7: The meta-stable olivine tongue [*Däßler et al.*, 1996]. E marks the depth of the equilibrium olivine-spinel phase change, A and B mark the depths of the phase change in slowly subducting slabs (< 6 cm/yr) without and with the effects of latent heat, and C and D mark the depths of the phase change in fast descending slabs (> 8 cm/yr) with and without internal heating.

accompanied by an 8% density increase [*Katsura and Ito*, 1989]. The sudden density increase provides an enhanced negative buoyancy force, driving the slab downward. The phase change from olivine to spinel is exothermic; therefore the depth of the phase change moves to shallower depths in a cold slab at equilibrium. However, recent work has suggested that in old, fast subducting slabs, such as here, the slab subducts too fast to reach equilibrium [*Kirby et al.*, 1991]. Cold temperatures in a slab would delay the transformation of olivine to spinel, creating a "meta-stable wedge" of olivine protruding below 410-km [*Sung and Burns*, 1976]. Depending on the rate of subduction and thermal field in the slab, the wedge could extend down to 660-km, creating an interesting scenario where the meta-stable olivine transforms directly to magnesiowüstite and perovskite. Figure 3.7 [*Däßler et al.*, 1996] illustrates the olivine wedge.

Deep earthquakes occur in the depth range from roughly 350 km - 690 km, the same depth range over which the olivine to spinel phase change occurs. Using analogous structures in Mg_2GeO_4 and ice, two groups [*Green et al.*, 1990, *Kirby et al.*, 1991] independently developed the theory that deep earthquakes are connected to the olivine to spinel transformation, called either the "anti-crack" theory or transformational faulting. In both theories, as the earthquake ruptures in meta-stable olivine, small lenses of spinel are created in the fault gouge.

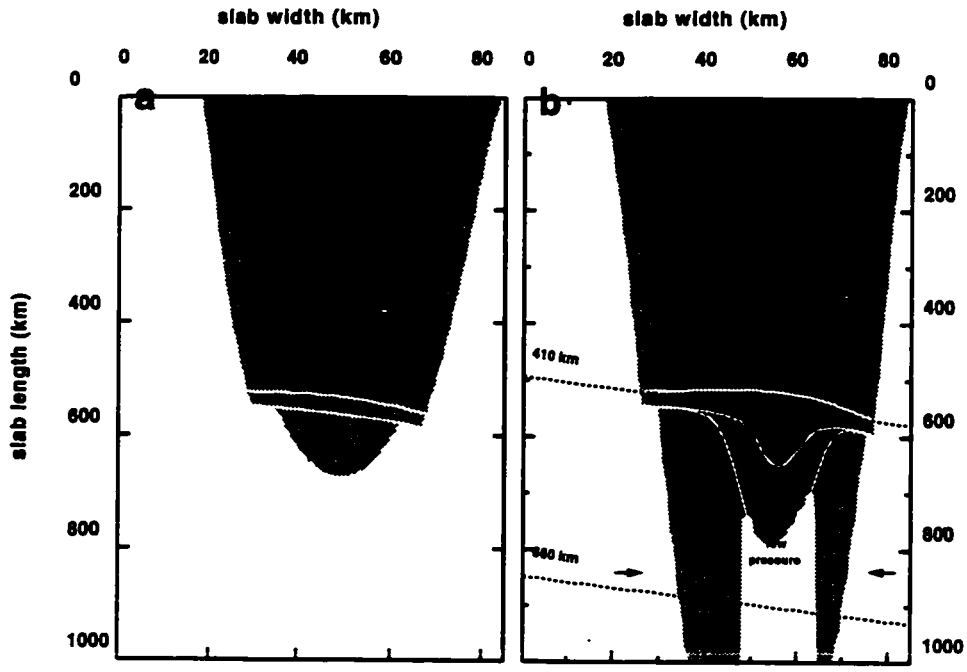

Figure 3.8: The slab rheology [*Riedel and Karato*, 1997]. The left and right plots come from calculations using slowly (4 cm/yr) and quickly (10 cm/yr) subducting slabs. Gray areas represent slab portions with a creep strength greater than 100 MPa. Dark gray areas have a creep strength greater than 200 MPa. The creep model is a Nabarro-Herring creep mechanism. Spinel grain growth was not included in the model and would decrease the size of the weak zone. The axes are slab width versus slab length (not depth) and the dashed lines mark 410 and 660 km depth. Between the arrows on the right plot, "Note the dramatic strength drop below the tip of the meta-stable wedge [*Riedel and Karato*, 1997]."

Däßler et al. [1996] recently showed theoretically that the meta-stable wedge can indeed extend to at least 600 km depth. Second, they found that the heat release in the meta-stable olivine to spinel phase change is three times greater than in the equilibrium phase change and thus results in localized heating in the slab of up to 150°C. They advanced the idea that the deep earthquakes occur as a runaway phase transformation, with the latent heat release providing a catalytic effect.

Finally, *Riedel and Karato* [1997] calculated the effect of the olivine to spinel phase change on the slab rheology. In warm slabs, the size of the spinel grains nucleated at olivine grain boundaries are not significantly smaller than olivine grains. On the other hand, in cold slabs, the grain size reduction can be four orders of magnitude.

This temperature dependence creates an interesting scenario immediately following the olivine-spinel phase change: cold slabs are weaker than warm slabs. Figure 3.8 [*Riedel and Karato*, 1997] shows their modeling results and dramatically displays the weak zone within a quickly subducting slab.

3.6 Deep earthquakes and slab rheology

From theoretical modeling, we see:

1. The depth range of the olivine to spinel phase change matches the depth range of the deep earthquakes.

2. There exist large compressive stress at depth within the slab.

3. Runaway meta-stable olivine to spinel phase transformations likely cause the rupture of deep earthquakes.

4. The phase transformation creates a weak zone within the slab.

We also have following observations:

1. The olivine to spinel phase change is accompanied by an 8% density increase.

2. The deepest earthquakes in the Izu-Bonin trench are responding to regional tectonic stresses, unlike shallower deep earthquakes, and mark a weak point in the slab.

3. The deepest earthquakes are larger than shallower deep earthquakes.

4. At the deepest earthquakes, the slab geometry changes. Below the earthquakes, the slab falls vertically downward, again suggesting a weakness in the slab at the deepest earthquakes.

Synthesizing these results, the subducting Pacific Plate descends from the surface. As the olivine enters the spinel stability field, compressive stress within the slab increase, deep earthquakes occur and the olivine begins to transform to spinel. A meta-stable olivine wedge develops, providing a positive (upward) buoyancy force which contributes to the shallow slab dip above the seismicity termination. Within the cold slab, the olivine to spinel phase transformation nucleates extremely small grains and the earthquakes tear the slab. The largest earthquakes, where the seismicity ceases, may mark the location where all of the olivine in the meta-stable wedge has been consumed. At that point, the slab has been thoroughly weakened. The phase change has increased the density of the cold slab, providing an additional negative (downward) buoyancy force. The zone of weakness at the seismicity cutoff effectively isolates the deep slab, relieving it of its membrane strength, and allowing it to fall vertically downward.

The Ocean Hemisphere Project (OHP), the Japanese initiative to place seismometers throughout the western Pacific oceanic region, will provide data crucial to further test this hypothesis. Receiver studies using data from stations near trenches should create better maps of the 660-km discontinuity topography and thus better reveal the slab location at depth. Data from these stations will also improve regional tomographic imaging by both improving earthquake hypocenter accuracy and increasing the number of raypaths near subducting slabs.

Chapter 4

SHEAR WAVE VELOCITY JUMP ACROSS 660-KM DISCONTINUITY: IMPLICATIONS FOR MANTLE CHEMISTRY

4.1 Abstract

Stacked vertical component short-period teleseismic data from earthquakes in the Izu-Bonin subduction zone recorded by networks in the Western United States reveal phases associated with conversions from mantle discontinuities. The dominant phase in the stacked P coda is the result of near source S-to-P conversions from a subhorizontal discontinuity at a depth ranging from 650 km to 745 km. We used 88 timings of this phase, called $S_{660}P$, to determine the topography of the 660-km discontinuity. Employing the 17 best recorded $S_{660}P$ phases (for which neither the $S_{660}P$ nor P radiation were nodal and for which there were over 70 seismograms per stack), we modeled the $S_{660}P$ amplitude using realistic synthetic seismograms which included corrections for 3-D discontinuity topography. The 3-D topography altered the $S_{660}P$ raypath and the incident angle at the discontinuity; we applied corrections to account for the corresponding changes in both the source radiation pattern and in the S-to-P conversion coefficient. The S wave velocity contrast across the 660-km discontinuity beneath the Izu-Bonin subduction zone is 0.40 ± 0.05 km/sec. This value is 8% larger than the PREM value and, unlike reflected SH waves, is independent of the estimated density contrast at 660 km. Recent mineral physics data suggest that the velocity jump at 660 km is strongly dependent on the aluminum content. Incorporating values extrapolated from these data, our velocity jump suggests that the lower portion of the mantle transition zone is consistent with a pyrolitic mantle containing 4% cation aluminum.

4.2 Introduction

Near 660 km depth, Ringwoodite (γ-spinel) transforms to seismicly faster perovskite and magnesiowüstite [*Liu*, 1979]. Seismic observations of the velocity and density jumps across this discontinuity serve as reference points for thermal, dynamical, and compositional models of the mantle. Several studies have estimated the impedance contrast (change in the product of density and shear-wave velocity) using low frequency SH waves. *Grand and Helmberger* [1984a,b] modeled waveforms of wide-angle reflections, *Revenaugh and Jordan* [1991a] analyzed near vertical reflections of ScS phases, and *Shearer* [1991] stacked underside reflections. These long-period studies measured changes in impedance averaged over 20 km. Previous converted phase studies (e.g., *Paulssen* [1985] and *Richards and Wicks* [1990]) were unable to measure the size of the velocity contrast, likely due to both noise and effects from the 3-D topography of the discontinuity [*van der Lee et al.*, 1994].

We use the teleseismic $S_{660}P$ phase to measure the size of the shear wave velocity jump across the 660-km discontinuity. This method has several attractions. First, the amplitude of this phase, relative to the P wave, depends almost entirely on the magnitude of the shear wave velocity contrast across the discontinuity rather than on the impedance contrast (Figure 4.1). Thus, no assumptions or extrapolations about the density are necessary to determine the shear wave velocity jump. Second, using comparatively high frequencies ($^1/_2$ Hz), we were able to create the high resolution topography map of the discontinuity necessary to model the effects of the 3-D surface [*Castle and Creager*, 1998]. Finally, by using near source S-to-P converted phases, we were able to investigate the size of shear wave jump in a region - a subduction zone - that had not been previously explored. Subduction zones, where cold downwellings encounter mantle discontinuities and disturb the ambient state, play a key role to the understanding the nature of discontinuity effects on global dynamics.

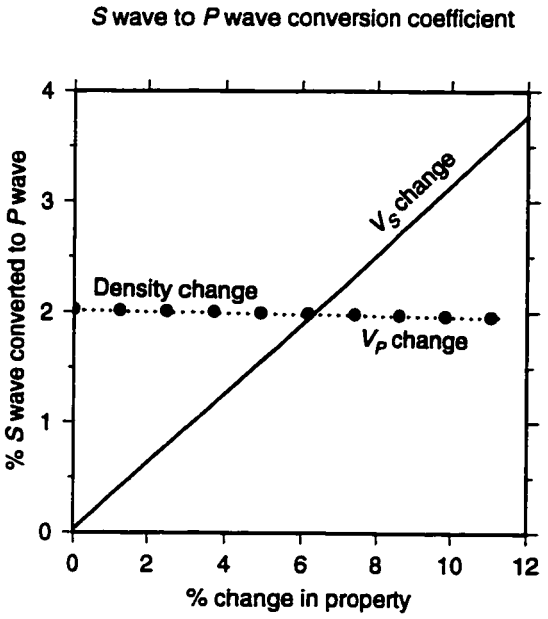

Figure 4.1: Percent of the S -wave amplitude converted to a P -wave at the 660-km discontinuity coming from an earthquake at 425 km depth recorded at 79°(slowness = 5.3 s/°). When one property's jump across the discontinuity is varied, the others remain at their *iasp91* values.

4.3 *Data and Method*

For each of the seventeen Izu-Bonin subduction zone earthquakes (Table 4.1), we analyzed the teleseismic records from short-period, vertical component seismometers located in the Western United States in one of three major seismic networks: the Pacific Northwest Seismic Network (PNSN), downloaded from the IRIS Data Management Center; the Northern California Seismic Network (NCSN); and the Southern California Seismic Network (SCSN). We processed the data to look for the $S_{660}P$ phase, which leaves an earthquake as a down-going S (shear) wave, converts to a P (compressional) wave at the 660-km discontinuity beneath the earthquake, and continues to the receivers as a P wave, following a path similar to the direct P wave.

We chose data from Izu-Bonin subduction zone earthquakes based on the following criteria: (1) > 70 quiet seismograms, and (2) neither the $S_{660}P$ nor the P wave radiation pattern was near nodal. We did not remove the data for which $S_{660}P$ was near the noise level (e.g. # 1 and 17, Figure 4.2). Therefore, our estimate of the shear velocity jump is not biased by removing data which could be associated with

Table 4.1: 17 Izu-Bonin earthquakes

No	Date	Dep	Stations			Per	$S_{660}P$	P rad	S rad	$S_{660}P$ amp (% P)		
		(km)	Net	#	Δ	(sec)	depth	(nodal = 0)		Data	Flat	3-D
1	84-03-06	456	NCSN	91	80	2-5	666	0.83	0.80	10	14	10
2	84-04-24	400	SCSN	99	83	2-5	675	0.38	0.76	19	27	30
3	85-04-03	472	NCSN	173	80	2-5	676	0.47	0.88	31	24	26
4	85-04-03	472	PNSN	79	76	2-5	671	0.51	0.88	38	24	20
5	85-09-10	517	SCSN	103	84	2-5	674	0.34	0.73	13	24	20
6	86-02-03	529	SCSN	74	84	2-5	671	0.68	0.75	11	13	8
7	91-05-03	475	NCSN	103	79	2-5	686	0.55	0.94	28	25	21
8	92-01-20	521	NCSN	131	80	2-5	671	0.30	0.44	24	23	19
9	92-01-20	521	PNSN	197	76	2-5	670	0.36	0.48	28	21	19
10	92-05-30	12	PNSN	104	73	2-5	650	0.22	-0.66	49	48	64
11	92-08-07	359	PNSN	102	73	2-5	665	-0.25	-0.47	25	16	20
12	92-08-29	306	NCSN	151	78	2-5	662	0.61	0.74	13	17	20
13	92-08-29	306	PNSN	111	73	2-5	660	0.58	0.66	12	18	20
14	92-10-30	413	NCSN	116	79	2-5	655	0.34	0.89	22	31	23
15	93-07-05	406	PNSN	92	75	1-4	655	-0.34	-0.31	21	15	11
16	93-07-20	461	PNSN	77	76	2-5	684	-0.32	0.66	20	15	17
17	93-10-11	357	PNSN	98	74	1-4	660	0.66	0.64	9	13	13

smaller velocity jumps.

For each earthquake network pair, noisy traces were removed, seismograms were demeaned, 2 - 5 second bandpass filtered, normalized, aligned on the P arrival, and linearly slant stacked. By using a slant stack algorithm, also known as a $\tau - p$ stack, which shifts each seismogram (in time) by a constant multiplied by its epicentral distance, we used the network as an antenna and effectively focused the seismometers on both the P and $S_{660}P$ phases.

We modeled the amplitude of the $S_{660}P$ phase relative to the P wave with synthetic seismograms. We created WKBJ synthetics [*Chapman*, 1978] for the two phases using the *iasp91* velocity model [*Kennett and Engdahl*, 1991] with discontinuity depths modified to match the timing observed in the data, the PREM density model [*Dziewonski and Anderson*, 1981], and the USGS double-couple focal mechanisms [*Sipkin*, 1986]. For each station in each earthquake/network pair, we calculated a synthetic, convolved in the observed source time function (which included the instru-

ment response and bandpass filter), and applied identical processing as was applied to the data.

However, the $S_{660}P$ amplitude also depends on the topography of the discontinuity. *Castle and Creager* [1998] (chapter 2) mapped the regional discontinuity topography by applying a migration algorithm to the relative timing of the $S_{660}P$ phase. They incorporated data from several studies using worldwide short-period and broad-band seismic records [*Vidale and Benz*, 1992, *Wicks and Richards*, 1993a]. Using their discontinuity topography map, we found that our $S_{660}P$ conversion points lay at areas on the discontinuity surface with limited but finite topography. To account for the topography, we applied two corrections to the amplitude of the synthetic $S_{660}P$ phase. (1) The S-to-P conversion locations are at different locations than in the flat discontinuity case. The ray thus leaves the earthquake traveling in a different direction, at a different spot on the radiation pattern, and has a different initial amplitude. This correction factor was as large as 14%. (2) The S wave is no longer incident upon a horizontal surface. We recomputed the S-to-P conversion coefficient using the new incident angle, producing a correction coefficient up to 35% [*Aki and Richards*, 1980]. Two 3-D effects we did not model were changes in the geometric spreading of each ray packet and the effects of the subducting slab on the ray path. Geometric spreading due to topography on the discontinuity may significantly alter amplitudes [*van der Lee et al.*, 1994]. The correction depends critically on the second derivative (curvature) of the surface, which is not robustly determined in the topography maps. The effects of a slab on ray paths can also be significant. However, in this case, since the rays travel to the northeast and immediately leave the plane of the slab, the slab has a negligible effect [*Creager*, 1984]. Once the rays leave the source region and enter the lower mantle, the $S_{660}P$ and P waves follow very similar paths, so 3-D velocities in the lower mantle and under stations should have also negligible effect on $S_{660}P$ / P amplitude ratios.

To determine the magnitude of the S wave velocity contrast at the discontinuity,

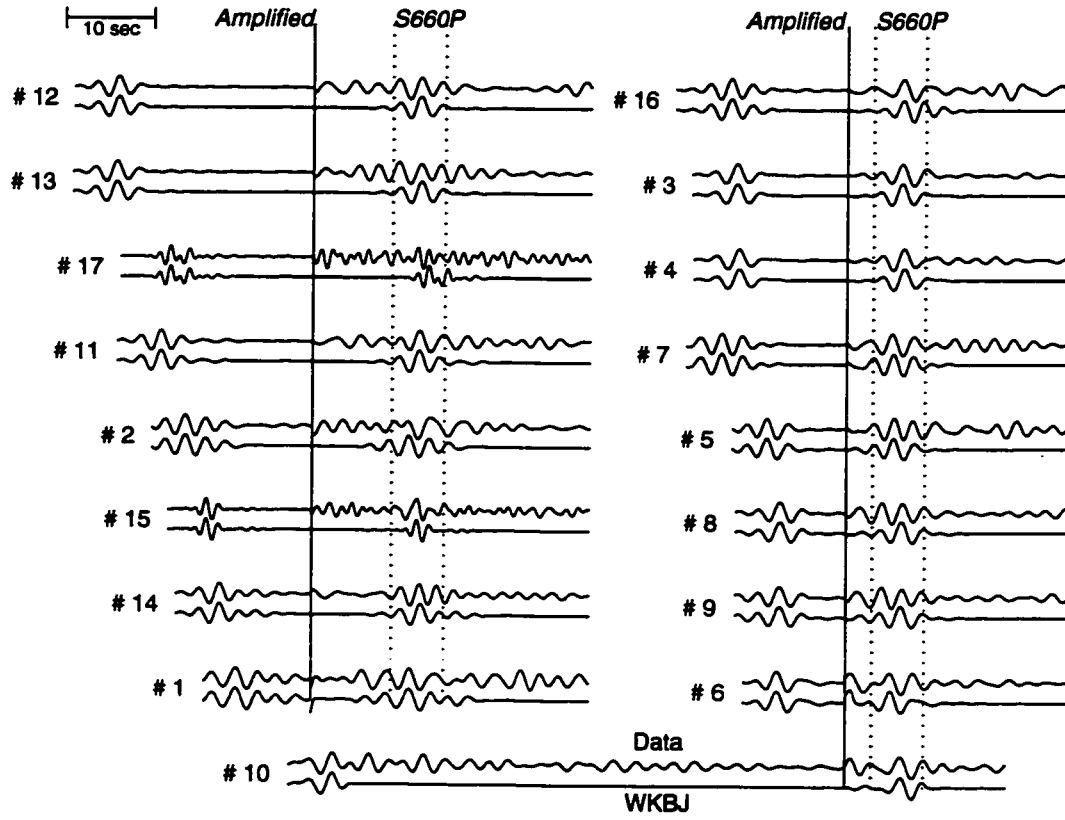

Figure 4.2: The observed waveforms (top) and synthetic waveforms (bottom) for the seventeen events. The amplitudes left of the solid line have been normalized while right of the solid line they have been normalized by the reciprocal of the percent listed in Table 4.1 under "Data" and "3-D". The peak-to-peak amplitudes are measured in the time window between the dashed lines.

we compared the amplitude of the $S_{660}P$ phase in the stacked synthetics with the amplitude in the stacked data. Figure 4.2 shows stacks of data (top) and synthetics (underneath) which include the correction factors mentioned above. The data are ordered by earthquake depth, except for number 10 at the bottom, and are normalized after the solid line by the reciprocal of the percent listed in Table 4.1 under "Data" and "3-D". Figures 4.3A and B show comparisons of the relative amplitudes (maximum peak-to-peak $S_{660}P$ amplitude over maximum peak-to-peak P amplitude) of the data versus the relative amplitudes of the synthetics for both the uncorrected and corrected cases, respectively.

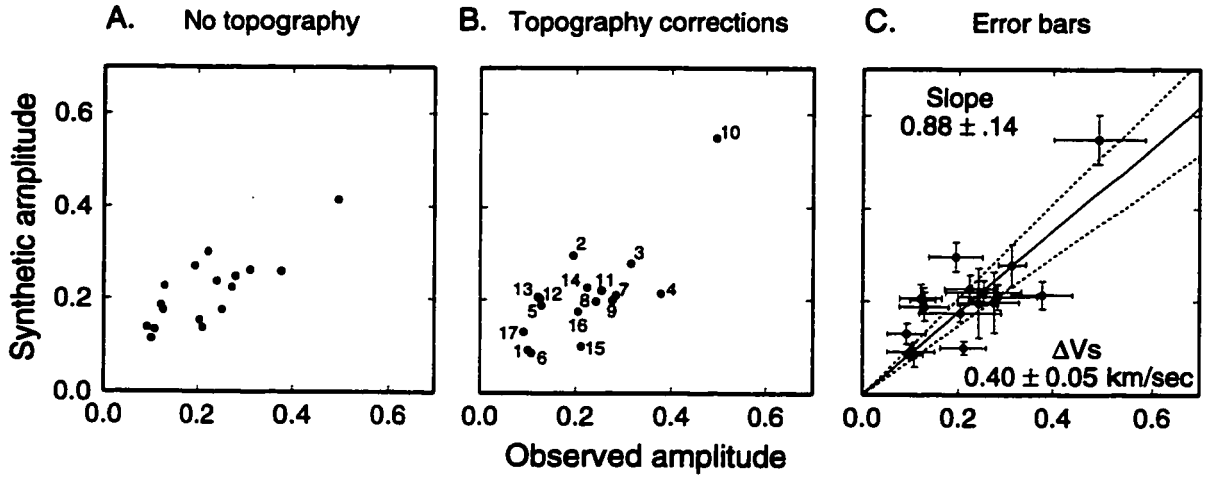

Figure 4.3: The observed ($S_{660}P/P$) amplitudes (peak-to-peak) versus the synthetic amplitudes. A) For a discontinuity without topography. B) Incorporating topography corrections for the radiation pattern and conversion coefficient. C) Graph (B) with error bars.

The correlations in both the waveforms and the amplitudes of the $S_{660}P$ phase between the corrected synthetics and the data are remarkable, especially considering the high frequencies ($^1/_2$ Hz) and the small amplitude of the $S_{660}P$ phase. On each individual seismogram, near-receiver reverberations typically dominate the P-wave coda and have higher amplitudes than the $S_{660}P$ phase. However, the local reverberations are incoherent over the large area covered by these networks; therefore by stacking an average of more than 100 seismograms per event increases the signal ($S_{660}P$) to noise (local reverberations) ratio by 10 (roughly the square root of the number of stations).

We estimated errors in the data amplitude measurements (the x-axis) by taking the maximum amplitude in a ten second window after the $S_{660}P$ arrival. We calculated uncertainties in the synthetic amplitudes by finding the maximum variation of the two 3-D correction factors (the radiation pattern and the S-to-P conversion coefficient) on an empirically chosen 10 km radius disc surrounding the S-to-P conversion point. Figure 4.3C shows these error bars.

4.4 *Results*

Incorporating our error estimates, the best-fitting line in a chi-squared sense through zero and the points has a slope of 0.88 with one standard deviation of $\pm.14$ relative to the *iasp91* velocity model. This corresponds to a shear wave velocity contrast at the 660-km discontinuity of 0.40 $\pm$ 0.05 km/sec for $^1/_2$ Hz waves.

We were concerned that point #10 (upper right corner, Figure 4.3) outweighed the other points. Additionally, this earthquake was the only shallow earthquake used and the synthetics did not include attenuation. (Note, however, that the rays did not travel through the spreading center west of the Izu-Bonin trench but rather traveled through the older, colder material to the north-east.) However, by removing this point, we obtained essentially an identical result: $\Delta V_s = 0.41 \pm 0.06$ km/sec. Also, using a bootstrap calculation, we obtained $\Delta V_s = 0.40$ km/sec with a standard deviation of 0.04 km/sec. One issue was that for some small amplitude events where $S_{660}P$ barely stood out, such as numbers 1 and 17, we may have measured the amplitude of the noise and not $S_{660}P$ (Figure 4.3). Technically, the best treatment of each of these two points would have been to assume that the observed amplitude of $S_{660}P$ was somewhere equally distributed between zero and the value listed. On the other hand, by simply eliminating these two points from our estimation, we again found $\Delta V_s = 0.40 \pm 0.06$ km/sec. Finally, as mentioned above, the synthetic seismograms did not include attentuation. The unmodeled effects of possibly greater S wave attentuation would bias our estimate to a smaller value; the actual veloctity jump across the discontinuity would be larger and our value would thus serve as a lower bound.

Another concern was that the relatively short wavelengths of 10 km ($^1/_2$ Hz) measured only part of the total velocity jump. As a rule of thumb, the thickness of a "discontinuity" is one quarter the shortest wavelength at which it can be observed [*Richards*, 1972], thus we were observing structures that were less than 3 to 7 km thick and therefore any broader structures would be unmodeled in our results.

Table 4.2: ΔVs at 660-km discontinuity

Property	*iasp91* [a]	*PREM*[b]	TNA/SNA[c]	Pau87[d]	RJ91[e,f]	this study
ΔVs (km/s)	0.35	0.37	0.41	0.62	0.49	0.40
%	6.2	6.7	7.5	11.3	8.5	7.1
Depth (km)	660	670	660	650	660	mean = 667

[a] *Kennett and Engdahl* [1991] - global model
[b] *Dziewonski and Anderson* [1981] - global model
[c] *Grand and Helmberger* [1984a,b] - North American models
[d] *Paulssen* [1987] - European model
[e] *Revenaugh and Jordan* [1991] - Pacific Ocean model
[f] inferred from (Δ impedance) = 0.072 $\pm$ 0.010 using a density scaling $\partial \ln v_s / \partial \ln \rho = 1$

Previous seismic studies found discontinuity thicknesses of less than 4 km [*Richards*, 1972, *Benz and Vidale*, 1993, *Yamazaki and Hirhara*, 1994]. Further, the P and $S_{660}P$ phases are coherent to at least $^1/_2$ Hz (chapter 7), corresponding to 11.2 km wavelengths, implying that the main phase transition is completed over less than 3 km. The mineral physics results of *Ito and Takahashi* [1989] also show that the Ringwoodite to perovskite and magnesiowüstite transformation takes place over less than 4 km depth range. Recent modeling of phase transitions suggests that while they asymptotically come to completion, they begin exponentially [*Stixrude*, 1997]. It follows that the velocity jump reported here was essentially the velocity jump for the Ringwoodite to perovskite and magnesiowüstite phase change. However, since other components (i.e. garnets and stishovites) have broader (more gradual) phase changes at similar depths; the long-period estimates of the jumps across the 660-km discontinuity may also include contributions from these secondary phase changes.

4.5 *Discussion*

Table 4.2 shows a comparison of 660-km results. While almost every modern velocity profile includes a sharp jump near 660 km depth, the sparseness of studies revealing the shear wave contrast at the discontinuity is notable. Our result is the first value from a subduction zone and is surprisingly similar to results from other tectonic

regions, such as that of *Grand and Helmberger* [1984a,b] from western North America. Our value is much smaller than that of *Paulssen* [1987] and somewhat smaller than that of *Revenaugh and Jordan* [1991a]. As an interesting side note, *Revenaugh and Jordan* found a negative correlation between the discontinuity depth and the size of the velocity jump. The results presented here agree with this hypothesized negative correlation: *Paulssen* found a large, shallow discontinuity under Europe (650 km, $\Delta Vs = 0.62$ km/sec), *Revenaugh and Jordan* found it deeper and smaller under the Pacific (660 km, 0.49 km/sec), and we found it even deeper and shallower in the subduction zone (667 km, 0.40 km/sec).

One persistent question has been how well does the pyrolite model of mantle composition [*Ringwood*, 1975] represent the earth. In the pyrolite model, the olivine to spinel phase change causes the 410-km discontinuity. Using mineral physics extrapolations to estimate the velocity jumps in the pyrolite model, *Bass and Anderson* [1984] and *Duffy and Anderson* [1989] asserted that the seismicly observed velocity jump at the 410-km discontinuity was to large to be consistent with the pyrolite composition. However, later work (e.g., *Rigden et al.* [1991] and *Bina* [1993]) found that the pyrolite composition indeed satisfied the seismic observations.

We anticipate a similar argument will encompass the 660-km discontinuity as mineral physics data accumulate. At 1600°K and 23 GPa, Ringwoodite, which composes 60% of the lower region of a pyrolitic mantle transition zone, transforms to perovskite and magnesiowüstite [*Ito and Takahashi*, 1989]. Extrapolating mineral physics data to these conditions, the phase change in a pyrolitic mantle increases the shear wave velocity by 0.32 to 0.48 km/sec, depending on whether aluminum composes 3% or 5% of the cations, respectfully [*Weidner and Wang*, 1998]. Compared to 0.40 km/sec, as found in this study, these extrapolations suggest that the lower transition zone is consistent with a pyrolitic mantle with roughly 4% cation aluminum.

Chapter 5

SEISMIC EVIDENCE AGAINST A MANTLE CHEMICAL DISCONTINUITY NEAR 660 KM DEPTH BENEATH IZU-BONIN

5.1 Abstract

We analyze *P*-wave codas from 12 deep Izu-Bonin earthquakes recorded by hundreds of Western United States seismograph stations for evidence of small-amplitude phases caused by near-source mantle discontinuities. For nearly every event, the dominant phase in the coda is the result of an *S*-to-*P* conversion from a nearly horizontal discontinuity ranging in depth from 650 to 690 km. This is interpreted as a thermally depressed spinel to perovskite and magnesiowüstite phase transition. If the 660-km seismic discontinuity is also associated with a change in chemistry, it would be dynamically depressed by a subducting slab. We consistently see that there is no nearly horizontal discontinuity between 700 and 1000 km with shear wave velocity contrast exceeding 1%; this observation places constraints on the properties of a postulated chemical discontinuity separating the upper and lower mantles.

5.2 Introduction

Seismic images of the boundary layers separating the upper mantle from the lower mantle provide a key to our understanding of large-scale mantle dynamics. That the global, seismic discontinuity at 660 km depth is primarily the result of a phase change from γ-spinel to perovskite and magnesiowüstite is widely accepted (eg. *Liu*

[1979]). This phase change is apparently is endothermic with a negative Clapeyron slope of -2 to -2.8 MPa/°K [*Ito and Takahashi*, 1989, *Bina and Helffrich*, 1994]. However, it has been suggested that this discontinuity also marks a chemical change (eg. *Anderson* [1977]). An enrichment in Si, Fe, or both, making the lower mantle more dense than the upper mantle, would add an additional stabilizing force further inhibiting convective mixing across this depth [*Ringwood and Irifune*, 1988, *Christensen and Yuen*, 1984].

In the vicinity of cold, lithospheric slabs, we expect the phase change to be depressed by about 50 km. Indeed, detailed investigations of the depth of this discontinuity close to where the Tonga [*Richards and Wicks*, 1990, *Niu and Kawakatsu*, 1995] and Izu-Bonin [*Vidale and Benz*, 1992, *Wicks and Richards*, 1993a] slabs reach depths of 660 km indicate depressions up to 60 km. However, should a chemical discontinuity globally coincide with the phase change at 660 km, the chemical discontinuity should: [1] be locally dynamically depressed 100-300 km in subduction zones [*Christensen and Yuen*, 1984, *Kincaid and Olson*, 1987], [2] be sharp [*Lees et al.*, 1983], and [3] have a velocity contrast ranging from 4% to 7% [*Lees et al.*, 1983] to -3.5% to 2% [*Jeanloz*, 1991]. We present evidence in support of the phase boundary being depressed up to 50 km below the Izu-Bonin subduction zone, while, at the 1% detection level in shear-wave velocity contrast, there is no nearly horizontal discontinuity between 700 and 1000 km depth which might be associated with a chemical boundary.

5.3 Method and Data

We analyze P-wave codas from 12 deep earthquakes in the Izu-Bonin subduction zone recorded by hundreds of short-period, vertical seismometers in the Western United States (Figure 5.1, Table 5.1). Data were recorded by the Southern California Earthquake Center (SCEC), Northern California Earthquake Data Center (NCEDC) and the Pacific Northwest Seismic Network (PNSN) and originally collected and prepro-

Table 5.1: Twelve Izu-Bonin earthquakes

No	Depth (km)	# Sta.	Dist. (°)	$S_{660}P$ to depth	$S_{660}P$
1	306	151	77	8	650
2	386	51	83	5	655
3	400	110	83	13	690
4	413	116	79	17	655
5	456	90	79	6	?
6	472	173	80	12	690
7	475	103	80	11	685
8	504	60	84	6	?
9	517	101	84	13	685
10	521	131	79	8	660
11	523	39	84	4	?
12	547	121	82	3	655

cessed by J. Vidale. We process these data to look for energy that leaves an earthquake as down-going S (shear) waves, converts to P (compressional) waves at a discontinuity at 'X' km depth beneath the source, and continues to the receivers as P waves, following paths similar to the direct P wave. The S_XP wave arrives after the P wave as it traverses the region between the earthquake and the discontinuity as a slower S wave. With knowledge of the hypocentral depth [*van der Hilst and Engdahl*, 1992] and seismic velocities, the relative S_XP to P delay time is a measure of the depth of the 'X' discontinuity. While we are not able to see diffuse seismic gradients with short-period data, we are able to see sharp discontinuities, such as a postulated chemical discontinuity [*Lees et al.*, 1983].

For each earthquake, noisy traces are removed, seismograms are demeaned, 0.5-Hz low-pass filtered, normalized, aligned on the P arrival, and slant stacked using a non-linear N^{th} root algorithm [*Muirhead and Datt*, 1976] with N=3. This algorithm robustly enhances coherent signals, predominately those caused by structures common to all wavepaths, such as near source structures, while reducing incoherent signals, such as high-amplitude, but uncorrelated, energy caused by reverberations in the differing local structure under each receiver. A slant stack is an N^{th} root stack (mean

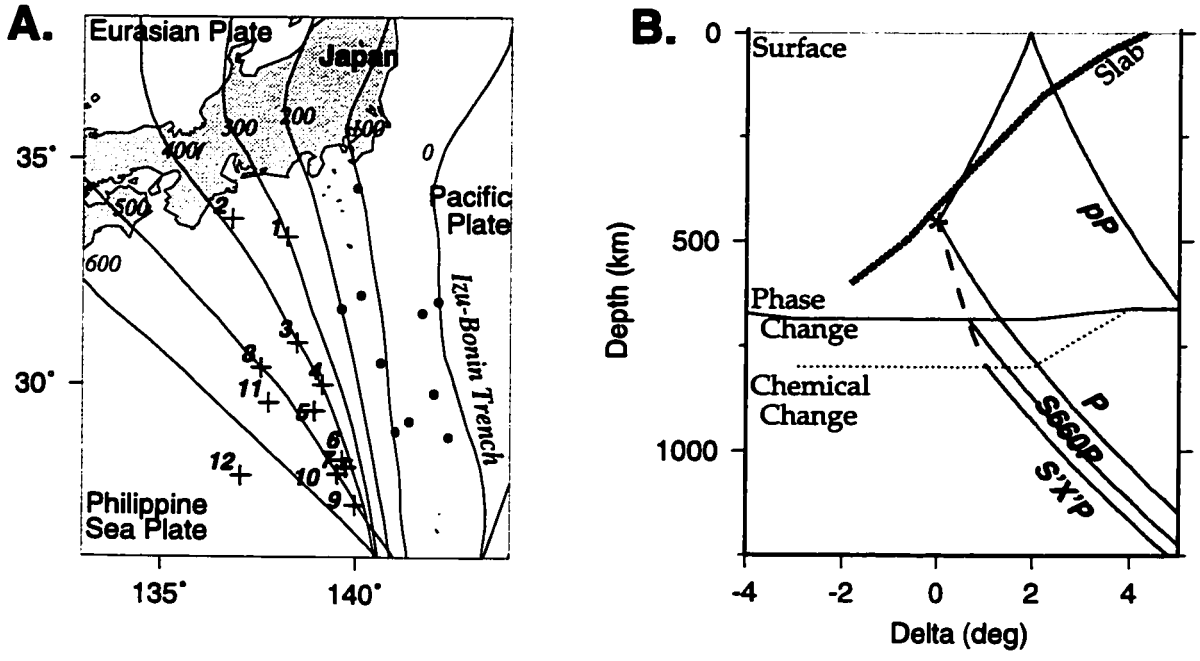

Figure 5.1: (a) Map view of Izu-Bonin source region, showing the earthquakes (+), the observed $S_X P$ conversion points (•) at various depths (see text), and earthquake depth isolines (note that the 500km and 600km contours are extrapolations); and (b) cartoon vertical cross section showing the pP, P, $S_{660}P$, and $S_X P$ ray paths; approximate slab surface; a phase change at 680 km; and a hypothetical chemical change at 800 km depth.

if N=1) of the seismograms after shifting each seismogram by a constant multiplied times its epicentral distance. The constant is the horizontal slowness (reciprocal of the horizontal phase velocity) minus the horizontal slowness of the direct P arrival. Rays interacting with discontinuities above (below) the source have positive (negative) slownesses relative to P (Figure 5.1a). Thus energy plotting in the top half of the slant stacks of Figure 5.2 corresponds to energy leaving the source going up (eg. pP), while energy from S-to-P conversions from discontinuities below the source plots in the bottom half. The slant stack effectively allows us to focus the "antenna" of seismographs on energy coming to the stations from different angles (slownesses). Our wide aperture networks, of order 500 km, allow good slowness resolution. For example, the phases for event 4 arriving 65s and 70s after P (Figure 5.2) are enough separated in slowness such that the 65s arrival (with negative slowness) is probably

$S(\text{down})_{1200}P$ while the 70s arrival (with positive slowness) is probably $p(\text{up})_{95}P$.

5.4 Results

5.4.1 The "660-km phase transition"

A spectacular result of the stacked data is that nearly all of the events exhibit distinct arrivals of energy superposed on low-level background noise (Figures 5.2 and 5.3). For 9 of the 12 events, the largest arrival between P and pP occurs at the time and slowness predicted for S-to-P conversions off a discontinuity between about 650 and 690 km depth (Figure 5.3). The three events with no strong observed $S_{660}P$ arrivals are each among the five events whose focal mechanisms [*Sipkin*, 1986] predict weak $S_{660}P$ / P amplitude ratios (Table 5.1). In all cases, when we expect to see a strong $S_{660}P$ converted phase it is very clear (Figure 5.3).

5.4.2 Search for a chemical discontinuity

If other horizontal, or nearly horizontal, discontinuities exist in the mantle below 700 km depth they should appear in Figure 5.3 as distinct arrivals. Arrival time curves for conversions at 660 and 1000 km are shown for reference. The very quiet stacked seismograms, with distinct pulses of energy are strong evidence that the lower mantle below these earthquakes is generally very smooth. To address the question of whether a second, possibly chemical, discontinuity exists we first discuss the events that have the most favorable radiation patterns for S-to-P conversions (events 1,3,4,6,7,9, and 10; Table 5.1). Event 1 is consistent with a discontinuity at 900 km depth while there are no discontinuities below 660 from event 3 to a depth of 1000 km where the data unfortunately end. Events 4, 6, 9, and 10 argue strongly for no discontinuity between 700 and 1000 km (Figures 5.2 and 5.3). However, there are arrivals consistent in time and slowness with horizontal discontinuities at depths of 1150 and 1300 (event 4), 1200 (event 6), 1000 (event 9) and 1000 and 1100 km (event 10). Figure 5.1b

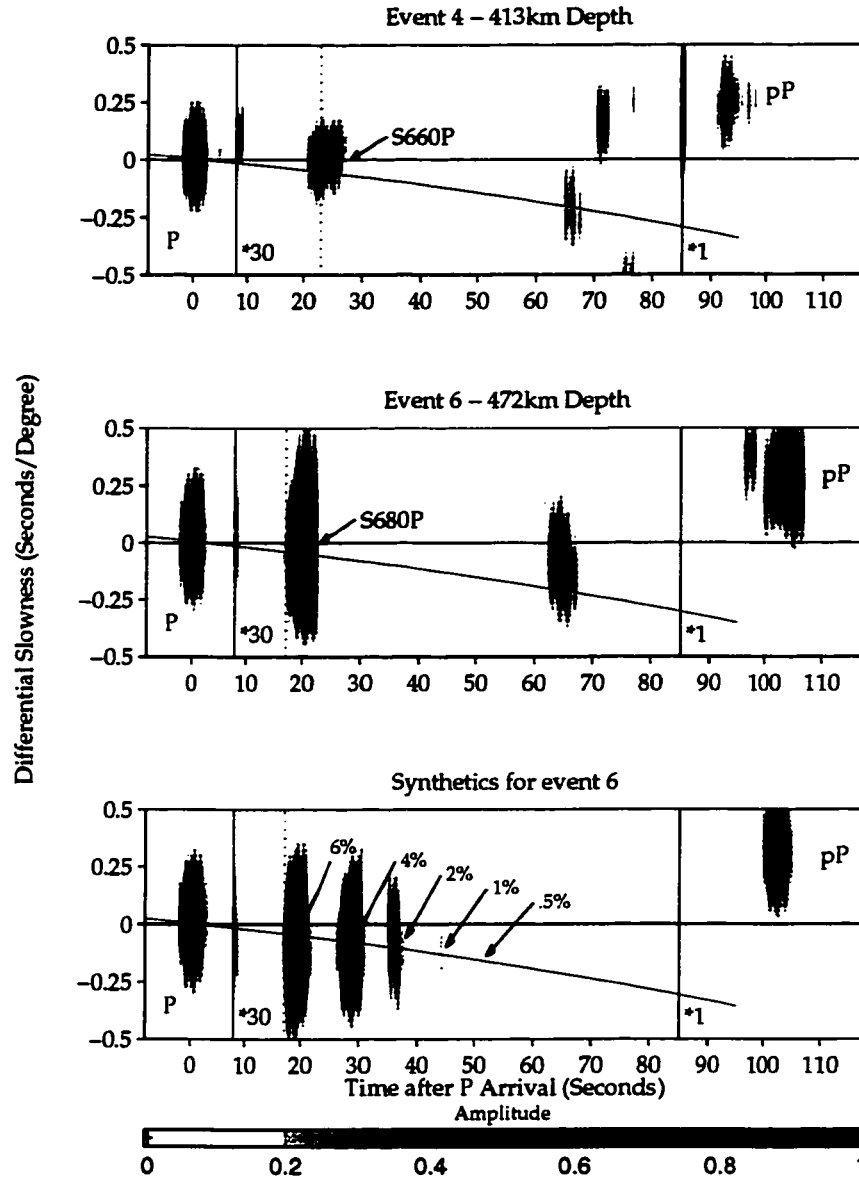

Figure 5.2: Slowness versus time vespegrams (the envelopes of N^{th} root stacked seismograms) for earthquake 4, earthquake 6, and synthetics created for event 6 with discontinuities at 680, 800, 900, 1000, and 1100km. High amplitudes indicate an arriving phase at that time and slowness. Between the two vertical solid lines, the data has been amplified by the amount shown. The vertical dashed line is the theoretical $S_{660}P$ arrival time and the curve follows the expected slowness of S to P converted phases.

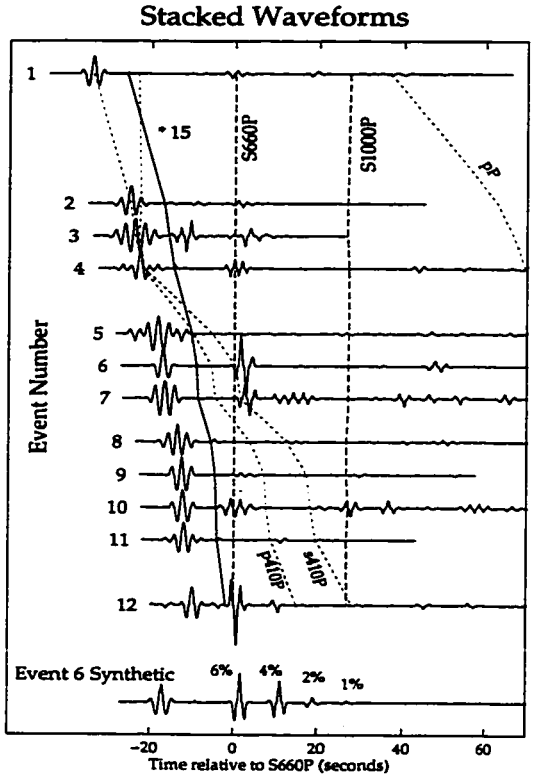

Figure 5.3: Slant stacks of seismograms from the twelve earthquakes aligned on the theoretical $S_{660}P$ arrival time. The first eight seconds, before the solid line, are stacked at the P slowness. The rest, right of the line, are stacked at the slowness expected for an S to P converted phase (as plotted in Figure 5.2) and increased 15 times in amplitude. Dashed lines mark theoretical arrival times of pP, $s_{410}P$, and $p_{410}P$ (which arrive at other slownesses), and $S_{660}P$ and $S_{1000}P$. An arrival from a discontinuity at a depth between 660 km and 1000 km would arrive in the time period between the graphed $S_{660}P$ and $S_{1000}P$ times. The slant stack from synthetics with added noise from event 6 is shown (bottom).

displays the latitude and longitude of these interaction points. Event 7 is anomalous in that its coda is very energetic for extended periods of time. The relative slowness of the energy at delay times of 35 and 55s is positive suggesting this energy is due to conversions off discontinuities above the earthquake. Thus, for each of these events (except 7), we can say unequivocally that there is no sharp discontinuity between 700 and 900 km, and five of these six events show no evidence for a discontinuity down to 1000 km.

The interpretation of the other five events is less reliable because of the unfavorable

radiation of down-going S-wave energy, and the intermittent observation of $S_{660}P$. However, they exhibit evidence for discontinuities at depths of 1000 (event 5); 1150 and 1250 (event 8); and 1200 and 1300 km (event 12). Events 8 and 11 show arrivals consistent with predicted times for $s_{410}P$ and $p_{410}P$. Figure 5.3 shows phases at about 40s for event 5 and at 10s for event 12, but these signals peak at incorrect slownesses for interpretations as S-to-P conversions beneath the events.

To determine our detection level, we create WKBJ synthetic seismograms [*Chapman*, 1978] of P, pP, and S_XP phases from discontinuities of 6, 4, 2, 1, and .5% at depths of 680, 800, 900, 1000, and 1100 km, respectively, generated from the *iasp91* velocity model [*Kennett and Engdahl*, 1991] modified to include these discontinuities. We used densities from PREM [*Dziewonski and Anderson*, 1981], and the USGS CMT double-couple solutions. For each station from event 6, we calculate a synthetic, convolve the instrument response, add random noise with the same power as was observed in the coda of the observed P wave, and apply identical processing as is applied to the data (bottom of Figures 5.2 and 5.3). The discontinuity at 680 km matches the event 6 data well in time, slowness and amplitude. The 1% discontinuity is clearly detectable in the synthetic and is larger than anything observed in the data except for $S_{660}P$ and the arrival at about 65 s, while the .5% discontinuity is below the detection threshold.

5.5 Conclusion

We clearly image the 660-km seismic discontinuity on all seven events where the source radiation pattern is favorable and find that it is depressed by up to 50 km, consistent with previous estimates for this region (e.g., *Vidale and Benz* [1992], *Wicks and Richards* [1993]). The stacked seismograms are very clean except for a distinct set of ten arrivals that could be interpreted as S-to-P conversions off approximately horizontal discontinuities. The problem is that they would be nearly uniformly distributed

between 900 and 1300 km depth, and as a result cannot be interpreted as a simple nearly horizontal discontinuity. An alternative explanation for most of these ten arrivals is scattering from one steeply dipping discontinuity that might be associated with a chemical discontinuity in an old subducted slab [*Castle and Creager*, 1996b]. Scattering off of dipping structures will produce arrivals with slownesses and times that may appear random unless properly migrated.

Many observations of seismic signals have been interpreted as isolated seismic discontinuities beneath 660 km [*Kawakatsu and Niu*, 1995, *Stunff et al.*, 1995]. We could argue for several more here. However, there is no evidence for a sharp discontinuity that is coherent over large horizontal spatial scales of thousands of km as one would expect for a chemical discontinuity that might separate the upper and lower mantle. Furthermore, synthetic modeling, such as for event 6, demonstrates that no discontinuity exists in the mantle below these events with a *S*-velocity contrast greater than 1%. Note that, unlike the SH reflection coefficient, the *S*-to-*P* transmission coefficient depends almost entirely on the jump in *Vs* and is insensitive to the change in density. Our constraint is only on *Vs* and not on density.

Thus, the clear evidence for a discontinuity depressed as much as 50 km, smaller than would be expected for a chemical boundary, is consistent with an explanation in terms of a thermally depressed phase boundary. At greater depths there are clearly no discontinuities beneath most events, which imposes constraints on a possible change in bulk chemistry. If it exists, it must [1] occur smoothly over a broad depth region so that our waves with 20 km wavelengths are unaffected by it, which is unlikely for a chemical boundary, or [2] occur within a depth of about 40 km of the phase change, also unlikely in a subduction zone, or [3] have a shear wave velocity contrast smaller than 1%.

5.6 Acknowledgments

We thank Drs. Weber and Wicks for discussions and fruitful ideas. Generously, Drs. Engdahl and Vidale provided earthquake locations and assembled waveform data. Comments by Drs. Bina, Clarke, Davies, Helffrich, van der Hilst, and Kennett helped improve the manuscript and are appreciated. This study was supported by grants from the National Science Foundation and the Fulbright Commission (J.C.). Much of the work was done while the authors were visiting the Australian National University.

Chapter 6

ANCIENT SLAB DEEP BENEATH IZU-BONIN

6.1 Abstract

By developing an efficient method to map seismic scatters in the earth, we imaged a subvertical structure parallel to and roughly 1000 km beneath the Izu-Bonin trench. The structure was imaged by $^1/_2$ to $^1/_5$ Hz waves, implying a sharp transition of less than 8 km width. Recent tomographic models image a similar structure [*Widiyantoro*, 1997, *Grand et al.*, 1997] that extends linearly southward from 30°N, beneath the middle of the Izu-Bonin trench, to beneath the Marianas trench. We interpret the sharp scattering surface as a subducted Moho and the tomographic image as the cold thermal anomaly of an ancient slab. The existence of this ancient slab implies that the southern half of the Izu-Bonin trench did not migrate with the northern half but from 45 Ma to 17 Ma remained a northern extension of the Marianas trench.

6.2 Introduction

Seismic images of the earth's interior reveal fundamental observations answering questions of the earth's structure, composition, and dynamics. Recent seismic tomographic models of the mantle's compressional [*van der Hilst et al.*, 1997] and shear [*Grand et al.*, 1997] wave velocities have been enlightening, showing features such as sheet like structures of seismicly fast material extending from trenches on the earth's surface to deep in the mantle. Complementary to tomographic models, which show regional average seismic velocities, are maps of seismic scattering in the mantle, which show areas where material properties vary rapidly. These sharp changes - disconti-

nuities - are caused by both mineralogical phase changes and chemical compositional changes and thus mark distinct mantle heterogeneities.

While using scattered waves, including reflected and converted phases, to image flat mantle discontinuities is a relatively standard procedure (e.g. *Flanagan and Shearer* [1998]), less work has been done using scattered waves to illuminate regional, 3-D structures. Previous deterministic scattering studies have used data migration techniques to image regional structures directly above the core in the D" region (e.g. *Krüger et al.* [1993] and *Lay and Young* [1996]) and in the crust beneath California [*Revenaugh*, 1995]. Mid-mantle scattering studies have thus far been limited to explanations of specific unusual observations in seismic waveforms [*Wicks and Weber*, 1996, *Castle and Creager*, 1996a, *Kaneshima and Helffrich*, 1998]. Expanding on these studies, we generated a migration method that is capable of using the entire seismic waveform to efficiently and routinely produce maps of mantle scattering.

6.3 Data and Method

We examined short-period teleseismic records from deep Izu-Bonin earthquakes traveling to short-period, vertical component seismometers located in the Western United States in one of three major seismic networks: the Pacific Northwest Seismic Network (PNSN), downloaded from the IRIS Data Management Center; the Northern California Seismic Network (NCSN); and the Southern California Seismic Network (SCSN). We used the *iasp91* velocity model [*Kennett and Engdahl*, 1991] for ray tracing and the hypocenters of *Engdahl et al.* [1998]. While P-to-P scattering could be similarly used, we examined the data for evidence of S-to-P scattering. This energy leaves earthquakes as a S (shear) wave, converts to a P (compressional) wave at a scatterer, and continues to the seismometers as a P wave, arriving after the primary P wave.

For each earthquake network pair, noisy traces were removed, seismograms were demeaned, 2 - 5 second bandpass filtered, normalized, and aligned on the P arrival.

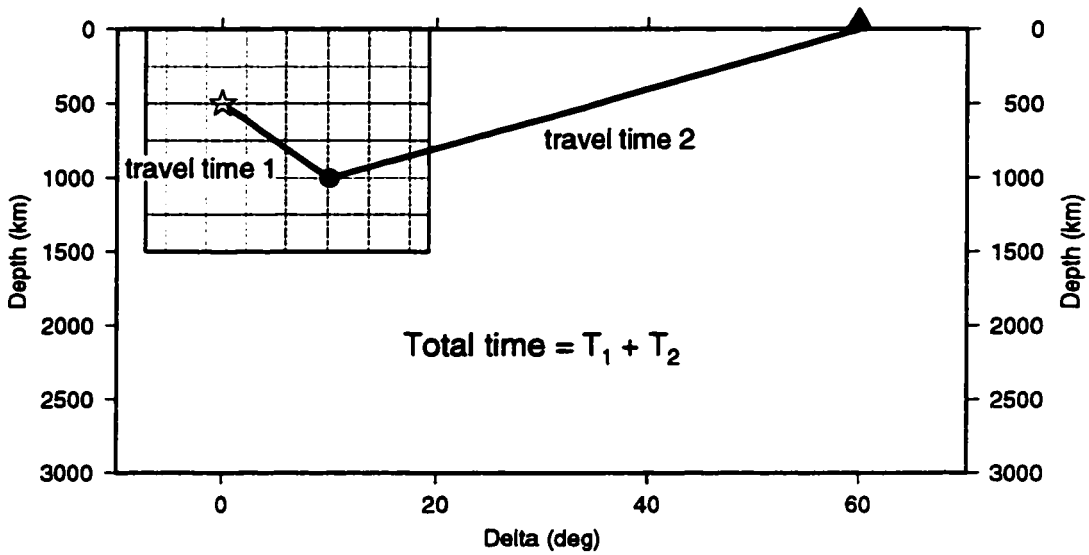

Figure 6.1: Schematic of the migration calculation on a grid surrounding an earthquake

We next migrated the amplitudes in each waveform to the locations at which they may have been generated. For this, we created a $0.1° \times 0.1° \times 10$ km grid surrounding the Izu-Bonin subduction zone. For a given earthquake/seismometer pair, we assigned each node in the grid a travel time by summing the time from the earthquake to the node as an S wave and the time from the node to the seismometer as a P (Figure 6.1). (P-to-P scattering could similarly be imaged by calculating travel times using P waves for both legs.) Using the travel time assigned to the node as an index, we next assigned the amplitude of the seismogram at that time to the node. If the time was within 5 seconds of the direct P wave or 8 seconds of the pP wave, we placed zeros at the node to prevent swamping from these high amplitude signals.

For energy arriving at a particular moment at a seismometer, the possible S-to-P scattering locations defined an isochronal surface similar in appearance to a 3-D "egg shell" surrounding the earthquake; a large amplitude arrival produced a bright "egg shell" (Figure 6.2). Subsequently, by combining - or stacking - an average of over one hundred seismograms per earthquake, the possible scattering locations were narrowed

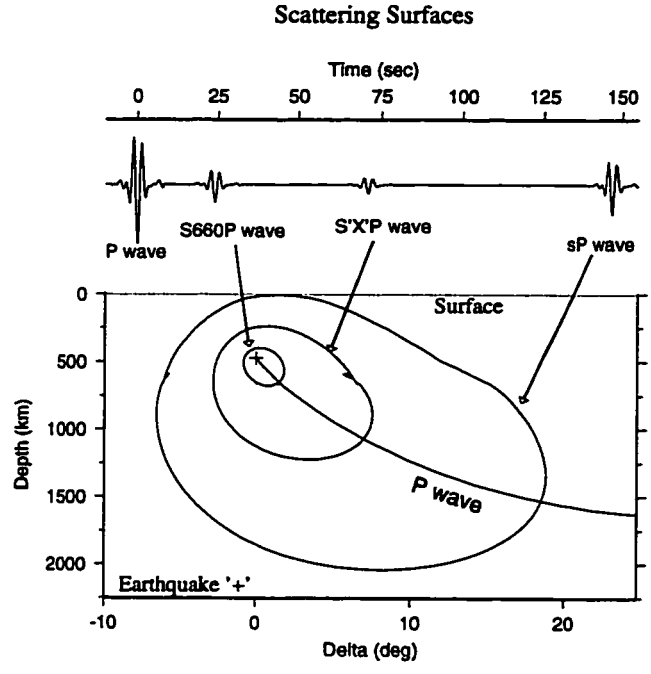

Figure 6.2: The egg-shells creating S-to-P conversions

down from large "egg shells" to narrow bright spots. We empirically found that an N^{th} root stacking method [*Muirhead and Datt*, 1976] with N=3 (mean if N=1) best improved the contrast between the signal and background noise. Additionally, at a point on the "egg shell", the tangent to the surface defines the orientation of the unique surface which scatters energy from the earthquake toward the receiver satisfying Snell's Law [*Castle and Creager*, 1998].

For a given S-to-P scatterer, stacking seismograms reduced the possible scatterer location to small regions. However, there often still existed ambiguities between two possible scatterer locations - a deeper location between the earthquake and the network and a shallower location behind the earthquake (relative to the network). As this non-uniqueness could only be attacked with additional information, we applied the same processing to twenty deep Izu-Bonin earthquakes and searched for evidence of scatterers in the same location.

6.4 Results

We first applied this procedure to 131 California network seismograms from a 521 km deep Izu-Bonin earthquake on January 1, 1992. Cross sections and maps through the resulting grid (Figures 6.3) show several bright signals. The 660-km discontinuity produced the brightest signal (Figure 6.3, upper two plots), in line with the results found in a recent detailed study of the discontinuity [*Castle and Creager*, 1998]. There were several additional signals present which showed other possible scatterer locations deeper in the mantle, including the one labeled scatterer "A" (Figure 6.3, lower two plots).

The timing of the signal producing scatterer "A" was such that if we had assumed it was from a flat surface, we would have identified the surface as a 1200-km discontinuity. However, as the highest amplitude of signal A was neither at the bottom of its "egg shell" nor along the great circle path, the scattering surface most likely is not flat but dips to the west with a northerly strike.

The same procedure was applied to twenty Izu-Bonin earthquakes, of which, seven showed evidence of a deep scatterer in the same location as scatterer "A" in Figure 6.3. To summarize the results, we plotted the highest probability locations from the seven events along cross section BB' (Figure 6.4). Note that while other surfaces were present in individual stacks, Figure 6.4 shows only the common surface. The scatterers defined a deep structure near 30°N, 145°E which extends from 800 km to 1200 km depth and has a dip of roughly 60°.

Certainly, while the scatterers appeared to arise from a similar structure, the observed locations did not precisely overlay one another but instead appeared "out of focus". In future work, we hope to address this issue by incorporating 3-D velocity models into the migration algorithm. Similar to work done in exploration seismology, the combined use of tomographic 3-D velocity models and scattering methods in both data interpretation and processing should prove dramatic.

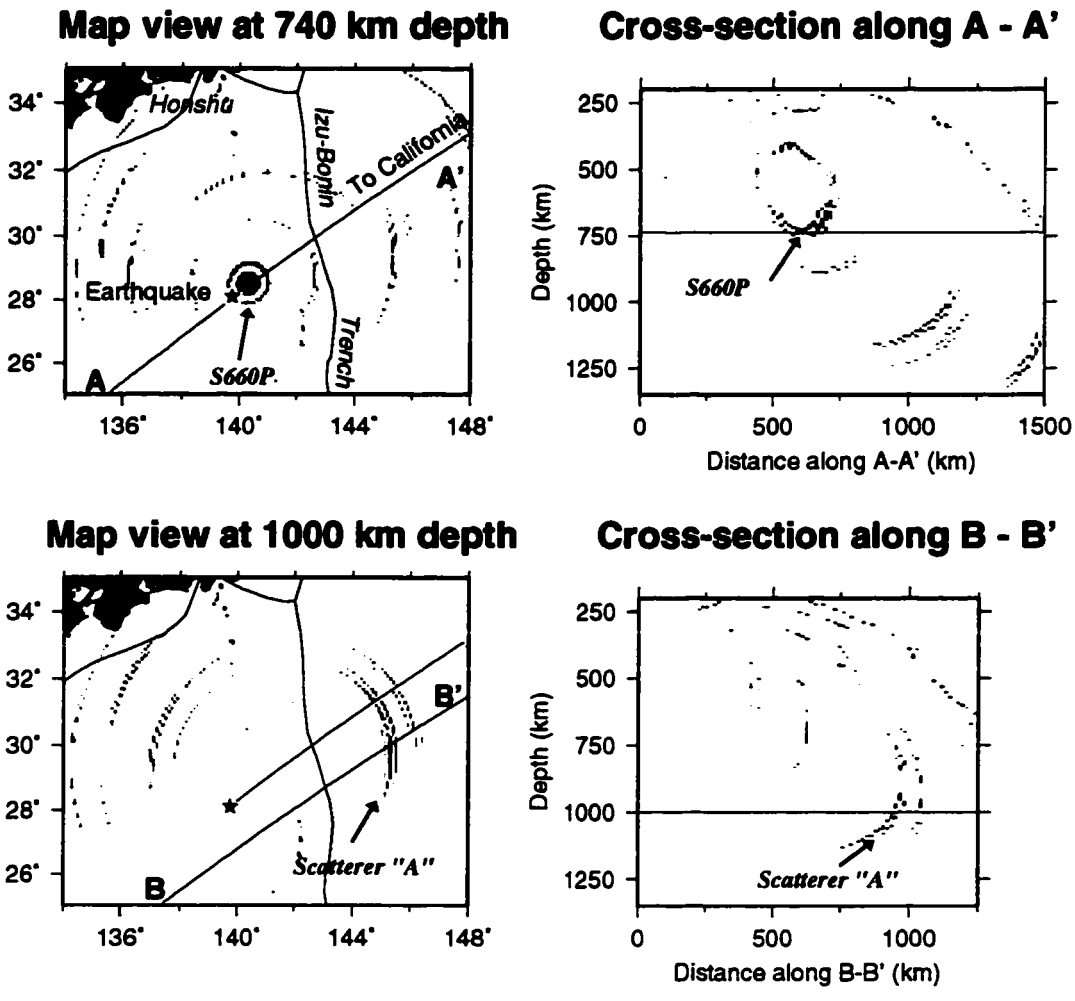

Figure 6.3: Sections through stacked data

Furthering our investigation of the structure, we examined the recent compressional and shear wave tomographic models from Widiyantoro and van der Hilst [*Widiyantoro*, 1997] and *Grand* [1994] , respectively. These models were constructed from data sources independent both to each other and to our data set and both primarily used hundreds of thousands of travel time picks of large amplitude body waves. The resolutions of the models are 1° (Widiyantoro) and 2° cubes (Grand). Figure 6.5 displays a map view of the *Widiyantoro* model at 950 km depth and Figure 6.6 shows the *Grand* model at 850 km. Both models show a finger of fast material extending

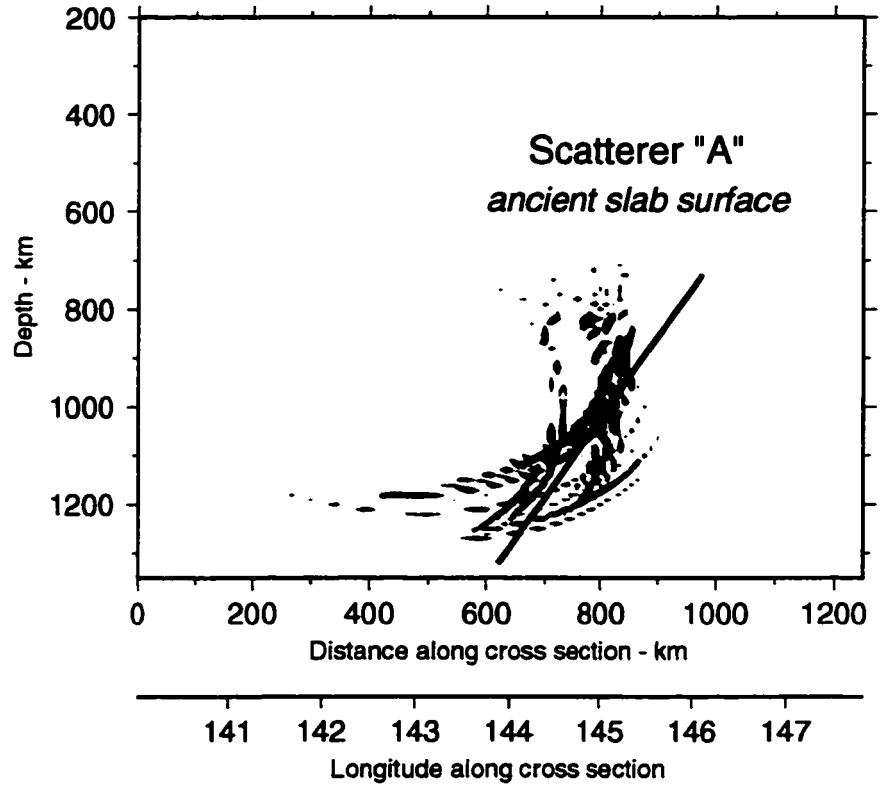

Figure 6.4: Several events

northward from the Mariana region to the scatterer near 30°N, 145°E.

6.5 Discussion

We imaged a structure using wavelengths of 10 to 30 km. As a rule of thumb, a scatterer can be seen only at wavelengths greater than 4 times its width [*Richards*, 1972], implying a sharpness of the surface of less than 8 km width. The tomographic images show a broad region of fast material in the same location. We interpret the scatterer as the sharp velocity contrast of a subducted Moho and the fast material in the tomographic images as the cold thermal anomaly of a subducted slab. Independently, either the tomographic images or the scattering image might be dismissed. Taken together, they present strong evidence that there exists a steeply dipping slab beneath

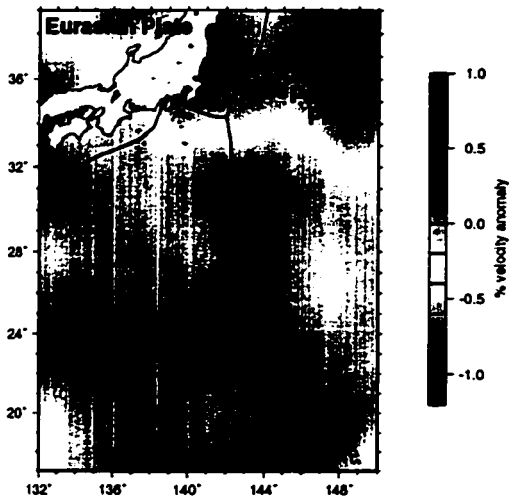

Figure 6.5: *Widiyantoro's* (1997) Vp model at 950 km

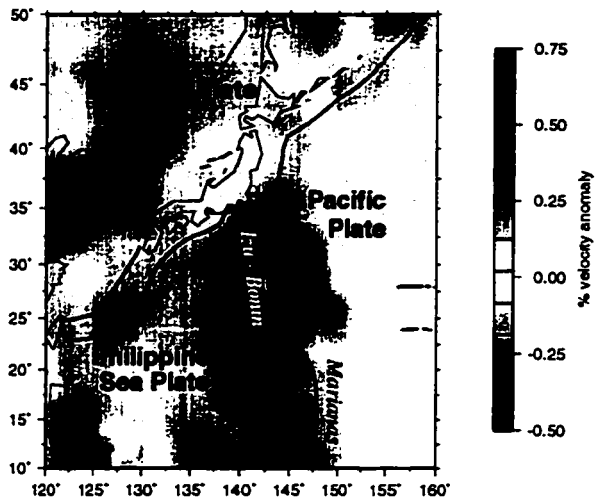

Figure 6.6: *Grand's* (1997) Vs model at 850 km

and parallel to the current location of the southern Izu-Bonin Trench.

As one additional piece of evidence, Figure 6.7 shows the location of subduction for the past 30 My from *Engebretson et al.* [1992] and *Richards and Engebretson* [1992]. Regionally, global models agree well (e.g. *Wen and Anderson* [1995]) . A ◇ marks the location of our scatterer from the short-period data. Note that the Pacific Plate subducts to the west at the Izu-Bonin Trench, placing the slab at the scatterer location.

Moho in the lower mantle

Several studies have debated the theoretical possibility of a chemically distinct body, such as a subducted Moho, existing in the lower mantle. *Gurnis* [1986] showed that a chemically distinct layer will remain chemically distinct once transported into the lower mantle. *Gaherty and Hager* [1994] showed that a subducting Moho, piggy-backing on a larger slab, will travel into the lower mantle. However, *van Keken et al.* [1996] and *Karato* [1997] recently showed that the ability of the larger slab to transport material into the lower mantle depends on the viscosities of the larger slab,

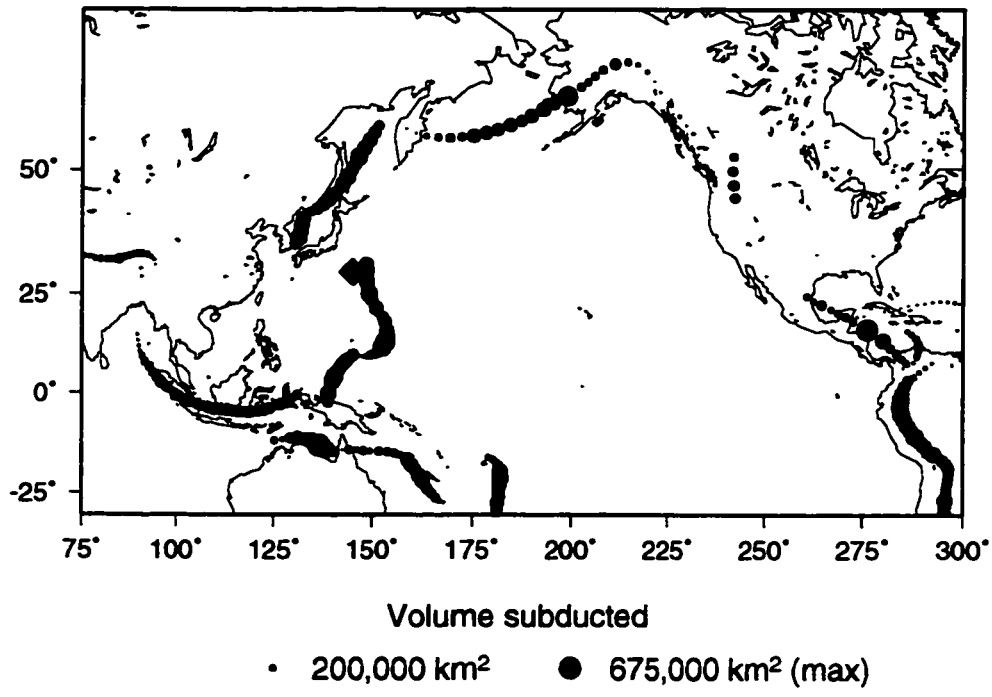

Figure 6.7: 0 - 30 My subduction from *Engebretson et al.* [1992] and *Richards and Engebretson* [1992]. A ◇ marks the scatterer location.

the crust, the Moho, and the ambient mantle; given certain values of these viscosities, the crust and Moho would delaminate and remain in the upper mantle as the rest of the slab enters the lower mantle. In this study, we show that in the Izu-Bonin and Mariana region, material can be transported into the lower mantle and, once there, remain distinct.

Lower mantle velocities

If the surface we imaged near 1000 km corresponds to the 30 My old material in the *Engebretson et al.* [1992] study, and if the slab sank through the upper mantle and transition zone (0 - 660 km) at the local convergence rate of 6 cm/yr [*Seno*, 1989], the material traveled through the lower mantle at 1.8 cm/yr.

Tectonic setting

We found evidence in the scatterer map and the tomographic models for a north-south trending slab near 1000 km depth at 144°E stretching from 30°N southward to the Mariana Trench. The Izu-Bonin subduction zone is complicated region where residual sphere analysis have been inconclusive [*Creager*, 1984] and strain analysis show extremely high strain in the subducting slab [*Yamaoka and Fukao*, 1986]. The slab, as defined by seismicity, changes from a moderately westerly dipping slab near 34°N to an over-vertical, recumbent slab near 26°N.

Regional plate reconstruction studies suggest that the Izu-Bonin Trench retreated rapidly to the northeast from 48 Ma to 17 Ma and advanced, either slowly or rapidly, westward from 5 Ma to the present [*Honza and Tamaki*, 1988, *Carlson and Mortera-Gutierrez*, 1990, *Otsuki*, 1990, *Seno et al.*, 1993]. Meanwhile, the Mariana Trench remained relatively stationary [*van der Hilst and Seno*, 1993]. In agreement with these reconstructions, studies of the 660-km discontinuity in the Izu-Bonin subduction zone [*Castle and Creager*, 1998] show a slab lying flat upon the 660-km discontinuity near 34°N, implying a previously rapidly retreating trench, and a slab subducting straight into the lower mantle south of 29°N, consistent with a more stationary trench.

We suggest here that the Japan-Mariana Arc was not a continuous feature. The northern portion of the Izu-Bonin Trench did not exist. Instead, the southern extent of the Japan Trench coincided with the present Nankai Trough, located to the northwest of the Philippine Sea Plate. The present southern portion of the Izu-Bonin Trench, or simply Bonin Trench, was a linear, northern extension of the Mariana Trench reaching to to 30°N. The dynamics of this point were similar to the current northern edge of the present Tonga Trench; material south of the point subducted while material to the north continued traveling north westward along the surface.

In the time period from 48 Ma to 17 Ma, the southern edge of the Japan Trench retreated to the east/northeast. This retreat deposited the slab upon the 660-km

discontinuity like pancake batter on a griddle, creating the fast anomaly seen in tomographic models (e.g. *Van der Hilst et al.* [1991]), the broad depression of the 660-km discontinuity (e.g. *Castle and Creager* [1998]), and a horizontal slab at 660-km depth [*Okino et al.*, 1989]. Meanwhile, the Bonin Trench remained a stationary northern extension of the Mariana Trench, creating the scatterer we imaged in the lower mantle. It then advanced slightly, as shown by the narrow, confined depression of the 660-km discontinuity and the recumbent slab as marked by current seismicity. The two trenches then met and connected to form the present Izu-Bonin Trench.

Chapter 7

OTHER DISCONTINUITIES BETWEEN 0 AND 660 KM DEPTH

7.1 Abstract

The depths and existence seismic discontinuities in the mantle place important constraints on the composition, state, and temperature profile of the mantle. We used 1/2 - 1/5 Hz converted and reflected teleseismic phases to investigate the upper mantle and transition zone to 660 km depth. At these frequencies, reflected and converted waves are sensitive to velocity changes that occur over less than 7 km. Below subduction zones, we found: (1) a sharp (< 3 km), well defined 660-km discontinuity; (2) no discontinuity between 660 and 410 km, consistent with a broad or non-existent 520-km discontinuity; (3) a small amplitude, inconsistently seen 410-km discontinuity; (4) no discontinuity between 410 and 200 km, consistent with a broad or non-existent 210 discontinuity; (5) no discontinuities between 200 km and 50 km; and (6) a 30 km thick crust at the Philippine Sea Plate that is not observed at South America.

7.2 Introduction

The location and existence of seismic discontinuities play an important role in unraveling the state of the mantle. At the surface of the earth, the temperature, pressure, state, and chemical composition of the rocks are well known. At the bottom of the mantle, the existence of a molten iron core places boundary conditions on the overlying mantle conditions. But the intervening 2850 km between the crust and the core leaves us considerable space to interpolate our knowledge. In this depth inter-

val, seismic discontinuities and their characteristics serve as reference points placing constraints on the thermal, chemical, and dynamical state of the mantle.

Numerous seismic studies in the first half of this century noted mantle discontinuities[1] by observing a sharp bends in the P wave travel time curve (e.g., *Byerly* [1926] and *Jeffreys* [1936]). Several recent seismic studies have examined the mantle specifically looking secondary arrivals arising from conversions and reflections at discontinuities. As these low amplitude secondary arrivals appear most coherent at low frequencies, studies using low frequency seismic waveforms have been numerous. For example, *Shear* [1991] and *Shearer and Flanagan* [1997], using low frequency (1/25 Hz) vertical and horizontal component seismograms, imaged discontinuities near 410, 520, and 660 km depths . *Revenaugh and Jordan* [1991a,1991b], using low frequency ScS reverberations, found large velocity jumps near 410 and 660 km depths and smaller contrasts near 30, 300, 520, 710, and 900 km, while *Zhang and Lay* [1993], using low frequency sS precursors, imaged upper mantle discontinuities at 80, 200, 330, and 400 km depths .

Shorter wavelength seismic data ($<$ 5 second periods) best reveal small scale features of discontinuities, such as limiting the minimum thickness of a discontinuity. Many investigations have used high frequency waves to examine the characteristics of specific discontinuities, including $P'P'$ studies (e.g. *Engdahl and Flinn* [1969] and *Whitcomb and Anderson* [1970]), PP studies (e.g. *Bolt* [1970]), and near receiver converted P-to-S and S-to-P studies (e.g. *Vinnik* [1977]). Studies using near source S-to-P converted phases to investigate discontinuities in subduction zones have also been numerous, including studies: searching for mid-mantle discontinuities between 700 km and 1200 km [*Kawakatsu and Niu*, 1994, *Castle and Creager*, 1997], map-

[1]Note that the word "discontinuity" is used to denote a depth which reflects or converts seismic energy; generally a depth at which the velocity increases faster than would be expected from first order effects from the mantle pressure and thermal profiles. Additionally, in this paper we will continue using the confusing nomenclature of calling a discontinuity by the depth at which it is occasionally observed (i.e. the discontinuity we call the 660-km discontinuity has been called the 650, 660, 670, and 690 km discontinuity).

ping the topography of either the 660-km discontinuity [*Wicks and Richards*, 1993a, *Niu and Kawakatsu*, 1995, *Castle and Creager*, 1998] or the 410-km discontinuity [*Collier and Helffrich*, 1997], and examining the sharpness of the 410 and 660 km discontinuities [*Yamazaki and Hirahara*, 1994].

Vidale and Benz [1992] conducted a survey of upper mantle (33 - 410 km) and transition zone (410 - 660 km) discontinuities using near source S-to-P conversions and p-to-P reflections. Rather than concentrate on one discontinuity, they used recordings of six earthquakes from large seismic networks to search the mantle for discontinuities at any depth. In this study, we expanded on their work: we used more data and additional analysis to examine the mantle between the crust and 660 km depth for signs of sharp discontinuities.

7.3 Data and method

The deployment of large, dense, regional digital networks and easy access to these data has allowed seismologists unprecedented opportunities. We gathered vertical component seismograms from short-period and broad band seismometers located in several networks and arrays: the Geyookcha Array in Turkmenistan, the Pacific Northwest Seismic Network (PNSN) in Washington and Oregon, the Southern California Seismic Network (SCSN), all downloaded from the IRIS Data Management Center in Seattle; and the Northern California Seismic Network (NCSN); the Grafenburg Regional Array (GRFN) in Germany, the German Regional Seismic Network (GRSN), both downloaded from the Erlangen Data Center; the Australian SKIPPY project; and the Gauribidanur Array (GBA) in India, downloaded from the Blackness Data Center. In total we analyzed 72 sets of records from 55 earthquakes in the western Pacific and South America (Tables 7.1 and 7.2).

We processed the data to look for small amplitude phases which are generated at discontinuities by either near source S (shear wave) to P (compressional wave)

Table 7.1: Short-period recordings

Event #	Date	Lon ° E	Lat ° N	Depth km	Mb	Network[a]	# Stations	Delta (deg)
				Izu-Bonin				
1	1982- 7- 4	137.0	27.9	547	6.3	NCSN	121	82.0
2	1984- 3- 6	138.9	29.4	456	6.2	NCSN	91	79.6
3	1984- 4-24	138.5	30.9	400	6.1	SCSN	99	83.2
4	1984- 4-24	138.5	30.9	400	6.1	PNSN	82	74.4
5	1985- 4- 3	139.6	28.3	472	5.9	NCSN	173	79.8
6	1985- 4- 3	139.6	28.3	472	5.9	PNSN	79	75.6
7	1985- 9-10	140.0	27.2	517	5.8	SCSN	103	84.4
8	1986- 2- 3	139.5	27.9	529	5.8	SCSN	74	84.5
9	1986- 2- 3	139.5	27.9	529	5.8	IND	19	59.3
10	1988- 9- 7	137.6	30.4	504	6.1	SCSN	60	84.1
11	1991- 5- 3	139.7	28.1	475	6.0	NCSN	103	79.3
12	1992- 1-20	139.5	28.0	521	5.8	NCSN	131	79.6
13	1992- 1-20	139.5	28.0	521	5.8	PNSN	97	75.9
14	1992- 5-30	141.9	30.8	12	5.9	PNSN	104	72.5
15	1992- 7-18	137.5	30.8	493	5.8	PNSN	99	75.3
16	1992- 8- 7	135.3	35.8	359	6.3	PNSN	102	73.0
17	1992- 8-29	138.2	33.3	306	6.0	NCSN	151	77.6
18	1992- 8-29	138.2	33.3	306	6.0	PNSN	111	73.0
19	1992-10-30	139.1	30.0	413	6.0	NCSN	116	79.1
20	1993- 7- 5	138.9	30.2	406	5.5	PNSN	92	74.8
21	1993- 7-20	140.0	27.4	461	6.1	PNSN	77	76.0
22	1993-10-11	137.9	32.0	357	6.4	GY	36	63.7
23	1993-10-11	137.9	32.0	357	6.4	PNSN	108	74.1
				elsewhere in the western Pacific				
24	1987-10- 6	145.0	18.8	510	6.7	IND	18	64.9
25	1987- 5-18	147.6	49.1	562	6.1	NCSN	75	62.4
26	1993- 1-18	145.7	18.4	152	5.6	SCSN	68	84.7
				South America				
27	1983-12-21	296.9	-28.2	604	6.2	NCSN	69	85.7
28	1984-10-20	293.2	-24.1	197	6.0	SCSN	93	75.7
29	1985- 5- 1	288.8	-9.2	605	6.0	NCSN	115	66.9
30	1986- 3-15	292.6	-19.2	232	6.0	SCSN	39	72.0
31	1989- 5- 5	288.6	-8.3	605	6.4	NCSN	87	65.0
32	1990-10-10	293.4	-19.6	262	5.8	SCSN	74	72.9
33	1990-10-17	289.2	-9.7	600	6.7	NCSN	111	66.7

[a] US = (PNSN, NCSN, and SCSN), IND = India, and GY = Geyookcha

Table 7.2: Broadband recordings

Event #	Date	Lon ° E	Lat ° N	Depth km	Mb	Network [a]	# Stations	Delta (deg)
				Izu-Bonin				
34	1980- 4-22	137.7	32.2	402	6.1	GER	13	85.8
35	1982- 7- 4	137.0	27.9	547	6.3	GER	13	89.1
36	1984- 3- 6	138.9	29.4	456	6.2	GER	13	88.7
37	1984- 4-24	138.5	30.9	400	6.1	GER	13	87.2
38	1985- 4-10	139.0	30.0	409	5.8	GER	13	88.3
39	1985- 9-10	140.0	27.2	517	5.8	GER	13	91.0
40	1985-10- 4	140.0	27.6	491	5.9	GER	13	90.7
41	1985-12- 3	140.5	27.0	439	5.9	GER	13	91.5
42	1986- 2- 3	139.5	27.9	529	5.8	GER	13	90.2
43	1986- 3-17	140.1	27.4	478	5.8	GER	13	90.9
44	1988- 9-13	138.7	30.0	456	5.8	GER	13	88.1
45	1989- 6-16	138.2	31.8	369	5.9	GER	13	86.3
46	1990- 8- 5	137.8	29.6	523	6.0	GER	12	88.0
47	1992- 1-20	139.5	28.0	521	5.8	GER	7	90.1
48	1992- 7-18	137.5	30.8	493	5.8	NCSN	8	81.3
49	1992-10-30	139.2	30.0	413	6.0	NCSN	9	79.6
50	1992-10-30	139.2	30.0	413	6.0	GER	9	87.9
51	1993-10-11	137.9	32.0	357	6.4	GER	10	85.7
				elsewhere in the western Pacific				
52	1980- 1-18	133.5	37.8	430	6.0	GER	12	79.2
53	1980- 3-31	135.6	35.5	363	6.1	GER	9	82.0
54	1981- 1- 2	128.2	29.3	232	6.1	GER	8	83.5
55	1982- 2- 3	135.7	36.9	341	5.6	GER	12	81.0
56	1984- 1- 1	136.8	33.7	386	6.5	GER	13	84.1
57	1985- 4- 3	139.6	28.3	472	5.9	GER	13	90.0
58	1986-12-21	122.5	25.5	271	6.1	GER	13	83.5
59	1987- 5-19	139.2	30.0	411	6.1	GER	13	88.4
60	1987- 6-12	122.2	25.5	267	5.8	GER	12	83.4
61	1987-10- 2	140.1	27.4	463	5.8	GER	12	91.0
62	1988- 9- 7	137.6	30.4	504	6.1	GER	9	87.1
63	1988-11- 5	136.0	37.2	334	5.9	GER	12	80.9
64	1990- 4-11	135.6	35.5	369	5.6	GER	13	82.1
65	1990- 4-14	140.2	27.3	466	5.6	GER	13	91.1
66	1990- 5-17	137.1	37.1	263	5.9	GER	12	81.4
67	1990- 8- 4	125.5	26.9	222	6.0	GER	7	84.2
68	1991- 5- 3	139.7	28.1	475	6.0	GER	13	90.2
69	1993-10-11	137.9	32.0	357	6.4	US	19	79.5
70	1994- 6-14	124.1	25.9	213	6.0	GER	7	84.5
71	1995- 3-31	135.0	38.2	355	6.0	AU	9	67.2
72	1995- 3-31	135.0	38.2	355	6.0	US	17	78.4

[a] AU = Australia (*SKIPPY*), GER = GRFN/GRSN, and US = (PNSN, NCSN, and SCSN)

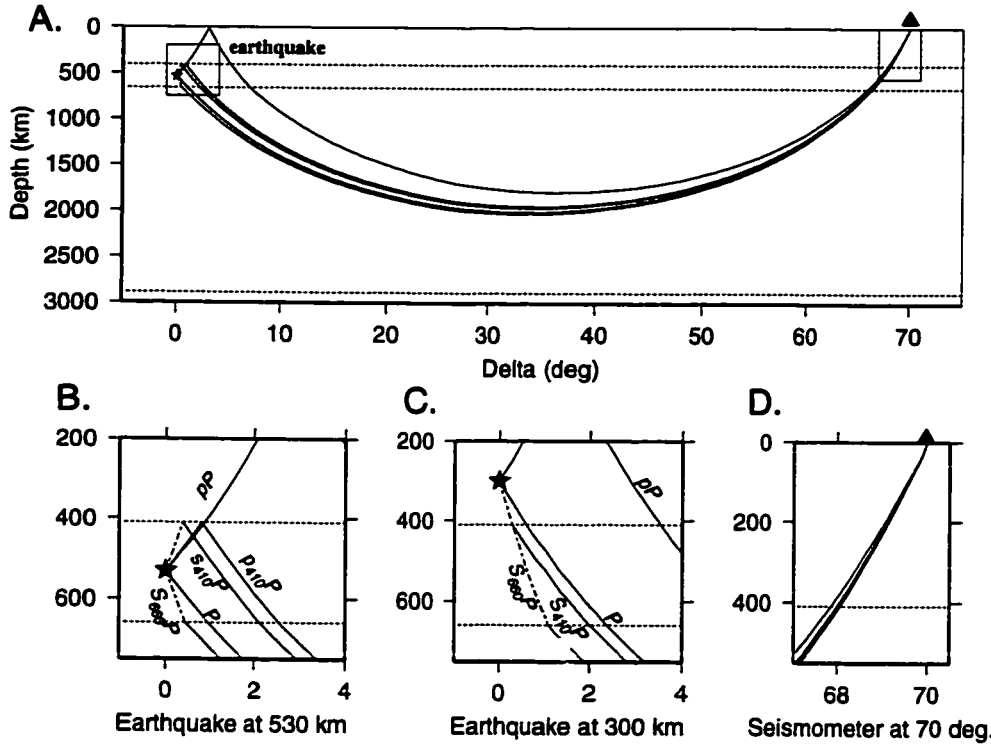

Figure 7.1: The ray paths

conversions, near source s-to-P conversion and reflections, or near source p-to-P reflections. Capital letters denote downgoing rays, lowercase letters denote upgoing rays, and a number denotes the discontinuity depth. For example, for an earthquake at 530 km depth, $S_{683}P$ defines the ray that leaves the earthquake as a downgoing S wave and converts and reflects to a P wave at a discontinuity at 683 km depth, $s_{403}P$ defines the ray that leaves the earthquake as an upgoing s wave and converts to a P wave at 403 km depth, and $p_{404}P$ defines the ray that leaves the earthquake as an upgoing p wave and reflects downward at 404 km depth. For an earthquake at 300 km depth, the phase mentioned above as $s_{403}P$ would be $S_{403}P$ and the phase $p_{404}P$ would not exist as it would be identical to the direct P wave. In each case, after the conversion or reflection near the source, the wave continues to the receivers as a P wave. Figure 7.1 schematically shows these phases for an earthquake at 530 km and

300 km depth.

These phases arrive in roughly the first minute after the P wave, in the P coda. The timing depends on the interaction depth and whether the first leg is a S or P wave. $S_{580}P$ arrives before $S_{590}P$ as it travels a shorter distance as a slower S wave. $p_{380}P$ arrives before $p_{370}P$ because it travels a shorter total distance. The phases also arrive at seismic networks at slightly different incoming angles. Relative to the direct P wave, upgoing phases from an earthquake at 450 km depth, such as $p_{350}P$ or $s_{350}P$, will arrive at shallower angles, while downgoing phases, such as $S_{550}P$, will arrive at a steeper angle. In seismological literature, this angle is called the "slowness", is defined as the reciprocal of the horizontal wavefront velocity, and has the inverse units of velocity (we used seconds per degree $[\frac{sec}{deg}]$). A steeper incoming ray has a smaller slowness as it travels across the network faster ("less slowly"). Ultimately, the combined use of the timing and the slowness of incoming arrivals reveals the depth of the discontinuity that generated each phase.

The amplitude of the secondary phases depends on the size of the discontinuity. Figure 7.2 shows the sensitivity of the three phases, $S_{660}P$, $s_{410}P$, and $p_{410}P$, to changes in the density, S wave velocity contrast, and P wave velocity contrast at a discontinuity [*Aki and Richards*, 1980]. For each line in each graph, the contrast of one property across the discontinuity was varied while jump of the other two properties were held constant. In A and B, the velocity and density contrasts were determined from contrasts across the 410-km discontinuity in the *iasp91* model [*Kennett and Engdahl*, 1991] and PREM model [*Dziewonski and Anderson*, 1981], respectively. For C, the values are taken from the *iasp91* 660-km discontinuity (velocities) and the PREM 670-km discontinuity (densities). For these calculations, a slowness of 6 sec/deg, as predicted for a P wave traveling from an earthquake at 400 km depth to a seismometer at 70°, was used.

The p-to-P reflected phases, such as $p_{300}P$, are sensitive to all three properties. If, for example, one found evidence of smaller than expected p-to-P reflection amplitudes,

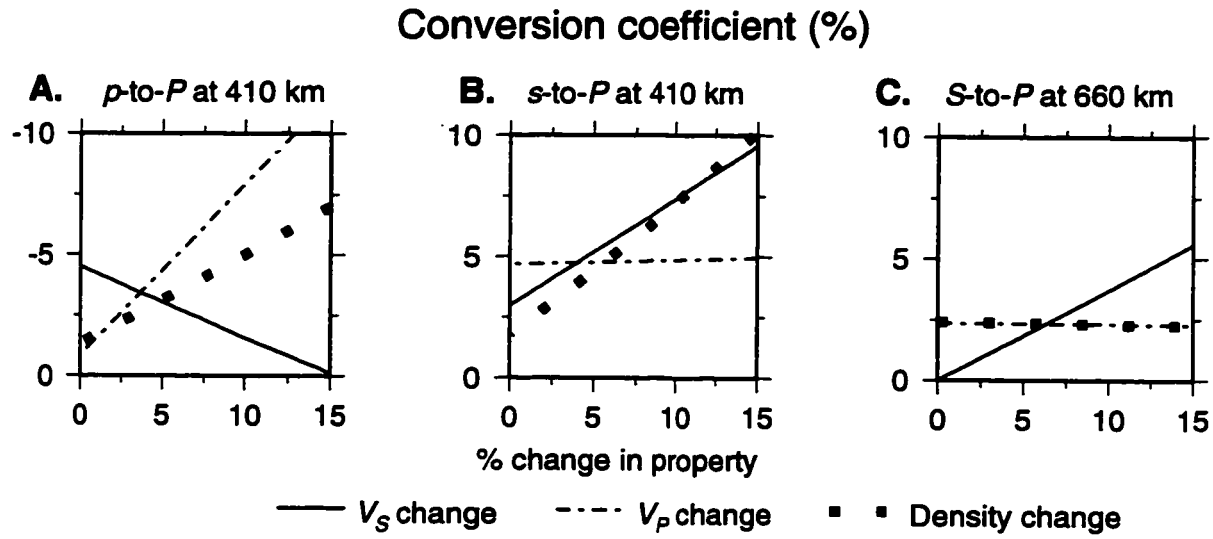

Figure 7.2: The p-to-P, s-to-P, and S-to-P conversion coefficients versus changes in the jump at the discontinuity. As one property is varied, the others remain at the *iasp91* (velocities) and PREM (density) values.

then either (1) the P wave velocity contrast is smaller than expected, (2) the density contrast is smaller than expected, or (3) the S wave velocity contrast is larger than expected. Upgoing s-to-P conversion and reflection amplitudes, such as $s_{410}P$, are sensitive to only the density and S wave velocity contrasts and are insensitive to P wave velocity changes. Finally, downgoing S-to-P conversions, such as $S_{660}P$, are sensitive to neither the density nor P wave velocity contrasts but only to the S wave velocity contrast.

Typically, large amplitude reverberations from near receiver structures swamp the first minute of individual seismograms, making observations of these near source converted phases difficult. However, the reverberations are incoherent across seismic networks. In fact, the structures under seismometers vary so much that the reverberations are even incoherent between seismometers only 50 km apart [*van der Lee et al.*, 1994, *Dewberry*, 1996]. While the ray paths are dispersed under the seismometers, they traverse similar paths near the source (Figure 7.1). Therefore, stacking seismograms reduces incoherent signals, mainly due to near receiver structures, and

enhances coherent signals, mainly from near source structures. The stacking was done with the N^{th} root stacking method [*Muirhead and Datt*, 1976], which we empirically found optimally improves the contrast between the signal and background noise at $N = 3$ (mean if $N = 1$).

We used seismic networks, such as the PNSN, covering the states of Washington and Oregon, as large aperture antenna to "focus" on energy arriving from specific directions. "Focusing" allowed better signal identification by isolating the slowness of incoming arrivals. We tuned the networks using a slant stack method (also known as a $\tau - p$ stack) which applies time shifts to seismograms based on the geographical distance of the seismometer from the earthquake.

In summary, for each earthquake/network pair, noisy traces were removed, seismograms were demeaned, 2 - 5 second bandpass filtered, normalized, aligned on the P arrival, and N^{th} ($N = 3$) root slant stacked. With the combined application of the N^{th} root and slant stack methods, our resolution of incoming arrivals was as good as $\pm$ 0.1 sec for timing and $\pm$ 0.1 sec/deg for slowness.

7.4 Results

We applied this procedure to event 13, an earthquake on January 20th, 1992. The results are displayed in a vespegram in Figure 7.3a. On an axis of slowness versus time, a vespegram displays the amplitudes of the stacked data after the envelope function has been applied. Relative to the P wave, the locations of dark spots indicate the timing and slowness of high amplitude seismic waves. Most obvious are the direct P wave, arriving at 0 sec and at 0 sec/deg, and the surface reflected pP wave, arriving at 115 sec and at 0.4 sec/deg. As expected, the surface reflected pP wave, which leaves the earthquake traveling upwards, has a positive slowness relative to the downgoing P wave. The smaller amplitude $S_{660}P$ and small $s_{410}P$ phases are also identifiable, arriving at 15 and 30 seconds. The amplitudes within the solid lines have been

increased by eight.

For comparison, we created 1 Hz complete synthetics (Figure 7.4) using the direct solution method (DSM synthetics) [*Cummins et al.*, 1994], the *iasp91* velocity model (with the 660 km discontinuity moved to 673 km, as observed in the data), the PREM density model, and the USGS double-couple focal mechanisms [*Sipkin*, 1986]. For each station in each earthquake/seismometer pair, we calculated a synthetic, convolved in the observed source time function (which included the instrument response and bandpass filter), added random noise with same power as in the observed P wave coda, and applied identical processing as was applied to the data. Comparison of synthetic and observed vespegrams confirms our interpretations as both show large amplitude P and pP phases in addition to small $S_{660}P$ and $s_{410}P$ phases.

Three lines overlay the vespegrams. The first, the dashed line, maps the slowness and timing of p-to-P reflections from structures of decreasing depth. The second, the longer solid line, maps the slowness and timing of upgoing s-to-P conversion reflections at structures of decreasing depths, and the third maps the slowness and timing of downgoing S-to-P conversions at increasing depths. Below the vespegram (Figures 7.3b and 7.4b), are plots of the data stacked along each line. As each time and slowness along a line corresponds to an interaction depth, time has been converted to depth along the ordinate. Using depth as the ordinate allows one to "unwrap" the vespegram and effectively display both the upgoing s-to-P and downgoing S-to-P conversions together along versus a common depth axis (Figures 7.3c and 7.4c).

When examining the stacked data, two additional considerations were: (1) "leakage" of energy between lines of stacked data and (2) the presence of arrivals from regional, dipping structures. Because a phase does not arrive at precisely one slowness, there is "leakage" between stacks. In Figure 7.3B, the $S_{660}P$ arrival stacks best at correct predicted negative (relative) slowness but also appears in both upgoing stacks as a $s_{470}P$ arrival and a $p_{450}P$ arrival. Leakage is bad between the s_xP and p_xP phases, which have little separation in slowness, and worst when attempting to

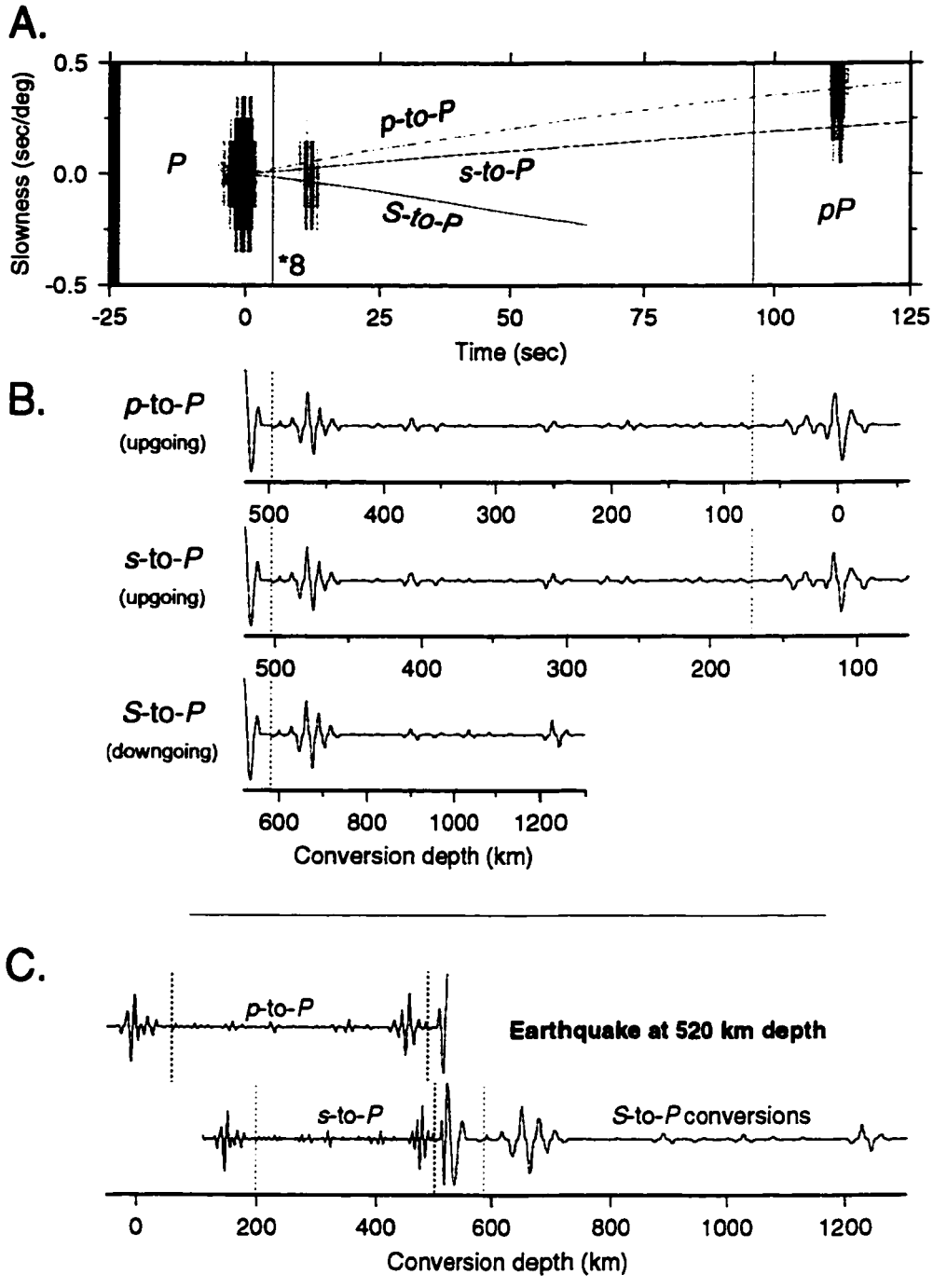

Figure 7.3: A. A 3^{rd} root vespegram for event 1992-01-20 recorded at PNSN. The area between the solid lines at 6 and 96 seconds has been increased eightfold. Also plotted are the expected arrival times and slownesses for the p-to-P, s-to$P$, and S-to-P phases. B. The traces are stacked along the slownesses shown in (A) and are again amplified between the dashed lines. The x-axis shows the interaction depth at each time. C. The stacks in (B) are plotted on a common depth scale depth and the S-to$P$ and s-to-P traces are plotted together.

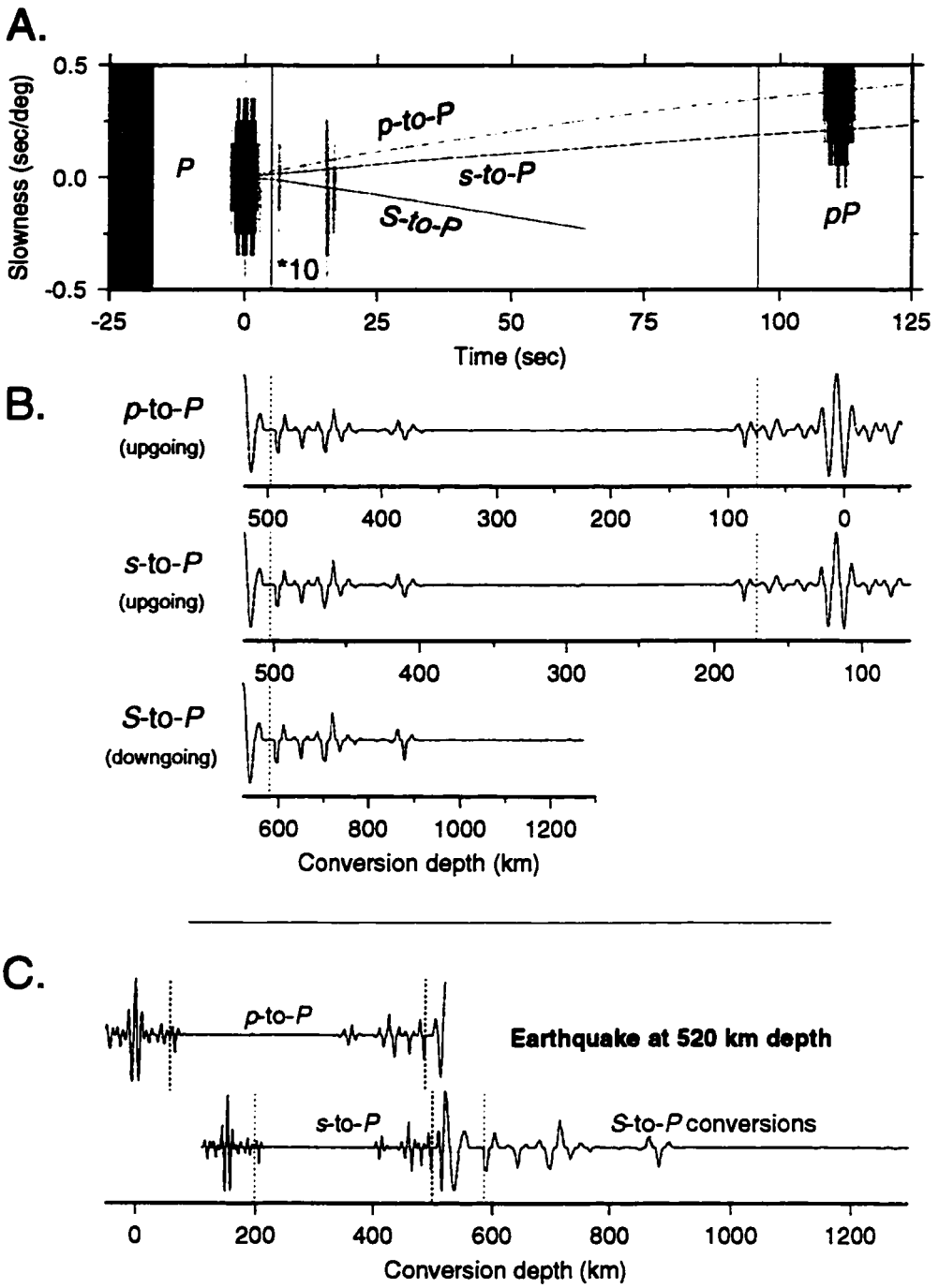

Figure 7.4: A DSM synthetic for event 92-01-20 to PNSN. A, B, C: As for Figure 7.3.

discern structures at depths near the earthquake depth, where all three phases, $S_X P$, $s_x P$ and $p_x P$, have almost no separation in slowness. The second problem is that local, 3-D structures, such as ancient slabs, also scatter seismic waves, producing phases that could be mistakenly interpreted as flat discontinuities at arbitrary depths. While searching for these regional structures is certainly of interest (chapter 6), we search here for horizontal or nearly horizontal global discontinuities.

The use of large data sets including earthquakes from several regions and at many depths mitigated both problems. Leaked energy from $S_{660}P$ appears as $s_{360}P$ phase for an earthquake at 460 km, but for an earthquake at 560 km, leaked energy from $S_{660}P$ appears as $s_{510}P$. Similarly, energy scattered from dipping structures will not appear at consistent depths, even for earthquakes in the same subduction zone, let alone for earthquakes in different regions. Thus, searching for signals at consistent depths from large numbers of well distributed earthquakes solved both the problems of leakage and non-global, non-horizontal structures.

Figures 7.5 (short-period) and 7.6 (broad-band) show the stacks of the $S(s)$-to-P conversions and reflections and Figures 7.7 and 7.8 show the stacks of the p-to-P reflections from the 72 events. The stacks are arranged by earthquake depth and, outside of a 10 second window center on the P wave, amplified by the amount shown. Plotted across the stacked data are roughly the times at which leakage from other phases might be expected. At the bottom of each page, a simple average of the absolute value of all the stacked data on the page, excluding the 10 second window around P wave, is plotted. The bottom plot shows the number of stacks that went into each point of the average stack. Note that the use of "#" in the following discussion refers to the number of the stack in each figure (on left axis) and not to the number in the previous tables.

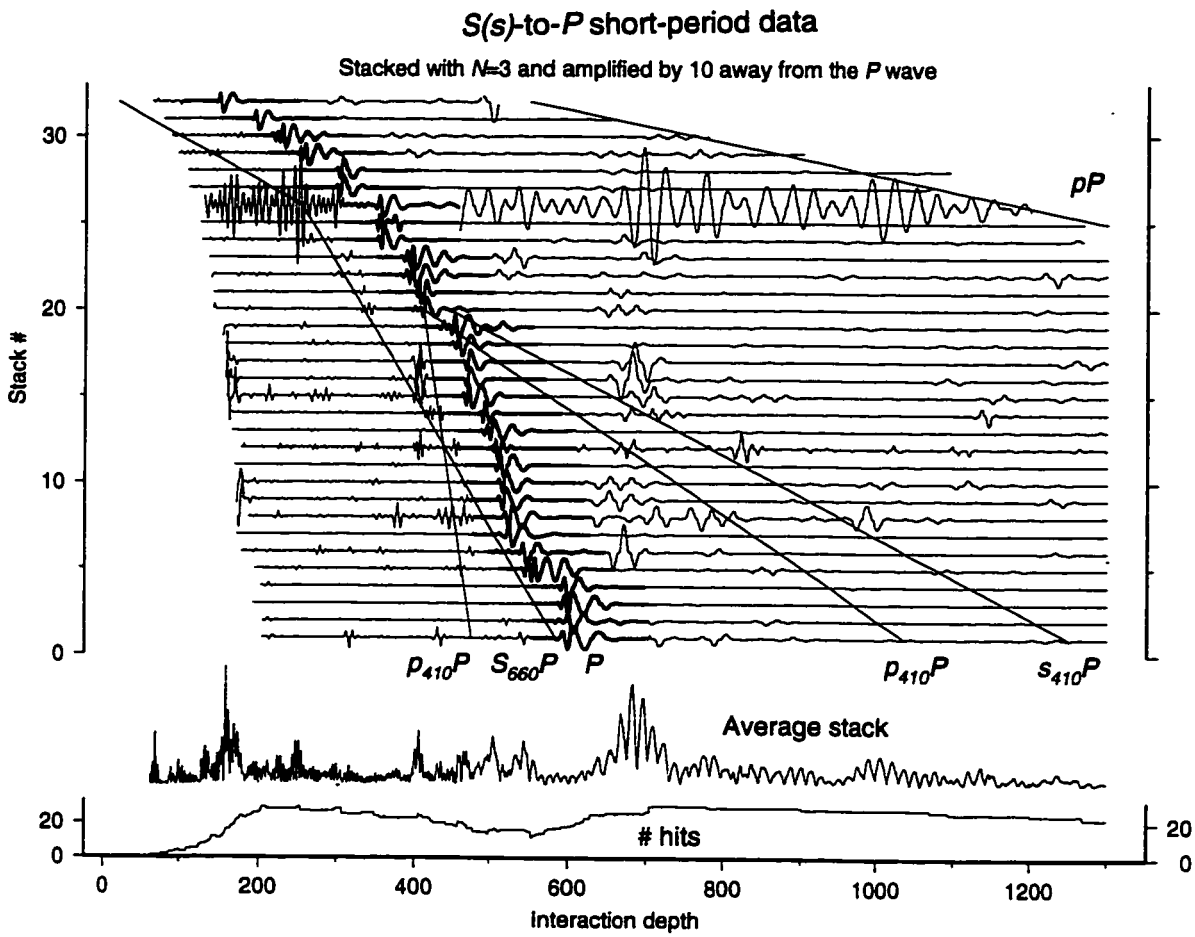

Figure 7.5: $S(s)$-to-P for short-period data

7.5 Discussion

7.5.1 Below 660 km

Several recent works have reported observations of deeper discontinuities, such as at 920 km [*Kawakatsu and Niu*, 1995], 1100 and 1200 km [*Wicks and Richards*, 1993b], and at 785 and 1200 km [*Stunff et al.*, 1995]. In this data set, no evidence exists for a global discontinuity between 750 and 1300 km depth [*Castle and Creager*, 1997]. We did occasionally observe energy arriving after the $S_{660}P$ phase, which we circle in Figure 7.9 (see chapter 5). The observations appear random unless one is willing to place

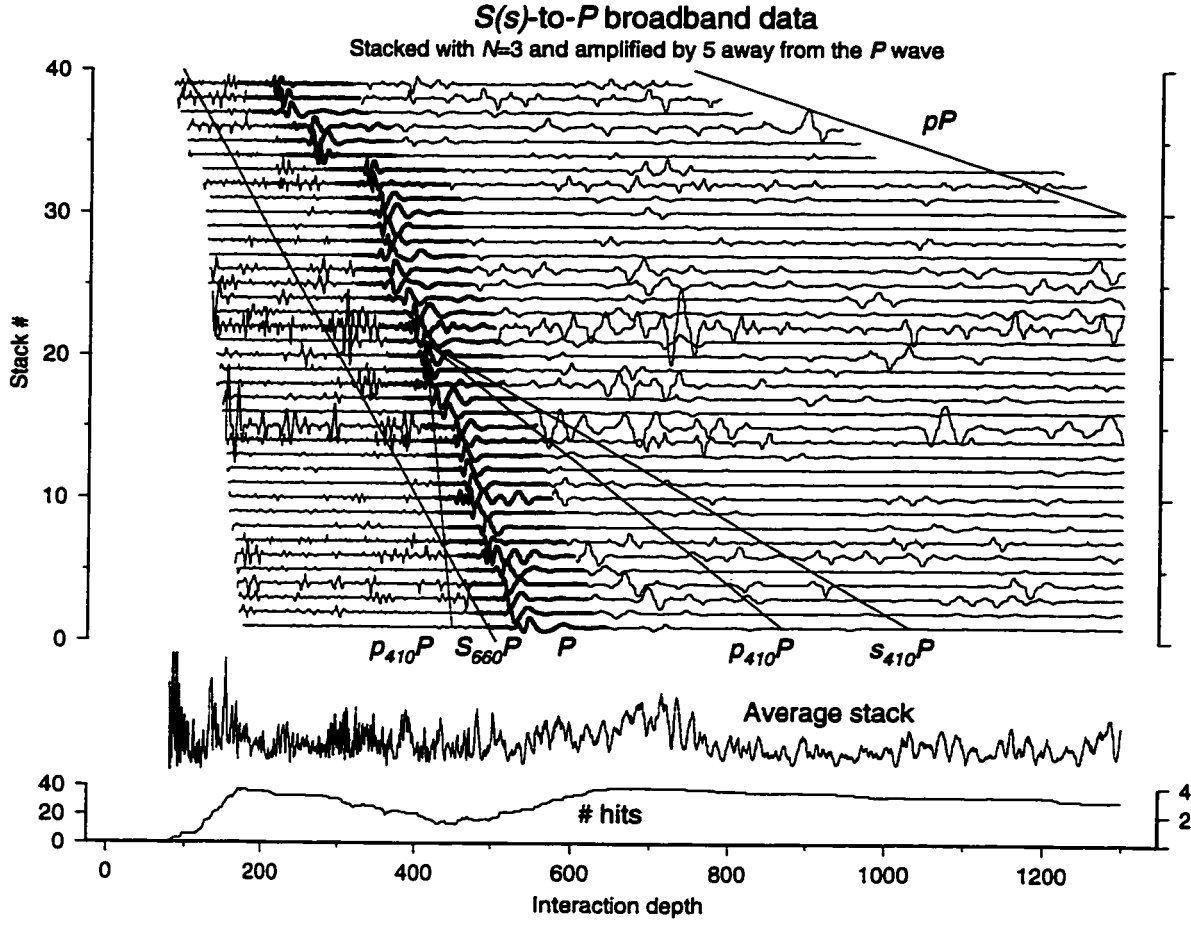

Figure 7.6: $S(s)$-to-P for broad-band data

at least five sharp flat discontinuities between 700 and 1300 km. Instead, these arrivals can be explained as energy generated at steeply dipping structures in the mantle ([*Castle and Creager*, 1996b, *Wicks and Weber*, 1996, *Kaneshima and Helffrich*, 1998] and chapter 6).

7.5.2 The 660 km discontinuity

Both in the individual stacks and in the average stack at the bottom of both the S-to-P figures (Figures 7.5 and 7.6), we observed the largest amplitudes between 660 and 720 km depth. These observations are in good agreement with the previous studies

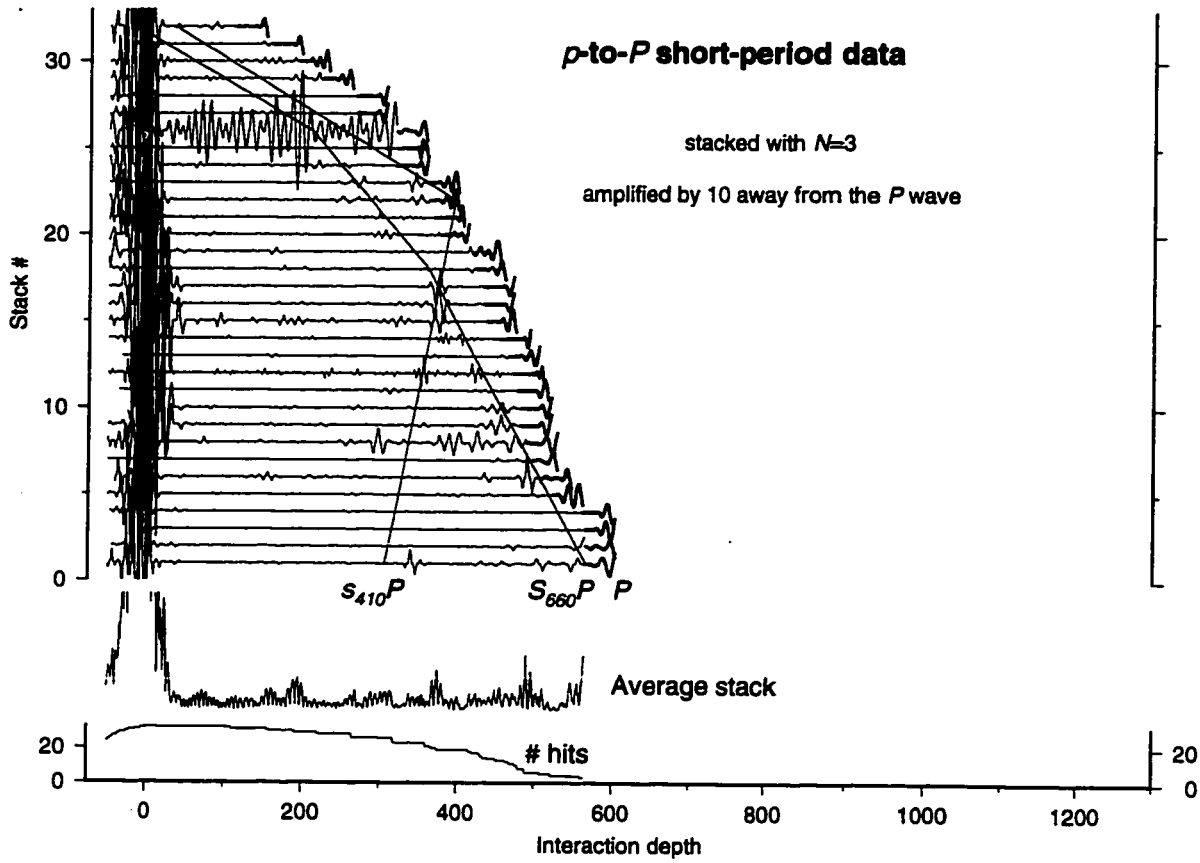

Figure 7.7: p-to-P for short-period data

of the 660 km discontinuity [*Wicks and Richards*, 1993a, *Niu and Kawakatsu*, 1995, *Castle and Creager*, 1998].

In the short-period stacks (Figure 7.5), the $S_{660}P$ phase was by far the dominant arrival. In the broadband stacks (Figure 7.6), we still observed the phase but it was much less dominant. It was tempting to relate this observation to the frequency content of the broadband versus short-period records and thus to the thickness of discontinuities. However, the average number of records in each short-period stack was 93 while the average number in the broadband stacks was 12. Additionally, whereas German broadband data since 1992 comes from the large German Regional Seismic Network, earlier German data, composing 70% of the broadband data, comes

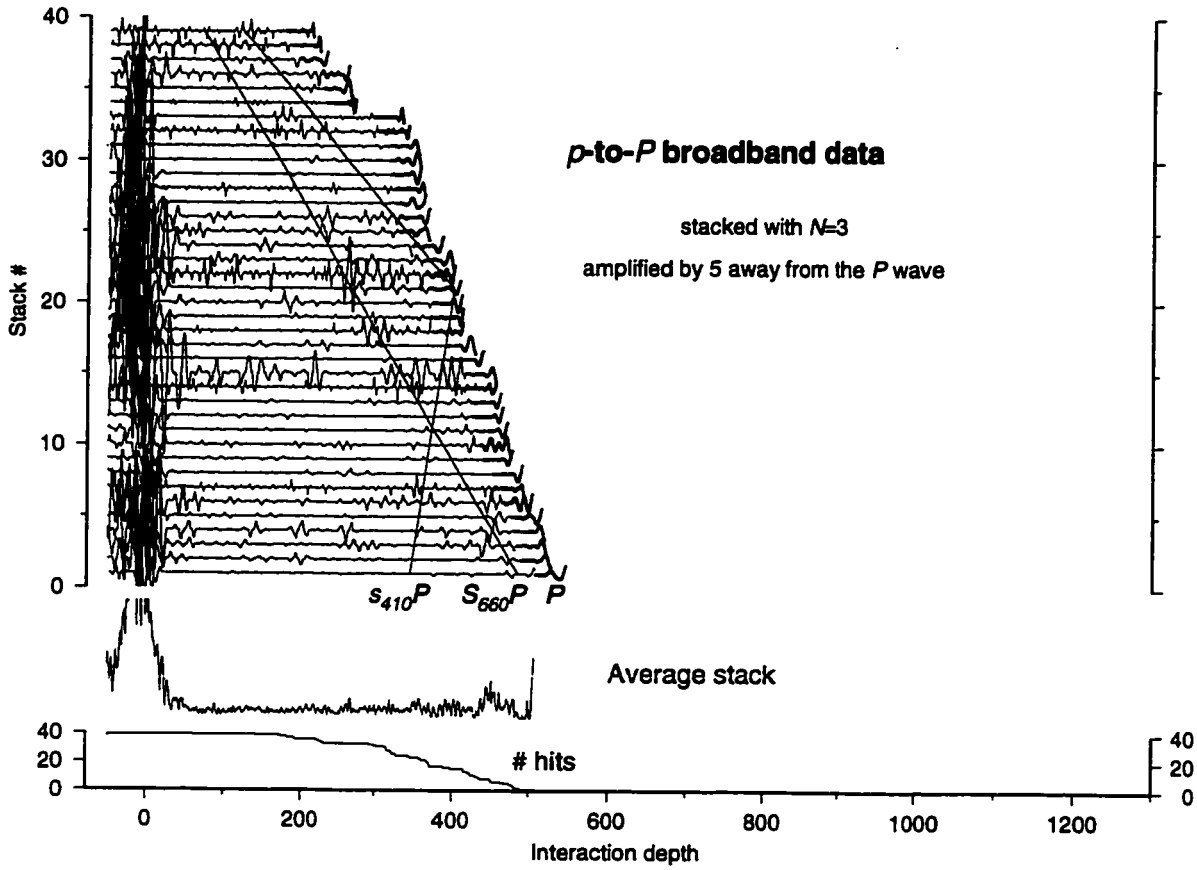

Figure 7.8: p-to-P for broad-band data

from the smaller Grafenburg array with an aperture of roughly 100 km. Clearly, the larger number of stations combined with the wide aperture (typically over 1000 km) of western United States short-period networks more effectively reduced noise and enhanced near-source signals in the stacks.

We also examined the frequency content of the $S_{660}P$ phase to determine the sharpness of the discontinuity. Figure 7.10 shows the stacked data from two earthquakes bandpass filtered at several different frequencies. 116 and 97 seismograms were stacked for the 92-10-30 earthquake (event 19, Table 7.1) and the 92-01-20 earthquake (event 13), respectively. The data were sampled at 10 Hz, bandpass filtered, aligned on the P wave, and linearly slant stacked (N=1) at the predicted slownesses for downgo-

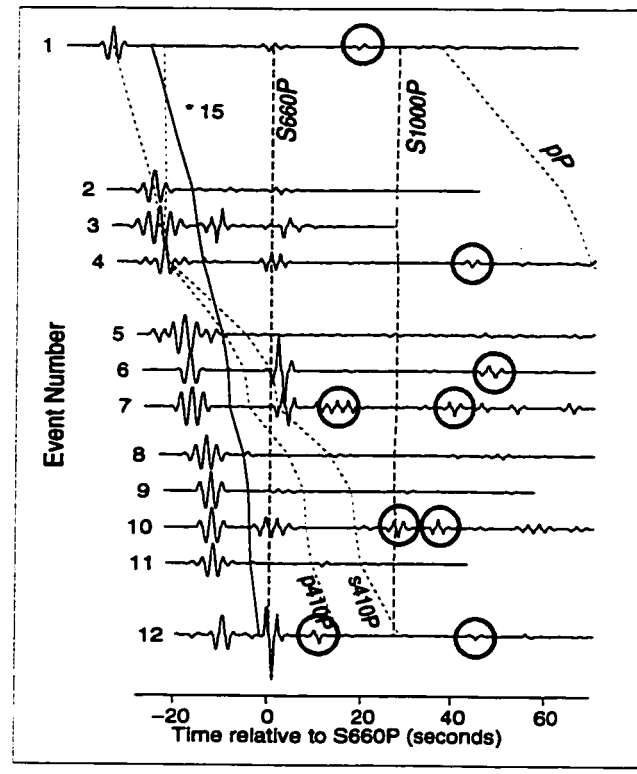

Figure 7.9: Stacked data with later arrivals. See Figure 5.3

ing S-to-P arrivals. The bandpass filters were butterworth filters with a cosine taper and 8 poles.

Figure 7.10A shows the results of using a 2-5 sec bandpass filter and applying a non-linear stacking ($N = 3$) algorithm. This was the method used to determine the depth of the 660-km discontinuity in the $S_{660}P$ analysis (chapter 2). For both earthquakes, the $S_{660}P$ phase is clear and the waveform matches the P waveform well. Figure 7.10B shows the results using the same filter (2 - 5 sec) but with linear stacking. Again, $S_{660}P$ phase is obvious. In C (2-3 sec) and D (1-2 sec), one can easily pick $S_{660}P$. $S_{660}P$ is arguably discernible in E (1 - 2 Hz). However, in F (2-3 Hz) and G (3-4 Hz), no $S_{660}P$ is visible.

$S_{660}P$ was observed at frequencies up to 1 Hz, above which it appears to rapidly

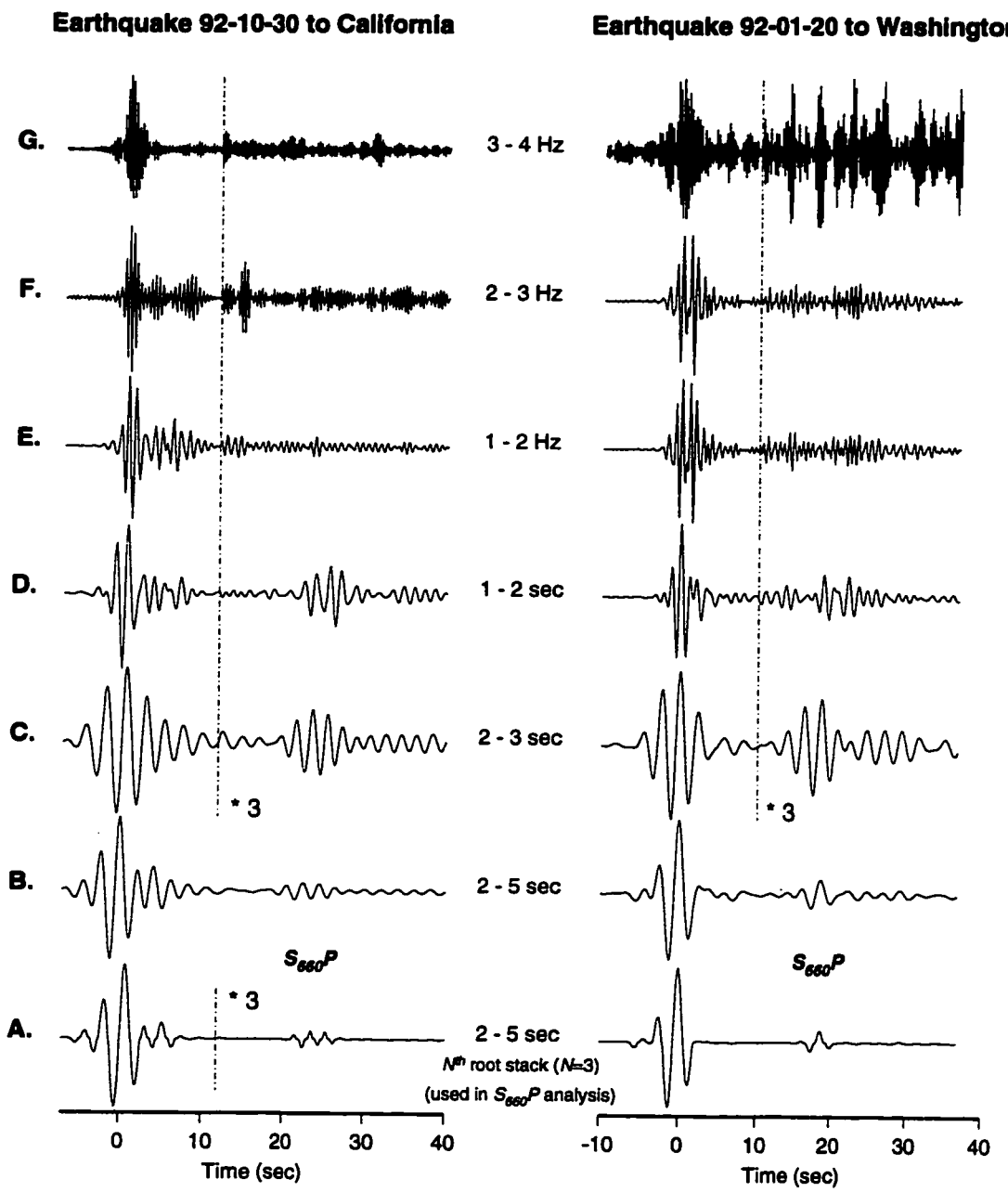

Figure 7.10: Observations of $S_{660}P$ at several frequencies

decrease in amplitude. One problem was that as the frequency window increased, the P wave became less similar between the traces; aligning the traces before stacking became increasingly difficult. This problem suggests that 1 Hz is the lower frequency bound at which $S_{660}P$ is visible. As shown by Figure 7.10, Figure 2.4 on page 18, and Figure B.2 on page 128, the $S_{660}P$ and P waves are also surprisingly coherent to at least $^1/_2$ Hz. *Richards* [1972] states that the minimum wavelength at which a discontinuity can be observed is roughly 4 times the thickness of the discontinuity. Using the *iasp91* shear wave velocity of 5.6 km at 660-km, $^1/_2$ Hz shear waves have a wavelength of 11.2 km, implying that the bulk of the velocity jump near 660-km occurs over a thickness of less than 3 km. This result is slightly smaller than previous estimates of 4 km [*Richards*, 1972, *Benz and Vidale*, 1993, *Yamazaki and Hirhara*, 1994].

These findings of a sharp 660-km discontinuity agree well with the laboratory measurements of *Ito and Takahashi* [1989] who found that the spinel to perovskite and magnesiowüstite phase change is complete over a depth interval smaller than 4 km.

Finally, as *Richards* [1972] concentrated on P-to-P reflections, improvements to this analysis of the 660-km discontinuity thickness include better modeling of S-to-P conversions, such as using DSM synthetics or Haskell propagator methods.

7.5.3 660 to 410 km depths

This depth range was difficult to image with the data. Because few of the earthquakes were at the bottom of this depth range, the p-to-P data provide little information for these depths. For the earthquakes in the depth range, the predicted $S(s)$-to-P arrival times are within 10 seconds of the direct P wave, effectively swamping smaller signals. Therefore, the numbers of stacks going into each average stack are low throughout the depth range.

We saw an occasional arrival, such as at 550 km in # 1, at 530 km in # 22 and

23, at 510 km in # 2 (Figure 7.5), and at 590 km in # 15 (Figure 7.6), although this last arrival is likely $s_{410}P$. However, this depth range appeared overall quite devoid of consistent arrivals. Using the velocities at these depths (5.1 km/sec to 5.6 km/sec) and at our 2-5 sec frequency range, this lack of observation implies that there are no discontinuities sharper than 7 km in this range. This agrees with $P'P'$ studies [*Benz and Vidale*, 1993] beneath the Indian Ocean, which found no discontinuities in this depth range sharper than 10 km.

Both the low frequency studies of *Shearer* [1991] (at 1/25 Hz) and *Revenaugh and Jordan* [1991a] (at 1/40 Hz) observed evidence for a discontinuity at 520 km that is at most 25 km thick. Candidates for this discontinuity include transformations of the olivine β-phase to γ-spinel, considered the most likely (*Revenaugh and Jordan*), and changes in pyroxene, garnet, or diopside. Whatever the phase change responsible for the observations, it must not only occur over a depth range of less than 25 km but also greater than 7 km.

7.5.4 The 410 km discontinuity

The olivine to α-spinel phase change creates the 410-km discontinuity [*Liu*, 1979]. While other short-period studies have previously reported frequent $s_{410}P$ and $p_{410}P$ observations [*Vidale and Benz*, 1992, *Benz and Vidale*, 1993, *Collier and Helffrich*, 1997], we found contradictory results here. We infrequently observed $S_{410}P$ and $s_{410}P$ and did not see $p_{410}P$.

In the average short-period $S(s)$-to-P stack (Figure 7.5), there appears a peak near 405 km. This is likely due to leakage from $S_{660}P$ in # 16 and 17. Similarly, the peak in the average stack of the $p_{410}P$ data at 380 km (Figure 7.7) appears largely due to leakage again from $S_{660}P$ in # 16 and 17. Observations of $s_{410}P$ include # 8 and 12 (Figure 7.5), and # 15 (Figure 7.6). # 38 and 39 (Figure 7.6) and # 29 and 30 (Figure 7.5) show $S_{410}P$ and # 8 (Figure 7.7) may be $p_{410}P$.

The absence of easily observed, large amplitude 410-km phases presents a puzzle.

A possibility is that topography on the 410 km discontinuity defocuses waves. Large variations in P-to-s scattering at discontinuities beneath Europe [*Paulssen*, 1985] suggest that the topography of a discontinuity can have a large influence on the amplitude of converted phases [*van der Lee et al.*, 1994]. Near a downgoing slab, the discontinuity would move to a shallower depth due to the cold slab and the positive Clapeyron slope of the olivine to spinel phase change. According to this argument, the resulting topography would diffuse and defocus the rays. Indeed, some, but not all, of the conversion points are close to where the slab passes through the discontinuity. The Clapeyron slopes of the olivine to α-spinel (near 410 km) and the γ to perovskite and magnesiowüstite (near 660 km) phase changes are roughly equal in absolute amplitude and the temperature gradients are of similar magnitude, suggesting that the same defocusing argument would apply to the 660 km discontinuity. However, we clearly observe the 660 km discontinuity.

Another possibility is that the *iasp91* model over predicts the size of the shear velocity jump across the 410-km discontinuity, such that smaller jumps in the material properties might explain the infrequent observations. In the *iasp91* velocity model, the jumps across the 410 km discontinuity are 3.7% (Vp) and 4.2% (Vs) compared to 5.8% (Vp) and 6.3% (Vs) across the 660 km discontinuity (Table 7.3). Using these values, the density jumps from PREM (5.9% at 400 km and 7.6% at 670 km), and a ray parameter of 5 sec/deg, the theoretical amplitudes of the phases generated at the 410-km discontinuity are 31% ($p_{410}P$), 116% ($s_{410}P$), and 53% ($S_{410}P$) the size of the $S_{660}P$ phase [*Aki and Richards*, 1980]. In the PREM model, the contrasts across 400-km, 2.6% (Vp), 3.4% (Vs), and 5.1% (density), are roughly half that across 670-km, 4.7% (Vp), 6.7% (Vs), and 9.7% (density). However, the amplitudes are still 23% ($p_{410}P$), 95% ($s_{410}P$), and 42% ($S_{410}P$) the size of the $S_{660}P$ phase. Thus, if this is the solution, the size of the jumps across the 410-km discontinuity are much less than half the size of those across the 660-km discontinuity.

Recent work on the 410-km discontinuity using a similar method by *Collier* [per-

Table 7.3: Percent change at each discontinuity

Property	Depth - iasp91/PREM					
	660/670-km		410/400-km		210/220-km	
	iasp91	prem	iasp91	prem	iasp91	prem
Vp	5.8%	4.7%	3.7%	2.6%	0.0%	7.1%
Vs	6.3%	6.7%	4.1%	3.4%	0.1%	5.1%
ρ	...	9.7%	...	5.1%	...	2.3%

sonal com., 1998] and *Xu et al.* [1998] along work by *Whitcomb and Anderson* [1972] also suggest that the 410-km discontinuity is much more difficult to observe than the 660-km discontinuity. Regional receiver functions studies by *Estabrook et al.* [1997] clearly image both discontinuities under China and Russia. However, under Japan, they observe only the 660-km discontinuity.

Revenaugh and Jordan's [1991] long period study found a larger contrast at the 410-km discontinuity (5.4% (Vs) and 3.9% (density)) than that in the *iasp91* model. *Shearer's* long period study found the P and S impedance contrasts at the 410-km discontinuity equal to those at the 660-km discontinuity. *Zhang and Lay* [1993] observed strong and consistent sS long-period precursors from a depth near 400 km ($s_{400}S$) beneath northwest subduction zones. Contrary to the short-period studies, each of these suggest that current models under-predict the size of the 410-km discontinuity.

Thus, we have two observations: [1] short-period studies with conversion points near subduction zones rarely see the 410-km discontinuity, [2] long-period studies, including those with conversion points in the subduction zone, consistently see the discontinuity. Explanation may be that the total width of the phase change is wider near a slab due either to the cold thermal anomaly [*Helffrich and Wood*, 1996, *Stixrude*, 1997], or to increased water content in the subducted slab [*Wood*, 1995]. In either case, the broadening of the discontinuity would make the discontinuity invisible at short-periods while still visible to the longer-periods.

7.5.5 410 to 210 km depths

Several works have found evidence for discontinuities in this depth range. *Revenaugh and Sipkin* [1994], using long-period ScS data, observed a discontinuity under the Sea of Japan and China at 330 km which they interpret as the upper limit of a silicate melt layer sitting on the 410-km discontinuity. *Zhang and Lay* [1993] observed weak evidence for the same feature.

We found no consistent signs of a discontinuity between 410 and 210 km. The noisy stack # 26, Figure 7.5, contains some energy near 270 km, however, this arrival is $S_{660}P$. # 22, Figure 7.6, has an arrival at 320 km which may be $S_{660}P$, and # 8, Figure 7.7, # 15, Figure 7.8 show arrivals which are probably $s_{410}P$. # 15, Figure 7.6, has an arrival at 300 km.

Thus, there exists no evidence for a sharp discontinuity in this depth range. The feature *Revenaugh and Sipkin* [1994] observed must be either broad or localized to the west of Izu-Bonin region.

7.5.6 The "210 km" discontinuity

At 210 km, the *iasp91* model has a miniscule shear wave discontinuity in Vs (.1%) and no discontinuity in Vp. On the other hand, the PREM model includes a large discontinuity at 220 km - 7.1% Vp, 5.1% Vs, and 2.3% density (Table 7.3). These velocity jumps are large - roughly twice as large as the 400 km discontinuity and equal in magnitude to the 670 km discontinuity. However, neither in the s-to-P reflections nor in the p-to-P reflections did we see any signs of such a large discontinuity near 210 km.

Sightings of the 220-km discontinuity in seismic data are extremely rare. *Revenaugh and Jordan* [1991b) found inconsistent evidence of a reflector between 200 and 300 km. *Shearer* [1991] and *Zhang and Lay* [1993], both at long-periods, found no evidence for a discontinuity near 210 km in P wave or S wave data under either conti-

nental or oceanic regions. Body wave studies of *Walck* [1984] , *Grand and Helmberger* [1984a), and *Grand and Helmberger* [1984b) found no evidence of a discontinuity at this depth.

These data imply that any discontinuity near 210 km must either be (1) a gradient zone wider than 25 km, (2) be extremely small, (3) very regional, (4) wide and have large topography, or (5) nonexistent. Future reference earth models (FREMs) should not include a sharp discontinuity near 210 km depth.

7.5.7 210 to 0 km depths

At these depths, the pP arrival swamps any s-to-P waves. Looking at pP reflections (Figures 7.7 and 7.8), no arrival stood out. *Revenaugh and Jordan* [1991] observed a positive impedance contrast near 60 km and a negative impedance contrast near 80 km, which they interpreted as the spinel to garnet phase change and as the lid of a low velocity zone, respectively, and *Zhang and Lay* [1993] observed a reflector at 66 km under Izu-Bonin. The structures giving rise to these long-period reflections must be broader than 4 km.

However, the pP arrival itself was intriguing and showed distinct regional variations. Table 7.4 tabulates the short-period data from the western Pacific and South America for which the pP phase was visible. Also listed is the location of the pP bounce point and the water depth at the bounce point. Figure 7.11 illustrates the difference between the pP arrival from the western Pacific earthquakes compared to the pP arrival from South America earthquakes. Figure 7.11A shows the linear stacks of the P and pP waves for the two groupings. For each stack, the traces were aligned on the given phase (P or pP), stacked, the envelope function was applied, and the resulting stack was normalized. The median stack is simply the median of the 13 (western Pacific) or 5 stacks (South America) plotted directly above it. Figure 7.11B and C compare the P and pP median stacks for each group. Finally, Figure 7.11D and E compare P to P and pP to pP between the groups.

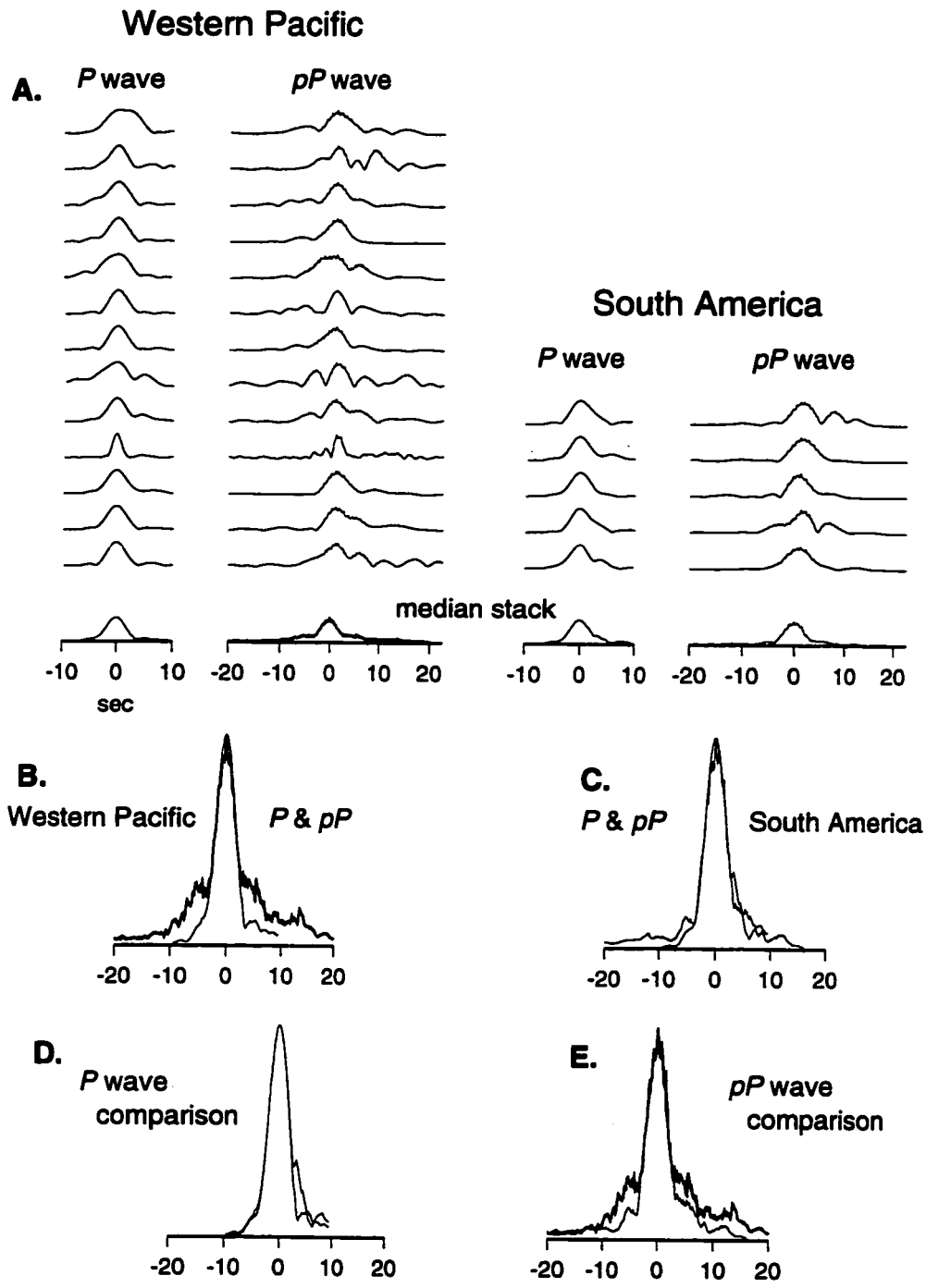

Figure 7.11: The pP compared to P. The western Pacific pP envelope is plotted thicker.

Table 7.4: Records used in the pP study

Event No[§]	Eq. Depth (km)	pP bounce point °E	°N	Water depth (meters)
		Western Pacific		
26	152	146.18	18.71	3463
18	306	139.43	34.28	487
16	359	136.80	36.98	-152
20	406	140.52	31.61	2062
19	413	140.85	31.10	2775
2	456	140.86	30.65	2501
5	472	141.61	29.57	3867
6	472	141.47	29.95	3948
11	475	141.74	29.44	3270
12	521	141.77	29.46	3453
13	521	141.66	29.81	3984
1	547	139.33	29.47	2598
25	562	152.79	50.71	979
		South America		
30	232	291.88	-18.45	...
32	262	292.58	-18.71	...
33	600	286.68	-6.87	...
29	605	286.23	-6.36	...
31	605	285.96	-5.39	...

[§] sorted by earthquake depth

The shapes of the P waveforms from the South America and from the western Pacific earthquakes were almost identical. However, the shape of the western Pacific pP waveform was distinct from both the P waveforms and the South America pP. There was increased energy arriving for 7 seconds before and for 5 seconds following pP.

A reflection from the surface of the ocean, pwP, explains the energy after the pP. The average water depth at the pP bounce points is 3 km and the speed of sound in water is 1.5 km/sec, resulting in a two-way travel time of 4 seconds.

Two possibilities for the energy arriving before the pP include reflections of off structure just below the surface or the effects of the slab as a waveguide. In the *iasp91* model, pP raypaths between deep Izu-Bonin earthquakes and the western United States seismometers leave the slab traveling upwards, bounce off of the surface above

the slab, and travel back, downwards, through the slab on the way to the stations. A wave traveling upwards within a slab with Vp 10% greater than *iasp91* would arrive roughly 4 sec early. However, because the slab is fast, it acts as an "anti-waveguide" such that the amplitude of this phase would be small. While seems reasonable as the precursor amplitude was small, the broadband German pP data from western Pacific earthquakes (not shown) also showed the precursor. The pP raypaths to Germany did not travel near the slab, making this explanation improbable.

The precursors may have come from regional structures. *Zhang and Lay* [1993] imaged the underside of the crust and found a crustal thicknesses of 33 km under Korea and 25 km under the Sea of Okhotsk, both with a shear wave impedance contrast of 26% that at the surface. Similarly, *Revenaugh and Jordan* [1991b] imaged a 26 km $\pm$ 7 km crust along a Bonin to receiver MAJO path. The precursor energy in our stack starts at -10 sec, increases rapidly until -7 sec, and is peaked at -5.3 sec. The energy peaked at -5.3 sec implies that the Philippine Sea Plate has a crustal thickness of 30 km ($p_{30}P$).

7.6 Conclusion

Using 72 network/earthquake pairs, we were able to gather information about upper mantle and transition zone discontinuities. The use of large numbers (> 50) of well dispersed seismograms was essential for noise reduction and slowness resolution. We found the frequency band between 2 and 5 seconds ($^1/_2$ to $^1/_5$ Hz) contained the most usable information from the short-period instruments. At higher frequencies, the traces became difficult to align and included fewer signals from the discontinuities. At lower frequencies, the slowness resolution drastically decreased, the timing resolution worsened, and the separation between arrivals became virtually nonexistent. Several stacking methods exist; for this work, the N^{th} root method with $N = 3$ worked extremely well. While the usefulness of worldwide seismic networks was partially

mitigated by the limited number of stations (< 15) in the networks outside of the western US, the inclusion of this data and comparisons of the data with the western US data proved advantageous.

Both the presence and lack of presence of small signals in the processed data placed constraints on the nature of the mantle. We found no signs of a horizontal or subhorizontal discontinuity between 660 km and 1300 km. The 660-km discontinuity was best imaged with 2-5 sec waves but was also observed at 1 Hz, suggesting that the discontinuity is less than 2 km thick. The 520-km discontinuity was not seen, implying that its thickness is at least 7 km thick. Similarly, the 410-km discontinuity was rarely observed. Possible explanations include discontinuity topography and broadening of the discontinuity. Broadening of the discontinuity could be accomplished by either the thermal effects of a cold slab on phase change or by the presence of water in the subducting slab. More work needs to be done to resolve this issue.

We observed no 210-km discontinuity. As neither short-period nor long-period studies studies observe this feature, its inclusion in reference earth models is unwarranted and incorrect. There was a crustal signal from earthquakes beneath oceanic provinces while none was observed from earthquakes beneath continental provinces. The crustal thickness of the overriding Philippine Sea Plate is roughly 30 km.

Chapter 8

FUTURE WORK

I feel chapter 2 (the topography of the 660-km discontinuity), chapter 4 (size of the 660-km discontinuity), chapter 5 (no structure beneath 660-km), and chapter 7 (other horizontal structures between 0 and 660-km) all considerably bettered previous studies by using improved methods and larger data sets.

Each one could also now be redone. There exist newer, slightly improved, stacking algorithms. There now exists considerably more data, including high quality broadband records. Using the broadband data and synthetic seismograms, one could investigate the depth profile of each discontinuity, i.e. do the phase changes really begin exponentially and asymptotically come to completion? *Niu and Kawakatsu* [1996] found one place where the 660-km discontinuity depth varied depending on the frequency of the waves. Is this feature real and related to the mineral physics of the phase change? One could also create a much larger map of the 660-km discontinuity topography by incorporating 660-km discontinuity depths from receiver function studies in Japan, Korea, China, and Russia. However, I feel that to redo any of the studies from these chapters would provide only marginal advancement.

On the other hand, chapter 3 (the connection between slab rheology and deep earthquakes) and chapter 6 (data migration to find a scatterer) are exciting new directions. Chapter 3 assimilates data from several sources, bringing together modeling, theoretical calculations, and observations. Our theory, that deep earthquakes are connected to olivine to spinel phase change, create a weak slab, eliminate the membrane strength, and allow the slab to fall downward, deserves consideration and further investigation.

I hope to continue the the study initiated in chapter 6. The migration algorithm, stacking, dataset are all first-attempts. Other, better techniques, such as migration methods used for near-surface seismic exploration, exist and should be adapted to this problem. And similar to exploration geophysics, where the interplay of tomographic and scattering (reflection) studies produce clearer images than either method alone, combining scattering studies with tomographic studies should result in dramatic results. While I have not dwelled on possible interpretations of a scattering map, my hope is that the maps will reveal heterogeneities throughout the mantle, whether they are global phase changes or the chemically distinct, 3-D, non-radial structures responsible for the geochemical signature observed at the surface.

REFERENCES

Aki, K. and Richards, P. *Quantitative Seismology.* W. H. Freeman and Company, New York, 1980.

Anderson, D. L. Composition of the mantle and core. *A. Rev. Earth planet. Sci.*, *5*, 179–202, 1977.

Bass, J. D. and Anderson, D. L. Composition of the Upper Mantle: Geophysical tests of two petrological models. *Geophys. Res. Lett.*, *11*, 237–240, 1984.

Benz, H. M. and Vidale, J. E. Sharpness of upper-mantle discontinuities determined from high-frequency reflections. *Nature*, *365*, 147–150, 1993.

Bina, C. R. Mutually consistent estimates of upper mantle composition from seismic velocity contrasts at 400 km depth. *Pure and Applied Geophysics*, *141*, 101–109, 1993.

Bina, C. R. Patterns of deep seismicity reflect buoyancy stresses due to phase transitions. *Geophys. Res. Lett.*, *24*, 3301–3304, 1997.

Bina, C. R. and Helffrich, G. Phase transition clapeyron slopes and transition zone seismic discontinuity topography. *J. Geophys. Res.*, *99*, 15853–15860, 1994.

Bolt, B. A. PdP and PKiKP waves and diffracted PcP waves. *Geophys. J. R. astr. Soc.*, *20*, 367–382, 1970.

Brudzinski, M. R., Chen, W. P., Nowack, R. L., and Huang, B. S. Variations of P wave speeds in the mantle transition zone beneath the northern Philippine Sea. *J. Geophys. Res.*, *102*, 11815–11828, 1997.

Burbach, G. V. and Frohlich, C. Intermediate and deep seismicity and lateral structure of subducted lithosphere in the Circum-Pacific region. *Rev. Gphys. Space Phys.*, *24*, 833–874, 1986.

Byerly, P. The Montana earthquake of June 28, 1925. *Bull. Seism. Soc. Am.*, *16*, 209–265, 1926.

Carlson, R. and Mortera-Gutierrez, C. Subduction hinge migration along the Izu-Bonin - Mariana arc. *Tectonophysics*, pages 331–344, 1990.

Castle, J. C. and Creager, K. C. Ancient structures in the mid-mantle (abstract). *SEDI 1996 Western Pacific Conference*, *77*, W140, 1996a.

Castle, J. C. and Creager, K. C. Imaging seismic velocity discontinuities of arbitrary orientation deep beneath Izu-Bonin (abstract). *Eos Trans. AGU*, *77*, 473, 1996b.

Castle, J. C. and Creager, K. C. Seismic evidence against a mantle chemical discontinuity near 660 km depth beneath Izu-Bonin. *Geophys. Res. Lett.*, *24*, 241–244, 1997.

Castle, J. C. and Creager, K. C. Topography of the 660-km discontinuity beneath Izu-Bonin: Implications for tectonic history and slab deformation. *J. Geophys. Res.*, *in press*, 1998.

Chapman, C. H. A new method for computing synthetic seismograms. *Geophys. J. R. astr. Soc.*, *54*, 481–518, 1978.

Chapman, C. H., Chu, J., and Lyness, D. G. The WKBJ seismogram algorithm. In *Seismologial Algorithms*, Doornbos, D. J., editor, page 47. Academic Press, New York, 1988.

Christensen, U. R. The influence of trench migration on the slab penetration into the lower mantle. *Earth Planet. Sci. Lett.*, *140*, 27–39, 1996.

Christensen, U. R. and Yuen, D. A. The interaction of a subducting lithospheric slab with a chemical or phase boundary. *J. Geophys. Res.*, *89*, 4389–4402, 1984.

Collier, J. and Helffrich, G. Topography of the "410" and "660" km seismic discontinuities in the Izu-Bonin subduction zone, 1997.

Creager, K. C., 1984. *Geometry, velocity structure, and penetration depths of descending slabs in the Western Pacific.* PhD thesis, University of California, San Diego.

Creager, K. C. and Boyd, T. M. The geometry of Aleutian subduction: Three-dimensional kinematic flow model. *J. Geophys. Res.*, *96*, 2293–2307, 1991.

Creager, K. C., Chiao, L. Y., Winchester, J. P., and Engdahl, R. Membrane strain rates in the subducting plate beneath south america. *Geophys. Res. Lett.*, *22*, 2321–2324, 1995.

Creager, K. C. and Ciao, L. Strain analysis in the Western Pacific. *in prep.*, 1998.

Creager, K. C. and Jordan, T. H. Slab penetration into the lower mantle beneath the Mariana and other island arcs of the northwest Pacific. *J. Geophys. Res.*, *91*, 3573–3589, 1986.

Cummins, P. R., Geller, R. J., and Takeuchi, N. DSM complete synthetic seismograms: P-SV, spherically symmetric, case. *Geophys. Res. Lett.*, *21*, 1663–1666, 1994.

Däßler, R., Yuen, D. A., Karato, S. I., and Riedel, M. R. Two-dimensional thermo-kinetic model for the olivine-spinel phase transition in subducting slabs. *Phys. Earth Planet. Int.*, *94*, 217–239, 1996.

Dewberry, S. R., 1996. *Crustal and Upper Mantle Structure for the Pacific Northwest from an analysis of short-period teleseismic network data.* PhD thesis, University of Washington.

Duffy, T. S. and Anderson, D. L. Seismic velocities in mantle minerals and the mineralogy of the upper mantle. *J. Geophys. Res.*, *94*, 1895–1912, 1989.

Dziewonski, A. and Anderson, D. L. Preliminary reference earth model. *Phys. Earth Planet. Int.*, *25*, 297–255, 1981.

Dziewonski, A. M., Chou, T. A., and Woodhouse, J. H. Determination of earthquake source parameters from waveform data for studies of global and regional seismicity. *J. Geophys. Res.*, *86*, 2825–2852, 1981.

Engdahl, E. R. and Flinn, E. A. Seismic waves reflected from discontinuities within Earth's upper mantle. *Science, 163*, 177–179, 1969.

Engdahl, E. R., van der Hilst, R. D., and Buland, R. P. Global teleseismic earthquake relocation with improved travel times and procedures for depth determination. *Bull. Seism. Soc. Am., submitted*, 1997.

Engebretson, D. C., Kelley, K., Cashman, H., and Richards, M. A. 180 million years of subduction. *GSA Today, 2*, 93–100, 1992.

Estabrook, C. and ??? Something to do with $p'p'$. *Nature, KCC*, 1996.

Estabrook, C., Li, X., Yuan, X., and Kind, R. Effects of the subducting Pacific Plate on the upper-mantle seismic discontinuities (abstract). *Ocean Hemisphere Project, 1*, 93, 1997.

Fischer, K. M., Jordan, T. H., and Creager, K. C. Seismic constraints on the morphology of deep slabs. *J. Geophys. Res., 93*, 4773–4783, 1988.

Flanagan, M. P. and Shearer, P. M. Global mapping of topography on transition zone velocity discontinuities by stacking SS precursors. *J. Geophys. Res., in press*, 1997.

Gaherty, J. B. and Hager, B. H. Compositional vs. thermal buoyancy and the evolution of subducted lithosphere. *Geophys. Res. Lett., 21*, 141–144, 1994.

Goff, J. A. and Jordan, T. H. Stochastic modeling of seafloor morphology: Inversion of sea beam data for second-order statistics. *J. Geophys. Res., 93*, 13589–13608, 1988.

Gordon, R. G. Present plate motions and plate boundaries. In *Global Earth Physics*, Ahrens, T. J., editor, pages 66–87. American Geophysical Union, 1995.

Grand, S. P. Mantle shear structure beneath the Americas and surrounding oceans. *J. Geophys. Res., 99*, 11591–11621, 1994.

Grand, S. P. and Helmberger, D. V. Upper mantle shear structure beneath the northwest Atlantic Ocean. *J. Geophys. Res., 89*, 11465–11475, 1984a.

Grand, S. P. and Helmberger, D. V. Upper mantle shear structure of North America. *Geophys. J. R. astr. Soc.*, *76*, 399–438, 1984b.

Grand, S. P., van der Hilst, R. D., and Widiyantoro, S. Global seismic tomography: A snapshot of convection in the Earth. *GSA Today*, *7*, 1–7, 1997.

Green, H. W. and Houston, H. The mechanism of deep earthquakes. *Annu. Rev. Earth Planet. Sci.*, *23*, 169–213, 1995.

Green, H. W., Young, T. E., Walker, D., and Scholz, C. H. Anticrack-associated faulting at very high pressure in natural olivine. *Nature*, *348*, 720–722, 1990.

Griffiths, R. W., Hackney, R. I., and van der Hilst, R. D. A laboratory investigation of effects of trench migration on the descent of subducted slabs. *Earth Planet. Sci. Lett.*, *133*, 1–17, 1995.

Guillou-Frottier, L., Buttles, J., and Olson, P. Laboratory experiments on the structure of subducted lithosphere. *Earth Planet. Sci. Lett.*, *133*, 19–34, 1995.

Gurnis, M. The effects of chemical density differences on convective mixing in the earth's mantle. *J. Geophys. Res.*, *91*, 11407–11419, 1986.

Gurnis, M. and Hager, B. H. Controls of the structure of subducted slabs. *Nature*, *335*, 317–321, 1988.

Hager, B. H. and Richards, M. A. Long-wavelength variations in earth's geoid: physical models and dynamical implications. *Geophys. J. R. astr. Soc.*, *328*, 309–327, 1989.

Hedlin, R. A. H., Sheaer, P. M., and Earle, P. S. Seismic evidence for small-scale heterogeneity throughout the earth's mantle. *Nature*, *387*, 145–150, 1997.

Helffrich, G. R., Stein, S., and Wood, B. J. Subduction zone thermal structure and mineralogy and their relationship to seismic wave reflections and conversions at the slab/mantle interface. *J. Geophys. Res.*, *94*, 753–763, 1989.

Helffrich, G. R. and Wood, B. J. 410km discontinuity sharpness and the form of the olivine α-β phase diagram: Resolution of apparent seismic contradictions. *Geophys. J. Int.*, *126*, F7–12, 1996.

Honza, E. and Tamaki, E. The Bonin Arc. In *The Ocean Basins and Margins*, Nairn, A. E. M., Stehli, F. G., and Uyeda, S., editors, volume 7A, pages 459–502. Plenum Publishing Corporation, 1985.

i. Karato, S. On the separation of crustal component from subducted oceainc lithosphere near the 660 km discontinuity. *Phys. Earth Planet. Int.*, *99*, 103–111, 1997.

Inoue, H., Fukao, Y., Tanabe, K., and Ogata, Y. Whole mantle P-wave travel time tomography. *Phys. Earth Planet. Int.*, *59*, 294–328, 1990.

Ito, E. and Takahashi, E. Postspinel transformations in the system Mg_2SiO_4 – Fe_2SiO_4 and some geophysical implications. *J. Geophys. Res.*, *94*, 10637–10646, 1989.

Jeanloz, R. Effects of phase transitions and possible compositional changes on the seismological structure near 650 km depth. *Geophys. Res. Lett.*, *18*, 1743–1746, 1991.

Jeffreys, S. H. The structure of the earth down to the 20°discontinuity. *Mon. Not. R. Astron. Soc. Geophys. Suppl.*, *3*, 401–422, 1936.

Kamiya, S., Miyatake, T., and Hirahara, K. How deep can we see the high velocity anomalies beneath the japan islands? *Geophys. Res. Lett.*, *15*, 828–831, 1988.

Kaneshima, S. and Helffrich, G. Detection of lower mantle scatterers northeast of the Mariana subduction zone using short-period array data. *J. Geophys. Res.*, *in press*, 1998.

Katsumata, M. and Sykes, L. R. Seismicity and tectonics of the Western Pacific: Izu-Marian-Caroline and Ryukyu-Taiwan regions. *J. Geophys. Res.*, *74*, 5923–5948, 1969.

Katsura, T. and Ito, E. The system Mg_2SiO_4 – Fe_2SiO_4 at high pressures and temperatures: Precise determination of stabilities of olivine, modified spinel, and spinel. *J. Geophys. Res.*, *94*, 15663–15670, 1989.

Kawakatsu, H. and Niu, F. L. Seismic evidence for a 920–km discontinuity in the mantle. *Nature*, *371*, 301–305, 1994.

Kawakatsu, H. and Niu, F. L. Depth variation of the "920km discontinuity" in the mid-mantle. *Eos Abstract Supplement*, *77*, 382, 1995.

Kennett, B. L. N. Seismic velocity gradients in the upper mantle. *Geophys. Res. Lett.*, *18*, 1115–1118, 1991.

Kennett, B. L. N. and Engdahl, E. R. Traveltimes for global earthquake location and phase identification. *Geophys. J. Int.*, *105*, 429–465, 1991.

Kincaid, C. and Olson, P. An experimental study of subduction and slab migration. *J. Geophys. Res.*, *92*, 13832–13840, 1987.

Kirby, S. H., Durnam, W. B., and Stern, L. A. Mantle phase changes and deep-earthquake faulting in subducting lithosphere. *Science*, *252*, 216–225, 1991.

Kirby, S. H., Stein, S., Okal, E. A., and Rubie, D. C. Metastable mantle phase transformations and deep earthquakes in subducting oceanic lithosphere. *Rev. Gphys.*, *34*, 261–306, 1996.

Krüger, F., Weber, M., Scherbaum, F., and Schlittenhardt, J. Double beam analysis of anomalies in the core–mantle boundary region. *Geophys. Res. Lett.*, *20*, 1475, 1993.

Lay, T. and Young, C. J. Imaging scattering structures in the lower mantle by migration of long-period s waves. *J. Geophys. Res.*, *101*, 20023–20040, 1996.

Lees, A. C., Bukowinski, M. S. T., and Jeanloz, R. Reflection properties of phase transition and compositional change models of the 670-km discontinuity. *J. Geophys. Res.*, *88*, 8145–8159, 1983.

Liu, L. G. Phase transformations and the constitution of the deep mantle. In *The Earth: its origin, structure and evolution*, McElhinny, M., editor, pages 177–198. Academic Press, London, 1979.

Lundgren, P. R. and Giardini, D. Seismicity, shear failure and models of deformation in deep subduction zones. *Phys. Earth Planet. Int.*, *74*, 63–74, 1992.

Muirhead, K. J. and Datt, R. The N^{th} root process applied to seismic array data. *Geophys. J. R. astr. Soc.*, *47*, 197–210, 1976.

Neidell, N. S. and Taner, M. T. Semblance and other coherency measures for multichannel data. *Geophys.*, *36*, 482–497, 1971.

Niu, F. and Kawakatsu, H. Direct evidence for the undulation of the 660-km discontinuity beneath Tonga: comparision of Japan and California array data. *Geophys. Res. Lett.*, *22*, 531–534, 1995.

Niu, F. and Kawakatsu, H. Complex structure of mantle discontinuities at the tip of the subdcuting slab beneath northeast China. *J. Phys. Earth*, *44*, 701–711, 1996.

Okino, K., Ando, M., Kaneshima, S., and Hirahara, K. The horizontally lying slab. *Geophys. Res. Lett.*, *16*, 1059–1062, 1989.

Otsuki, K. Westward migration of the Izu-Bonin trench, northward motion of the Philippine Sea Plate, and their relationships to the Cenozoic of Japanese island arcs. *Tectonophysics*, *180*, 351–367, 1990.

Paulssen, H. Upper mantle converted waves beneath the NARS array. *Geophys. Res. Lett.*, *12*, 709–712, 1985.

Paulssen, H. Lateral heterogeneity of Europe's upper mantle as inferred from modelling of broad-band body waves. *Geophys. J. R. astr. Soc.*, *91*, 171–199, 1987.

Pullen, J., Creager, K. C., and Malone, S. Broadband array study in the Puget Sound region. *Eos Abstract Supplement*, *76*, 416, 1995.

Revenaugh, J. The contribution of topographic scattering to teleseismic coda in southern California. *Geophys. Res. Lett.*, *22*, 543–546, 1995.

Revenaugh, J. and Jordan, T. H. Mantle layering from ScS reverberations, 2: The transition zone. *J. Geophys. Res.*, *96*, 19763–19780, 1991a.

Revenaugh, J. and Jordan, T. H. Mantle layering from ScS reverberations, 3: The upper mantle. *J. Geophys. Res.*, *96*, 19781–19810, 1991b.

Revenaugh, J. and Sipkin, S. Mantle discontinuity structure beneath China. *J. Geophys. Res.*, *99*, 21911–21927, 1994.

Richards, M. A. and Engebretson, D. Large-scale mantle convection and the history of subduction. *Nature*, *355*, 437–440, 1992.

Richards, M. A. and Wicks, Jr, C. W. S–P conversion from the transition zone beneath Tonga and the nature of the 670 km discontinuity. *Geophys. J. Int.*, *101*, 1–35, 1990.

Richards, P. G. Seismic waves reflected from velocity gradient anomalies within the Earth's upper mantle. *Zeitshrift für Geophysik*, *38*, 517–527, 1972.

Riedel, M. R. and Karato, S. I. Grain-size evolution in subducted oceanic lithosphere associated with the olivine-spinel transformation and its effects on rheology. *Earth Planet. Sci. Lett.*, *148*, 27–43, 1997.

Rigden, S. M., Gwanmesia, G. D., Fitz-Gerald, J. D., Jackson, I., and Liebermann, R. C. Spinel elasticity and seismic structure of the transition zone of the mantle. *Nature*, *354*, 143–145, 1991.

Ringwood, A. E. *Composition and Petrology of the Earth's Mantle.* McGraw-Hill, New York, 1975.

Ringwood, A. E. Phase transformations and their bearing on the constitution and dynamics of the mantle. *Geochimica et Cosmochimica Acta*, *55*, 2083–2110, 1991.

Ringwood, A. E. and Irifune, T. Nature of the 650-km seismic discontinuity: implications for mantle dynamics and differentiation. *Nature*, *331*, 131–136, 1988.

Salas, S. L., Hille, E., and Anderson, J. T. *Calculus.* John Wiley and Sons, New York, 1986, 5^{th} edition.

Schimmel, M. and Paulssen, H. Noise reduction and detection of weak, coherent signals through phase-weighted stacks. *Geophys. J. Int.*, *130*, 497–505, 1997.

Seno, T. Philippine Sea Plate kinematics. *Modern Geology*, *14*, 87–97, 1989.

Seno, T. and Maruyama, S. Paleogeographic reconstruction and origin of the Philippine Sea. *Tectonophysics*, *102*, 53–84, 1984.

Seno, T., Stein, S., and Gripp, A. E. A model for the motion of the Philippine Sea Plate consistent with NUVEL-1 and geological data. *J. Geophys. Res.*, *98*, 17941–17948, 1993.

Shearer, P. M. Imaging global body-wave phases by stacking long-period seismograms. *J. Geophys. Res.*, *96*, 20353–20364, 1991.

Silver, P. G. and Jordan, T. H. Total-moment spectra of fourteen large earthquakes. *J. Geophys. Res.*, *88*, 3273–3293, 1983.

Sipkin, S. Estimation of earthquake source parameters by the inversion of waveform data: global seismocity. *Bull. Seism. Soc. Am.*, *76*, 1515–1541, 1986.

Stixrude, L. Structure and sharpness of phase transitions and mantle discontinuities. *J. Geophys. Res.*, *96*, 14835–14852, 1997.

Stunff, Y. L., Wicks, Jr, C. W., and Romanowicz, B. $P'P'$ precursors under Africa: evidence for mid-mantle reflectors. *Science*, *270*, 74–77, 1995.

Sung, C. M. and Burns, R. G. Kinetics of high-pressure phase transformations: implications to the evolution of the olivine - spinel transition in the downgoing lithosphere and its consequences on the dynamics of the mantle. *Tectonophyics*, *21*, 1–32, 1976.

Tajima, F., 1997. Characteristics of the upper mantle transition zone anomalies associated with subduction zones in the northwestern Pacific (abstract). In *Ocean Hemisphere Project*, volume 1, page 90.

Thoraval, C. and Richards, M. A. The geoid constraint in global geodynamics: viscosity structure, mantle heterogeneity models and boundary conditions. *Geophys. J. Int.*, *131*, 1–8, 1997.

van der Hilst, R. and Engdahl, E. R. Step-wise relocation of ISC earthquake hypocenters for linearized tomographic imaging of slab structure. *Phys. Earth Planet. Int.*, *75*, 39–53, 1992.

van der Hilst, R. and Seno, T. Effects of relative plate motion on the deep structure and penetration depth of slabs below the Izu-Bonin and Mariana island arcs. *Earth Planet. Sci. Lett.*, *120*, 395–407, 1993.

van der Hilst, R., Widiyantoro, S., Creager, K. C., and McSweeney, T. J. Deep subduction and aspherical variations in P-wavespeed at the base of Earth's mantle. *J. Geophys. Res.*, *in press*, 1998.

van der Hilst, R., Widiyantoro, S., and Engdahl, E. R. Evidence for deep mantle circulation from global tomography. *Nature*, *386*, 578–584, 1997.

van der Hilst, R. D., Engdahl, R., Spakman, W., and Nolet, G. Tomographic imaging of subducted lithosphere below northwest Pacific island arcs. *Nature*, *353*, 37–42, 1991.

van der Lee, S., Paulssen, H., and Nolet, G. Variability of P660s phases as a consequence of topography of the 660 km discontinuity. *Phys. Earth Planet. Int.*, *86*, 147–164, 1994.

van Keken, P. E., Karato, S. I., and Yuen, D. A. Rheological control of oceanic crust separation in the transition zone. *Geophys. Res. Lett.*, *23*, 1821–1824, 1996.

VanDecar, J. C., 1991. *Upper mantle structure of the Cascadia Subduction Zone from non-linear teleseismic travel-time inversion.* PhD thesis, University of Washington.

Vidale, J. E. and Benz, H. M. Upper-mantle seismic discontinuities and the thermal structure of subduction zones. *Nature*, *356*, 678–683, 1992.

Vinnik, L. P. Detection of waves converted from P to SV in the mantle. *Phys. Earth Planet. Int.*, *15*, 39–45, 1977.

Walck, M. C. The P-wave upper mantle structure beneath an active spreading centre: the Gulf of California. *Geophys. J. R. astr. Soc.*, *76*, 697–723, 1984.

Weidner, D. J. and Wang, Y. Chemical and clapeyron induced buoyancy at the 660 km discontinuity. *J. Geophys. Res.*, *in press*, 1998.

Wen, L. and Anderson, D. L. The fate of slabs inferred from seismic tomography and 130 million years of subduction. *Earth Planet. Sci. Lett.*, *133*, 185–198, 1995.

Wessel, P. and Smith, W. H. F. New version of the Generic Mapping Tools released. *EOS Trans. Amer. Geophys. U.*, *76*, 329, 1995.

Whitcomb, J. H. and Anderson, D. L. Reflection of $p'p'$ seismic waves from discontinuities in the mantle. *J. Geophys. Res.*, *75*, 5713–5728, 1970.

Wicks, Jr, C. W. and Richards, M. A. A detailed map of the 660–kilometer discontinuity beneath the Izu–Bonin subduction zone. *Science*, *261*, 1424–1427, 1993a.

Wicks, Jr, C. W. and Richards, M. A. Seismic evidence for the 1200 km discontinuity (abstract). *Eos Trans. AGU*, *74*, 550, 1993b.

Wicks, Jr, C. W. and Weber, M. California broadband array evidence for an upper mantle reflector beneath the west Mariana ridge (abstract). *Eos Trans. AGU*, *76*, 492, 1996.

Widiyantoro, S., 1997. *Studies of Seismic Tomography on Regional and Global Scale.* PhD thesis, Australian National University.

Wood, B. J. The effect of H_2O on the 410 kilometer seismic discontinuity. *Science*, *268*, 74–76, 1995.

Xu, F., Vidale, J. E., Earle, P. S., and Benz, H. M. Mantle discontinuities under southern africa from precursors to $P'P'_{df}$. *Geophys. Res. Lett.*, *in press*, 1998.

Yamaoka, K. and Fukao, Y. Spherical shell tectonics: Effects of sphericity and inextensibility on the geometry of the descending lithosphere. *Rev. Gphys.*, *24*, 27–53, 1986.

Yamazaki, A. and Hirahara, K. The thickness of upper mantle discontinuities, as inferred from short–period J–array data. *Geophys. Res. Lett.*, *21*, 1811, 1994.

Zhang, Z. and Lay, T. Investigation of upper mantle discontinuities near northwestern Pacific subduction zones using precursors to sSH. *J. Geophys. Res.*, *98*, 4389–4405, 1993.

Zhong, S. and Gurnis, M. Dynamic interaction between tectonic plates, subducting slabs, and the mantle. *Earth Interactions*, *1*, 1997.

Appendix A

DATA - SEISMOGRAMS

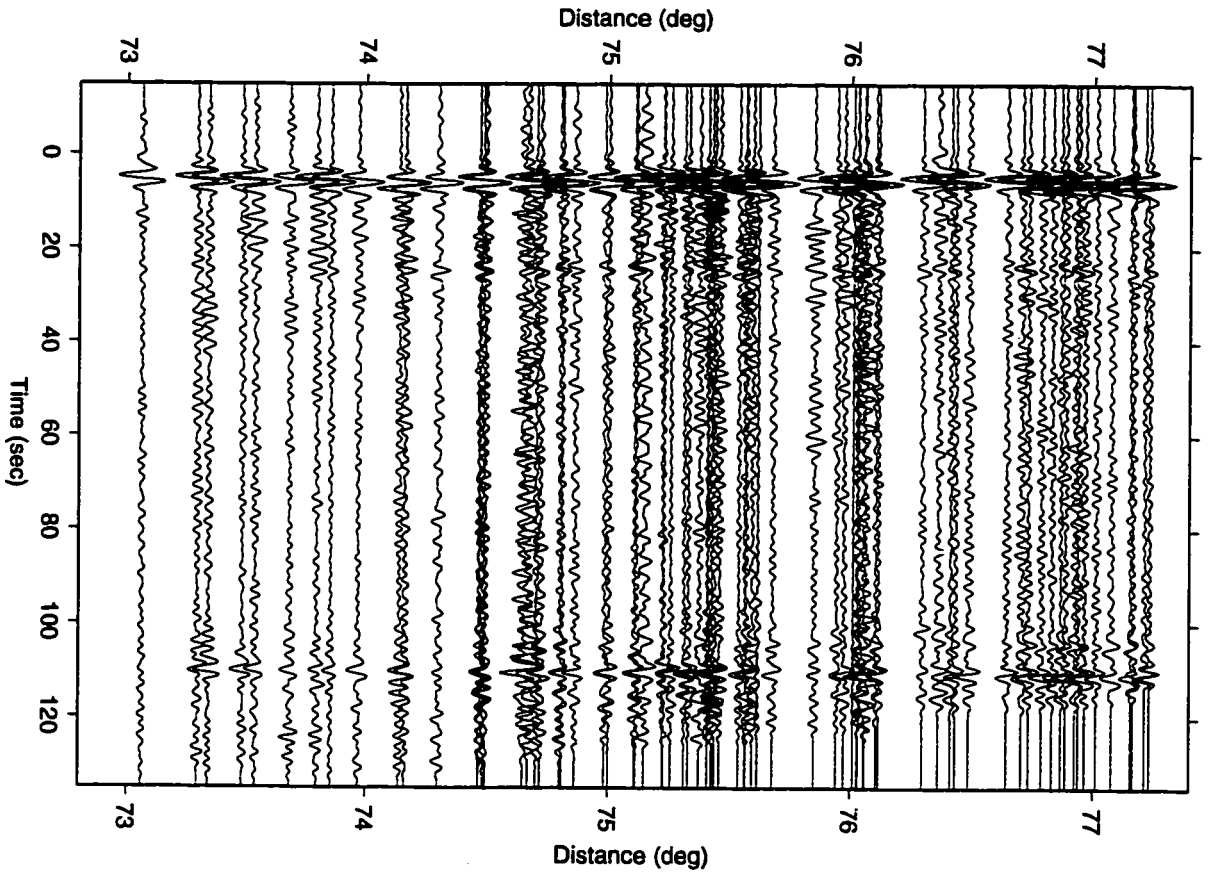

Figure A.1: Sesimograms recorded at the PNSN from the April 3, 1985 Izu-Bonin earthquake at 472 km depth. The records have been bandpass filtered at 2-5 sec and aligned on the P arrival.

Appendix B

DATA STACKING

Figure B.1: Stacking methods applied to the previous data (1985-04-03 to PNSN). The $S_{660}P$ phase is exceptionally clear in these data. The first plot shows of vespegram using a linear slant stack. The second plot shows the N^{th} root method with N=3. This method dramatically reduced bachground noise, which was essential when working with noiser data. The third plot shows a new method called a "Phase Weighted Stack" which weights the data based on the coherency of the instantaneous phase [*Schimmel and Paulssen*, 1997]. The results appear similar to the N^{th} root method with the advantage that there is less signal distortion. Finally, the forth stack shows the results of using the semblence stacking method [*Neidell and Taner*, 1971]. This method extracts coherent signals from the records regardless of their amplitudes.

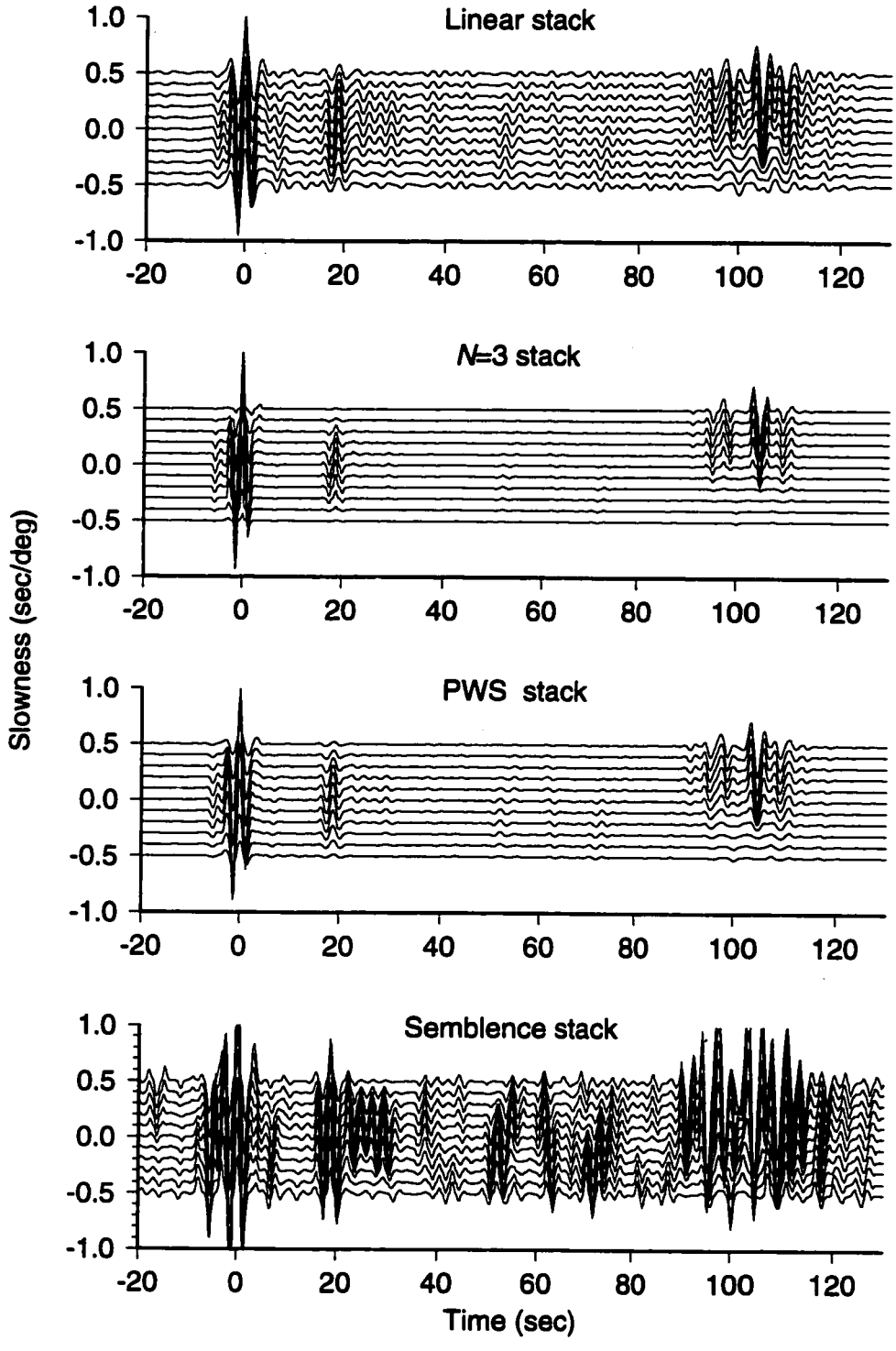
Linear stack
N=3 stack
PWS stack
Semblence stack
1.0
0.5
0.0
-0.5
-1.0
-20
0
20
40
60
80
100
120
Slowness (sec/deg)
Time (sec)

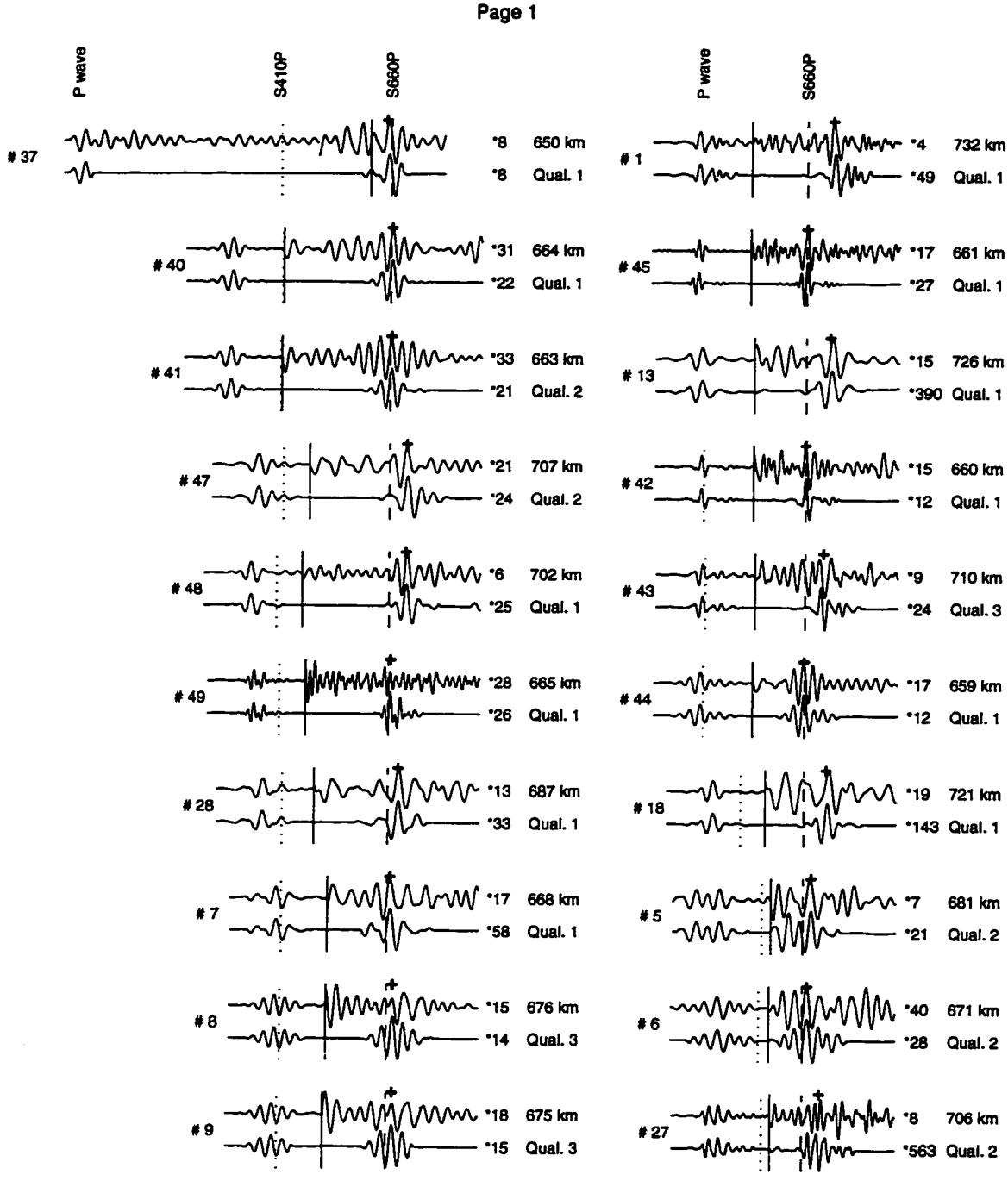

Figure B.2a: Linearly stacked data (N=1): see Figure 2.4, page 18, chapter 2

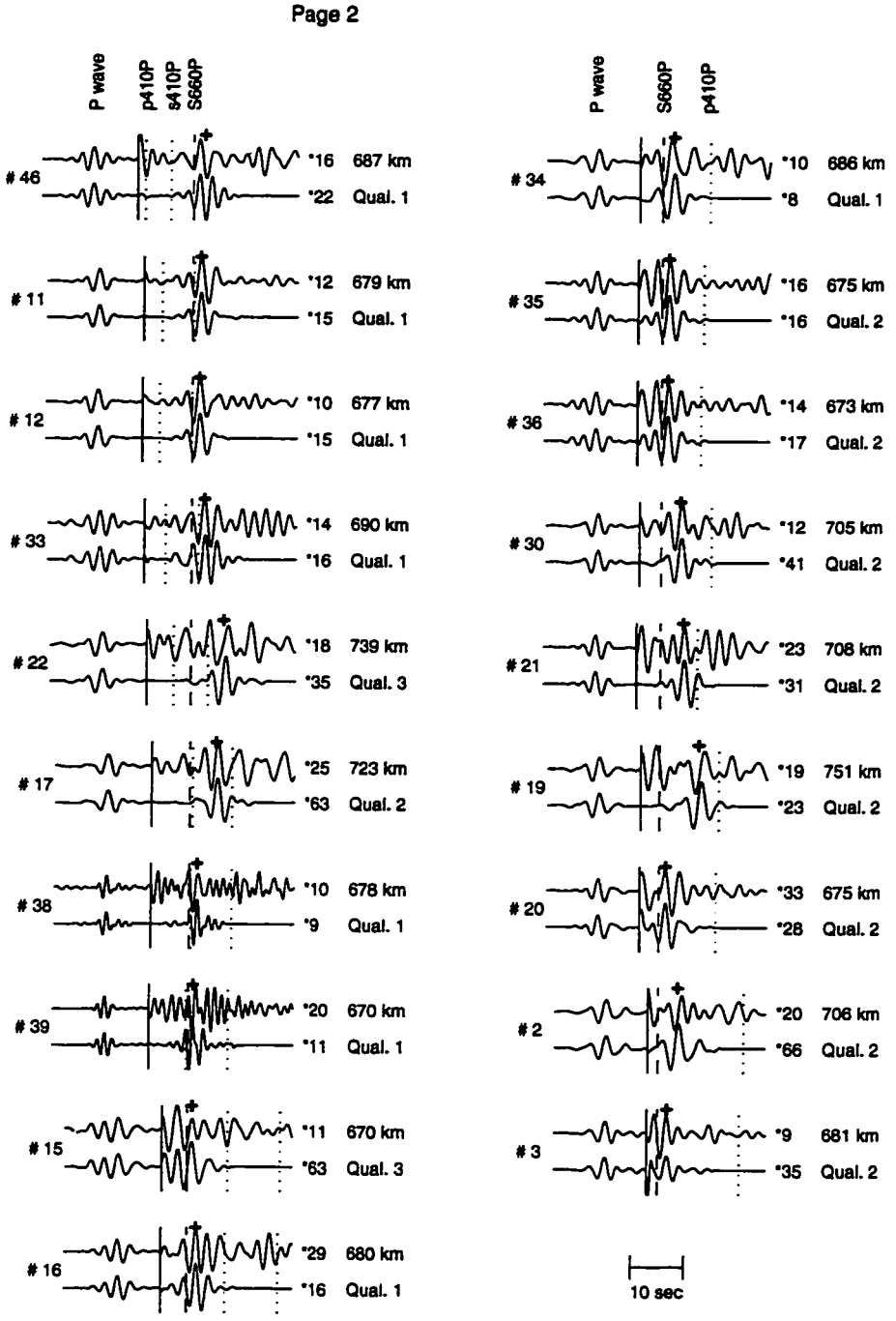

Figure B.2b: (continued)

Appendix C

STATION AND EARTHQUAKE DISTRIBUTION

Figure C.1: Earthquake (+) and station (Δ) distribution. The station and earthquake distribution are shown in Figure C. Geyookcha is the small array on the east side of the Caspian Sea, India is the GBA array run by the Blackness organization in the United Kingdom, Australia is records from the *Skippy* project, and the Western U.S. includes networks in Washington, Oregon, and California.

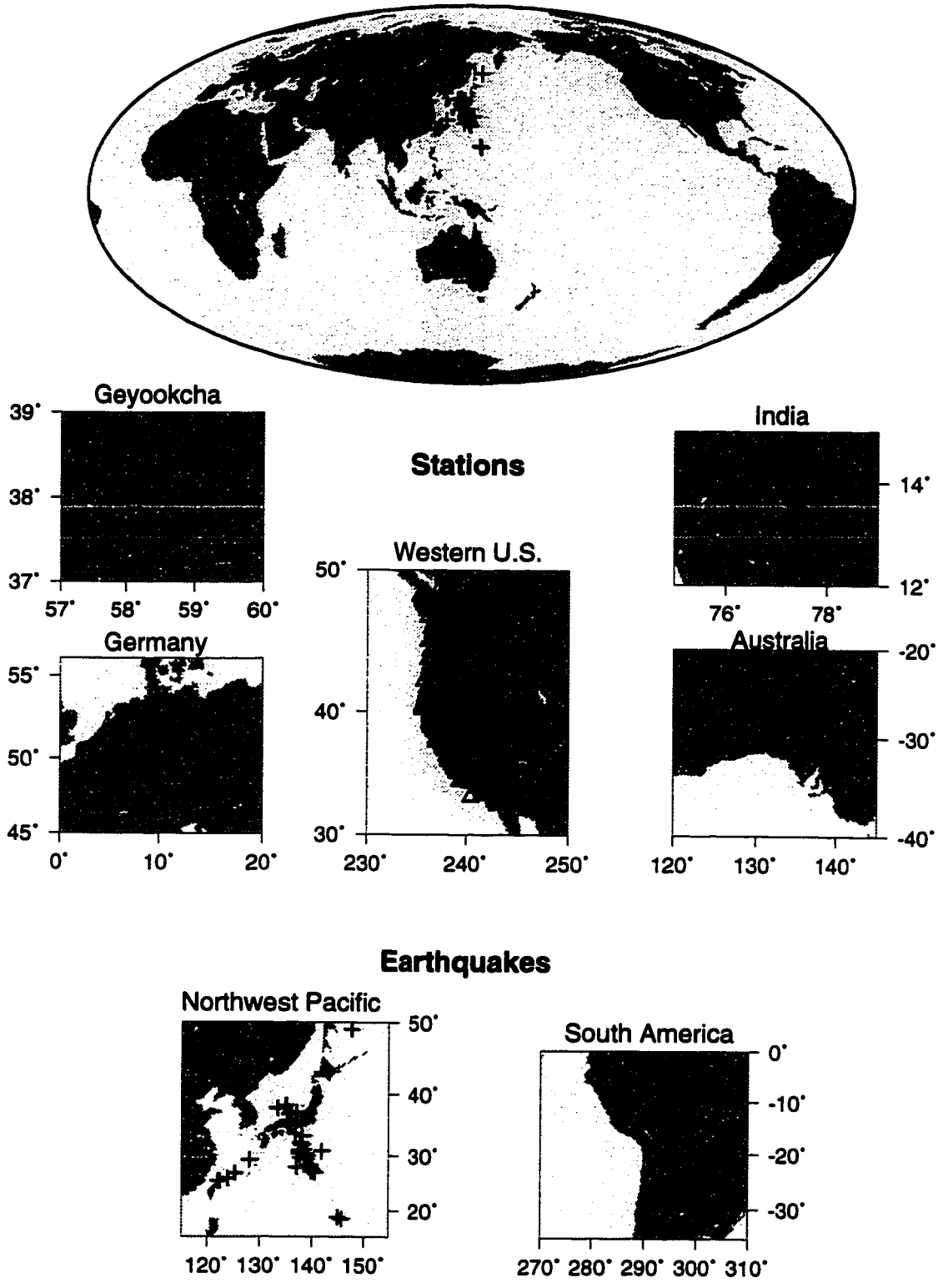
Geyookcha
39°
38°
37°
57°
58°
59°
60°
Germany
55°
50°
45°
0°
10°
20°
Stations
Western U.S.
50°
40°
30°
230°
240°
250°
India
14°
12°
76°
78°
Australia
-20°
-30°
-40°
120°
130°
140°
Earthquakes
Northwest Pacific
50°
40°
30°
20°
120°
130°
140°
150°
South America
0°
-10°
-20°
-30°
270°
280°
290°
300°
310°

VITA

- 1970 : Born, May 30, Joliet, Illinois
- 1992 : B.A. Physics, Rice University, Houston, Texas
- 1995 : Visiting Scholar, Universität Göttingen, Göttingen, Germany
- 1996 : Fulbright Scholar, Australian National University, Canberra, Australia
- 1998 : Ph.D. Geophysics, University of Washington, Seattle, Washington

IMAGE EVALUATION
TEST TARGET (QA-3)

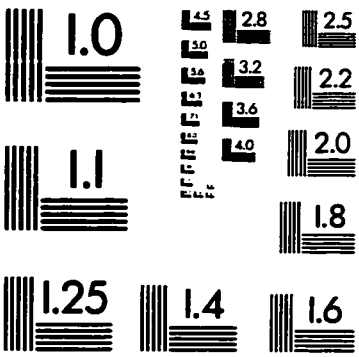

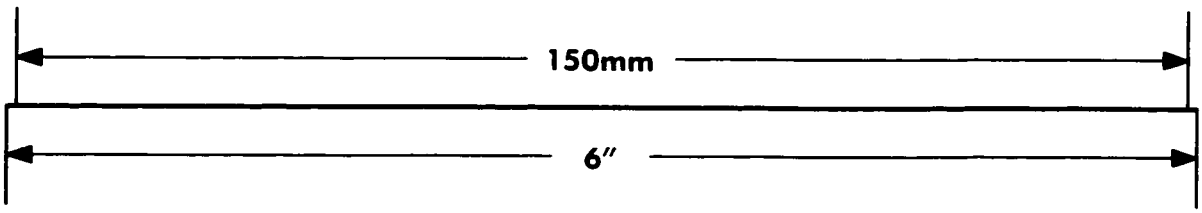

APPLIED IMAGE, Inc
1653 East Main Street
Rochester, NY 14609 USA
Phone: 716/482-0300
Fax: 716/288-5989